

NASA CONTRACTOR REPORT

NASA CR-1926



NASA CR

pt. 1
C. 1

0061017



TECH LIBRARY KAFB, NM

LOAN COPY: RETURN TO
AFWL (DOUL)
KIRTLAND AFB, N. M.

FLOW FIELD ANALYSIS OF AIRCRAFT CONFIGURATIONS USING A NUMERICAL SOLUTION TO THE THREE-DIMENSIONAL UNIFIED SUPERSONIC/HYPERSONIC SMALL-DISTURBANCE EQUATIONS

Part I

*by R. C. Gunness, Jr., C. J. Knight,
and E. D'Sylva*

Prepared by
THE BOEING COMPANY
Seattle, Wash.
for Langley Research Center

NATIONAL AERONAUTICS AND SPACE ADMINISTRATION • WASHINGTON, D. C. • FEBRUARY 1972



0061017

1. Report No. NASA CR-1926		2. Government Accession No.		3. Recipient's Catalog No.	
4. Title and Subtitle FLOW FIELD ANALYSIS OF AIRCRAFT CONFIGURATIONS USING A NUMERICAL SOLUTION TO THE THREE-DIMENSIONAL UNIFIED SUPERSONIC/HYPERSONIC SMALL-DISTURBANCE EQUATIONS, PART I				5. Report Date February 1972	
				6. Performing Organization Code	
7. Author(s) R. C. Gunness, Jr., C. J. Knight, and E. D'Sylva				8. Performing Organization Report No. D6-25124, Part I	
9. Performing Organization Name and Address The Boeing Company Commercial Airplane Group Seattle, Washington				10. Work Unit No.	
				11. Contract or Grant No. NAS1-9562	
12. Sponsoring Agency Name and Address National Aeronautics and Space Administration Washington, D.C. 20546				13. Type of Report and Period Covered Contractor Report	
				14. Sponsoring Agency Code	
15. Supplementary Notes					
16. Abstract <p>The unified small disturbance equations are numerically solved using the well-known Lax-Wendroff finite-difference technique. The method allows complete determination of the inviscid flow field and surface properties as long as the flow remains supersonic. Shock waves and other discontinuities are accounted for implicitly in the numerical method. This technique has been programmed for general application to the three-dimensional case. The validity of the method is demonstrated by calculations on (1) cones, (2) axisymmetric bodies, (3) lifting bodies, (4) delta wings, and (5) a conical wing/body combination. Part I contains the discussion of problem development and results of the study. Part II contains flow charts, subroutine descriptions, and a listing of the computer program.</p> <p style="text-align: right;">1. Inviscid flow 2. Hypersonic flow 3. Supersonic flow</p>					
17. Key Words (Suggested by Author(s)) Flow fields Inviscid flow Finite difference Steady flow Aircraft flows Three-dimensional flow Flow analysis				18. Distribution Statement Unclassified - Unlimited	
19. Security Classif. (of this report) Unclassified		20. Security Classif. (of this page) Unclassified		21. No. of Pages 114	
				22. Price* \$3.00	

CONTENTS

	Page
SUMMARY	1
INTRODUCTION	1
Requirements for Hypersonic Flow-Field Method	1
Discussion of Possible Approaches	3
Three-dimensional characteristics	3
Three-dimensional finite differences	3
Hypersonic small-disturbance theory and finite differences	3
Summary of Reasons for Selection of Present Method	4
SYMBOLS	5
ANALYSIS	7
Hypersonic Small-Disturbance Theory	7
Derivation of equations	7
Unified theory and accuracy of small-disturbance assumption	10
Numerical Solution to Hypersonic Small-Disturbance Equations	10
Grid system	10
Differencing method for update of regular grid points	14
Differencing method for update of body points	15
Update of between-grid points	17
Geometry Definition	17
Initial Conditions	17
COMPUTER PROGRAM USE	19
Program Elements	19
Input Data Preparation	23
Printed Output Data	27
Comments on Program Use	28
RESULTS	31
Cone	32
Axisymmetric Bodies	32
Elliptic Cones and Elliptic Cone/Wedge	42
Delta Wing—Supersonic Flow	50
Subsonic leading edge	50
Supersonic leading edge	53
Delta Wings—Hypersonic Flow	57
Wing/Body Combination	57
CONCLUSIONS	65
APPENDIX A—Boundary Update Scheme BND1 (Conservative Differencing)	67

CONTENTS—Concluded

	Page
APPENDIX B—Boundary Update Scheme BND3 (Method of Characteristics)	73
APPENDIX C—Surface Interpolation Procedure	81
APPENDIX D—Geometry Package Usage	85

FIGURES

No.		Page
1	Inviscid Flow Theories—Regions of Applicability	2
2	Comparison of Hypersonic Theory and Unified Theory for Flow Over a Wedge	11
3	Accuracy of the Unified Theory for Flow Over a Cone	12
4	Grid System in Cross-Flow Plane	13
5	Construction of Surface Coordinate System to Update Surface Properties	16
6	Modification of Body to Allow for an Impulsive Start or Tangent Cone Start	18
7	Program Overlay Structure	20
8	Computer Deck Setup	22
9	Asymptotic Convergence to a Steady State After an Impulsive Start	33
10	Comparison of the Steady-State Pressure Distribution After an Impulsive Start With the Exact Pressure Distribution	34
11	Comparison of Pressure Distributions for a Cone at Angle of Attack Obtained Using Different Methods	35
12	Comparison of Pressure Distributions for a Cone at Angle of Attack Obtained Using Different Methods	36
13	Supersonic Flow Over Cone at Angle of Attack	37
14	Surface Mach Number	38
15	Development of the Pressure Distribution on a Power Law Body After an Impulsive Start	39
16	Pressure Coefficient on an $\ell/d = 3$ Circular-Arc Ogive	40
17	Pressure Coefficient on an $\ell/d = 3$ Circular-Arc Ogive	41
18	Hypersonic Flow Over a Cone-Cylinder	43
19	Supersonic Flow Over Circular-Arc Body	44
20	Pressure Distribution on an Elliptic Cone, $\alpha = 0^\circ$	45
21	Pressure Distribution on an Elliptic Cone, $\alpha = 4^\circ$	46
22	Pressure Distribution on an Elliptic Cone, $\alpha = 6^\circ$	47
23	Pressure Distribution on an Elliptic Cone, $\alpha = 1.0^\circ$	48
24	Surface Pressure on An Elliptic Cone/Wedge	49
25	Pressure Distribution for Supersonic Delta Wing With Subsonic Leading Edges	51
26	Comparison of Surface Update Scheme 3, BND1, and BND3 for Supersonic Flow Over Delta Wing	52
27	Tangential Momentum Variation	54
28	Density Variation	55
29	Pressure Distribution of Supersonic Delta Wing With Supersonic Leading Edges	56
30	Shock Shape for Hypersonic Flow Over Slab Delta Wing	58
31	Pressure Distribution for Lower Surface of Hypersonic Slab Delta Wing	59
32	Delta Wing Pressure Distribution With Leading Edge and Initial Conditions Modified	60
33	Pressure Distribution for Flat Delta Wing	61
34	Shock Shape for Flow Over Wing/Body Combination	62
35	Pressure Distribution for Flow Over Wing/Body Combination	63
36	Interpolation Without Corresponding Points	82
37	Interpolation With Corresponding Points	83
38	SST Geometry	104

TABLES

No.		Page
1	Numerical Values of Significant Parameters Used in Computer Runs for Figures 9 to 35	31
2	SST Input Data	97

FLOW FIELD ANALYSIS OF AIRCRAFT CONFIGURATIONS USING A NUMERICAL SOLUTION TO THE THREE-DIMENSIONAL UNIFIED SUPERSONIC/HYPERSONIC SMALL-DISTURBANCE EQUATIONS

Part I

By R. C. Gunness, Jr., C. J. Knight, and E. D'Sylva
The Boeing Company

SUMMARY

The Boeing Company has completed an 18-month contract to refine and demonstrate the applicability of a method for theoretically predicting the inviscid three-dimensional flow about supersonic/hypersonic aircraft configurations. All of the contract commitments have been met.

The method provides a numerical solution to the nonlinear small-disturbance equations embodied in the unified supersonic/hypersonic theory developed by Van Dyke. The small-disturbance equations are applicable for both supersonic and hypersonic flow over configurations whose local surface inclinations to the freestream are everywhere small. The numerical method uses the well-known Lax-Wendroff finite difference technique. It allows determination of the complete flow field, in addition to the surface properties. Shock waves and other discontinuities are accounted for implicitly in the numerical method (due to the "artificial viscosity" inherent in the differenced equation) and, hence, no special techniques are required to treat these discontinuities.

The numerical method has been programmed for general application to the three-dimensional case. To demonstrate the validity of the program, several special cases were analyzed for various angles of attack. These include (1) cones, (2) axisymmetric bodies, (3) lifting bodies, (4) delta wings, and (5) a wing/body combination. The agreement with other theoretical methods and experimental data was good. The program, written in FORTRAN IV for the CDC 6600 digital computer, should be an ideal tool for aerodynamic design and analysis studies of supersonic and hypersonic vehicles such as the SST and HST.

INTRODUCTION

Requirements for Hypersonic Flow-Field Method

The aerodynamic analysis requirements for the successful design of a hypersonic transport include (1) the need for more accurate overall prediction methods for aircraft lift, drag, and pitching moments and (2) the need for a fairly detailed description of the complete flow field. For the first problem, the most practical and useful methods currently available are linear theory and the various versions of the Newtonian theory. However, as illustrated in figure 1, the hypersonic transport is expected to lie in a region wherein neither of these methods is appropriate. For the second problem, there appears to be no satisfactory practical method currently available to handle the complicated nonlinear interactions that are expected to be so important in hypersonic cruise vehicle design.

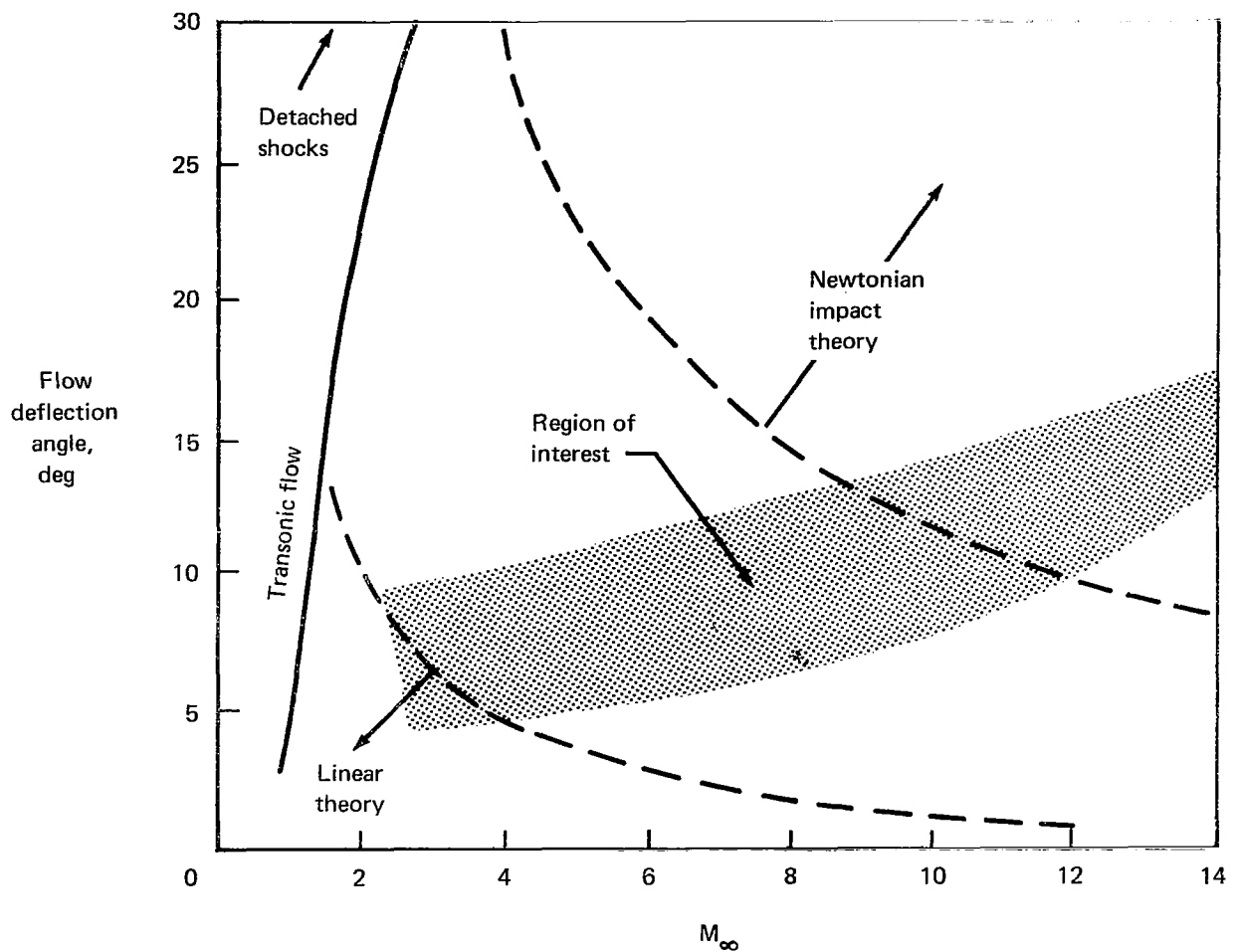


FIGURE 1.—INVISCID FLOW THEORIES—REGIONS OF APPLICABILITY

To fulfill these requirements, it was felt that the following methods were theoretically suitable for predicting both the overall aerodynamic parameters and the complete flow field.

- 1) Three-dimensional characteristics
- 2) Three-dimensional finite differences
- 3) Small-disturbance theory and finite difference methods

The feasibility of implementing these three methods is considered next.

Discussion of Possible Approaches

Three-dimensional characteristics.—This method has been studied by many research and industrial organizations for at least 10 years. Very few successful calculations exist, however, and the current state-of-the-art seems to be limited to axisymmetric bodies, and certain conical-type bodies that may be at angle of attack. The relatively slow progress in developing this method is due to the complex geometry of the wave intersections and the difficulty in specifying boundary conditions at the body surface. It appears that the development of a practical and convenient three-dimensional (nonconical flow) characteristics method is still some years away. Research on this method is currently being conducted by Rakich (ref. 1) and Beeman and Powers (ref. 2).

Three-dimensional finite differences.—In recent years, the method of finite differences has become an attractive alternative to the method of characteristics. This is made possible by the development of finite difference methods capable of calculating flow fields with discontinuities (such as shock waves, slip lines, etc.) without requiring any special treatment in the region of the discontinuity. The discontinuities are, in fact, spread out over several computational mesh points due to the “artificial viscosity” associated with the truncation error of the finite difference equations (see refs. 3 and 4). This allows the flow field development to be computed directly, whereas the method of characteristics required special treatment when discontinuities occur.

The use of steady two-dimensional finite differences has been successfully applied by DeJarnette (ref. 5) for supersonic flow wherein a special body coordinate system was employed. Thommen and D'Atorre (ref. 6) applied the finite difference technique to a simple steady three-dimensional supersonic flow. Recently Kutler (ref. 7) used finite differences to develop a method for predicting three-dimensional conical flows.

The use of steady three-dimensional finite difference for the present nonconical-type flow application appears to be attractive, but there could be practical difficulties in numerically enforcing boundary conditions on complicated three-dimensional bodies. Non-Cartesian body coordinate systems, such as employed by DeJarnette, would be very difficult to generalize to the general three-dimensional body. Additional groundwork and experience are required before the exact three-dimensional problem is attacked.

Hypersonic small-disturbance theory and finite differences.—The hypersonic small-disturbance assumption (Van Dyke, ref. 8, and Hayes, ref. 9) implies that the steady three-dimensional flow is equivalent to an unsteady two-dimensional flow (in the crossflow plane). The hypersonic small-disturbance equations, whose accuracy is discussed in “Unified Theory and Accuracy of Small-Disturbance Assumption,” allow a simplification of the problem. This is due to the fact that the boundary conditions are simpler to enforce in the unsteady crossflow plane than on the steady three-dimensional body. Also, there exists in the literature more numerical experience for two-dimensional, unsteady, finite difference methods than for the steady, three-dimensional problem. In a recent review paper by C. K. Chu (ref. 10), various unsteady two-dimensional techniques are presented.

Summary of Reasons for Selection of Present Method

After weighing the attributes and problems of these schemes, the hypersonic small-disturbance approach was chosen for this initial undertaking. A number of advantages it has over other schemes are listed below.

- 1) Finite difference methods are easier to implement than the method of characteristics.
- 2) The hypersonic small-disturbance equations are known to yield an accurate description of the flow field (this is discussed under “Unified Theory and Accuracy of Small-Disturbance Assumption”).
- 3) The numerical experience gained in solving the hypersonic small-disturbance equations can be applied to an exact, steady, three-dimensional formulation.
- 4) Computer run times and storage requirements would be somewhat reduced from the full problem.

SYMBOLS

\bar{a}	speed of sound, $\sqrt{\gamma R \bar{T}}$
a	dimensionless speed of sound, \bar{a}/\bar{w}_∞
BND1	conservative boundary update scheme (app. A)
BND3	characteristics boundary update scheme (app. B)
c	curvature
E	dimensionless energy function, $p + 1/2 \rho(u^2 + v^2) \gamma(\gamma - 1)\beta^2$
f	four-component vector function
g	four-component vector function
M_∞	freestream Mach number
NC	number of contour points
NT	number of time (or z) steps
NX	number of x-direction mesh points
NY	number of y-direction mesh points
n	coordinate normal to crosscut contour
\tilde{n}	relative normal coordinate, $n - \dot{\lambda}t$
\bar{p}	pressure
p	dimensionless pressure, \bar{p}/\bar{p}_∞
s	surface coordinate along crosscut contour (arc length)
\tilde{s}	relative surface coordinate, $s - \dot{\gamma}t$
\bar{S}	dimensionless entropy function, p/ρ^γ
\bar{T}	temperature
T	dimensionless temperature, \bar{T}/\bar{T}_∞
\bar{t}	time variable, z/\bar{w}_∞
t	z
\bar{u}	crossflow velocity component in x-direction

u	dimensionless value, \bar{u}/\bar{w}_∞
\tilde{u}, u	dimensionless crossflow velocity tangent to crosscut contour
\bar{v}	crossflow velocity component in y-direction
v	dimensionless value, \bar{v}/\bar{w}_∞
v'	dimensionless crossflow velocity normal to crosscut contour
\tilde{v}	relative normal velocity, $v' - \dot{\lambda}$
W	four-component vector function
\bar{w}	velocity component in longitudinal (z) direction
w	dimensionless value, \bar{w}/\bar{w}_∞
x	crossflow plane abscissa, dimensions arbitrary
y	crossflow plane ordinate, dimensions arbitrary
z	longitudinal coordinate ($= t$)
α	angle of attack, degrees
β	$\sqrt{M_\infty^2 - 1}$
γ	ratio of specific heats
$\dot{\gamma}$	dimensionless tangential velocity of crosscut contour point
Λ	sweepback angle
$\dot{\lambda}$	dimensionless normal velocity of crosscut contour point
$\bar{\rho}$	density
ρ	dimensionless density, $\bar{\rho}/\bar{\rho}_\infty$

Subscripts:

∞	freestream
i, I	mesh point location along x-axis (measured from centerline)
j, J	mesh point location along y-axis (measured from bottom of mesh)

Superscripts:

(\wedge)	tentative value
(\sim)	dimensional quantity
(\approx)	relative quantity

ANALYSIS

Hypersonic Small-Disturbance Theory

Derivation of equations.—Mathematically, the inviscid formulation for a hypersonic aircraft (see sketch below) is:

$$\frac{\partial(\bar{\rho}\bar{u})}{\partial x} + \frac{\partial(\bar{\rho}\bar{v})}{\partial y} + \frac{\partial(\bar{\rho}\bar{w})}{\partial z} = 0 \quad \text{continuity equation}$$

$$\bar{u} \frac{\partial \bar{u}}{\partial x} + \bar{v} \frac{\partial \bar{u}}{\partial y} + \bar{w} \frac{\partial \bar{u}}{\partial z} + \frac{1}{\bar{\rho}} \frac{\partial \bar{p}}{\partial x} = 0 \quad \text{x-momentum equation}$$

$$\bar{u} \frac{\partial \bar{v}}{\partial x} + \bar{v} \frac{\partial \bar{v}}{\partial y} + \bar{w} \frac{\partial \bar{v}}{\partial z} + \frac{1}{\bar{\rho}} \frac{\partial \bar{p}}{\partial y} = 0 \quad \text{y-momentum equation}$$

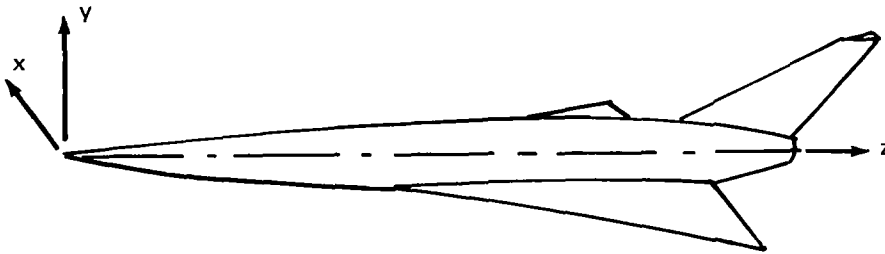
$$\bar{u} \frac{\partial \bar{w}}{\partial x} + \bar{v} \frac{\partial \bar{w}}{\partial y} + \bar{w} \frac{\partial \bar{w}}{\partial z} + \frac{1}{\bar{\rho}} \frac{\partial \bar{p}}{\partial z} = 0 \quad \text{z-momentum equation}$$

$$\bar{u} \frac{\partial(\bar{p}/\bar{\rho}^\gamma)}{\partial x} + \bar{v} \frac{\partial(\bar{p}/\bar{\rho}^\gamma)}{\partial y} + \bar{w} \frac{\partial(\bar{p}/\bar{\rho}^\gamma)}{\partial z} = 0 \quad \text{energy equation}$$

with boundary condition

$$\bar{u}n_x + \bar{v}n_y + \bar{w}n_z = 0 \quad \text{no flow-through surface}$$

In addition, the solutions must satisfy the Rankine-Hugoniot relations across shock waves.



Now, for a body whose maximum deflection angle is small, the following ordering is assumed (see ref. 8 for further details).

$\delta \equiv$ flow deflection angle $\ll 1$ } slender body assumption

$$\left. \begin{aligned} \bar{u}/w_{\infty} &= O(\delta) \\ \bar{v}/w_{\infty} &= O(\delta) \\ \bar{w}/w_{\infty} &= O(1) \text{ or } \frac{w - w_{\infty}}{w_{\infty}} = O(\delta^2) \\ \bar{p}/p_{\infty} &= O(M_{\infty}^2 \delta^2) \\ \bar{\rho}/\rho_{\infty} &= O(1) \end{aligned} \right\} \text{magnitude of aerodynamic quantities}$$

$$\left. \begin{aligned} x &= O(\delta) \\ y &= O(\delta) \\ z &= O(1) \end{aligned} \right\} \text{shock lies close to body}$$

where

$$\left. \begin{aligned} M_{\infty} &\gg 1 \\ \delta &\ll 1 \\ \frac{1}{M_{\infty} \delta} &= O(1) \end{aligned} \right\} \text{description of limiting process}$$

If the above relations are used in the Euler equations, the following hypersonic small-disturbance equations are obtained:

$$\bar{w}_{\infty} \frac{\partial \bar{p}}{\partial z} + \frac{\partial(\bar{\rho} \bar{u})}{\partial x} + \frac{\partial(\bar{\rho} \bar{v})}{\partial y} = 0 + O(\delta^2) \quad (1)$$

$$\bar{w}_{\infty} \frac{\partial \bar{w}}{\partial z} + \frac{\bar{u} \partial \bar{w}}{\partial x} + \frac{\bar{v} \partial \bar{w}}{\partial y} + \frac{1}{\bar{\rho}} \frac{\partial \bar{p}}{\partial z} = 0 + O(\delta^4) \quad (2)$$

$$\bar{w}_\infty \frac{\partial \bar{v}}{\partial z} + \bar{u} \frac{\partial \bar{v}}{\partial x} + \bar{v} \frac{\partial \bar{v}}{\partial y} + \frac{1}{\bar{\rho}} \frac{\partial \bar{p}}{\partial y} = 0 + O(\delta^3) \quad (3)$$

$$\bar{w}_\infty \frac{\partial \bar{u}}{\partial z} + \bar{u} \frac{\partial \bar{u}}{\partial x} + \bar{v} \frac{\partial \bar{u}}{\partial y} + \frac{1}{\bar{\rho}} \frac{\partial \bar{p}}{\partial x} = 0 + O(\delta^3) \quad (4)$$

$$\bar{w}_\infty \frac{\partial}{\partial z} (\bar{p}/\bar{\rho}^\gamma) + \bar{u} \frac{\partial}{\partial x} (\bar{p}/\bar{\rho}^\gamma) + \bar{v} \frac{\partial}{\partial y} (\bar{p}/\bar{\rho}^\gamma) = 0 + O(\delta^2) \quad (5)$$

with boundary conditions

$$\bar{w}_\infty n_z + \bar{u} n_x + \bar{v} n_y = 0 + O(\delta^3) \quad (6)$$

The following observations are in order concerning the hypersonic small-disturbance equations.

1) Equation (2) becomes uncoupled from the remaining equations and \bar{w} can be determined from the Bernoulli equation below—once the other variables are known.

$$\bar{w}_\infty \bar{w}' + \frac{1}{2} (\bar{u}^2 + \bar{v}^2) + \frac{\gamma}{\gamma-1} \frac{\bar{p}}{\bar{\rho}} = \text{constant}$$

2) The error of the neglected terms, denoted by $O(\delta)$ on the right of the equations, is two orders of magnitude smaller than the retained terms.

3) Equations (1), (3), (4), (5), and (6) are equivalent to the unsteady two-dimensional flow equations. That is, if we let $\bar{t} = z/w_\infty$ and neglect higher order terms, these equations become

$$\frac{\partial \bar{p}}{\partial \bar{t}} + \frac{\partial (\bar{\rho} \bar{u})}{\partial x} + \frac{\partial (\bar{\rho} \bar{v})}{\partial y} = 0 \quad (7)$$

$$\frac{\partial \bar{v}}{\partial \bar{t}} + \bar{u} \frac{\partial \bar{v}}{\partial x} + \bar{v} \frac{\partial \bar{v}}{\partial y} + \frac{1}{\bar{\rho}} \frac{\partial \bar{p}}{\partial y} = 0 \quad (8)$$

$$\frac{\partial \bar{u}}{\partial \bar{t}} + \bar{u} \frac{\partial \bar{u}}{\partial x} + \bar{v} \frac{\partial \bar{u}}{\partial y} + \frac{1}{\bar{\rho}} \frac{\partial \bar{p}}{\partial x} = 0 \quad (9)$$

$$\frac{\partial}{\partial \bar{t}} (\bar{p}/\bar{\rho}^\gamma) + \bar{u} \frac{\partial}{\partial x} (\bar{p}/\bar{\rho}^\gamma) + \bar{v} \frac{\partial}{\partial y} (\bar{p}/\bar{\rho}^\gamma) = 0 \quad (10)$$

$$\frac{\partial n}{\partial \bar{t}} + \bar{u} n_x + \bar{v} n_y = 0 \quad (11)$$

$$y, x \rightarrow \infty, \quad \bar{v}, \bar{u} \rightarrow 0, \quad \bar{p} \rightarrow \bar{p}_\infty, \quad \bar{\rho} \rightarrow \bar{\rho}_\infty \quad (12)$$

which are the two-dimensional unsteady Euler equations. The hypersonic small-disturbance assumption then allows us to solve approximately the steady, three-dimensional gas dynamic equations by considering the unsteady, two-dimensional flow in the crossflow plane.

Unified theory and accuracy of small-disturbance assumption.—Van Dyke (ref. 8) pointed out that, if M_∞ is simply replaced by $\beta = \sqrt{M_\infty^2 - 1}$ (and the pressure and density reinterpreted) in this formulation, then the above equations are valid for supersonic flows as well. That is, the restriction of the limit $M \rightarrow \infty$ is effectively removed and a unified theory is obtained that is valid for both supersonic and hypersonic flows. This is fortunate and adds significantly to the utility of the present method.

Figure 2 shows the accuracy of unified theory for the case of a wedge. Figure 3 shows the general applicability of the theory for a cone. Also shown are the results from linear theory and second-order theory. Reference 8 shows equally good results for other bodies. These results suggest that the small-disturbance assumption is reasonable for configurations having small surface inclinations.

In view of these encouraging results it was felt that an attempt should be made to obtain solutions to the unified supersonic/hypersonic small-disturbance equations for more general bodies. An important requirement of such a method is that it must be applicable to fairly complicated bodies such as the HST. Due to the geometry requirements and the complicated nonlinear nature of equations (7) through (12), it was readily evident that a fairly complex numerical solution would be required. It was felt, however, that the availability of large computers and advanced numerical methods makes it feasible to solve this problem.

Numerical Solution to Hypersonic Small-Disturbance Equations

To obtain an effective numerical scheme for the solution to equations (7) through (12) for an arbitrary two-dimensional body deforming with time in the crossflow plane, requires the effective combination of many numerical components. Items such as numerical stability, accuracy, treatment of regular grid points, satisfaction of boundary conditions, both on the body and at infinity, and geometry definition must be considered very carefully before an effective numerical scheme can be constructed. The above items are given individual consideration and the selected solutions used are outlined. The overall setup is shown in figure 4.

Grid system.—The grid system adopted for the field is a Cartesian system of equally spaced points. The use of a Cartesian grid was chosen primarily because of its simplicity of definition. In addition, the equations of motion remain conservative in their differenced form when such a system is used. This is a desirable property as regards shock definition (see ref. 11). For points on the body, a local surface coordinate system is used. Figure 4 shows the basic Cartesian mesh in the crossflow plane. Also shown is the local surface coordinate system on the body associated with a particular boundary. Other boundary points and their corresponding local surface coordinate systems are not shown.

The Cartesian points in the crossflow plane are divided into three types that include:

- 1) Regular grid points—These points lie outside the contour, and the rectangular region ($2\Delta x$ by $2\Delta y$) that surrounds these points must contain no portion of the crosscut contour.
- 2) Between points—These points also lie outside the contour, but the surrounding rectangle is intersected by the crossflow contour.
- 3) Inside points—These points lie inside the contour.

Points from the above three classes are shown in figure 4.

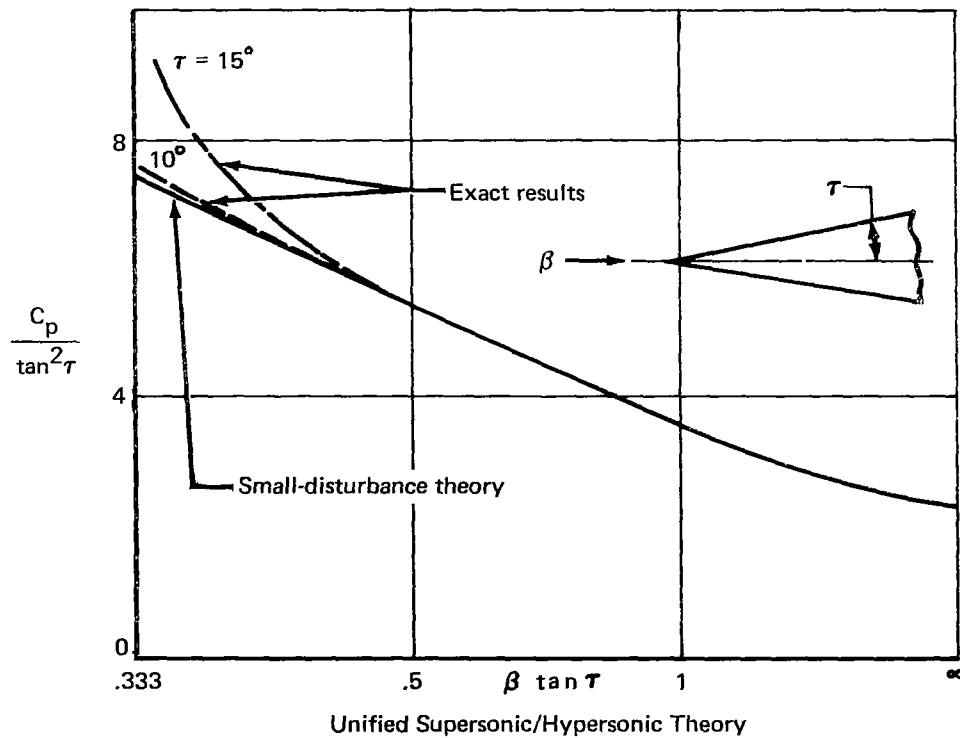
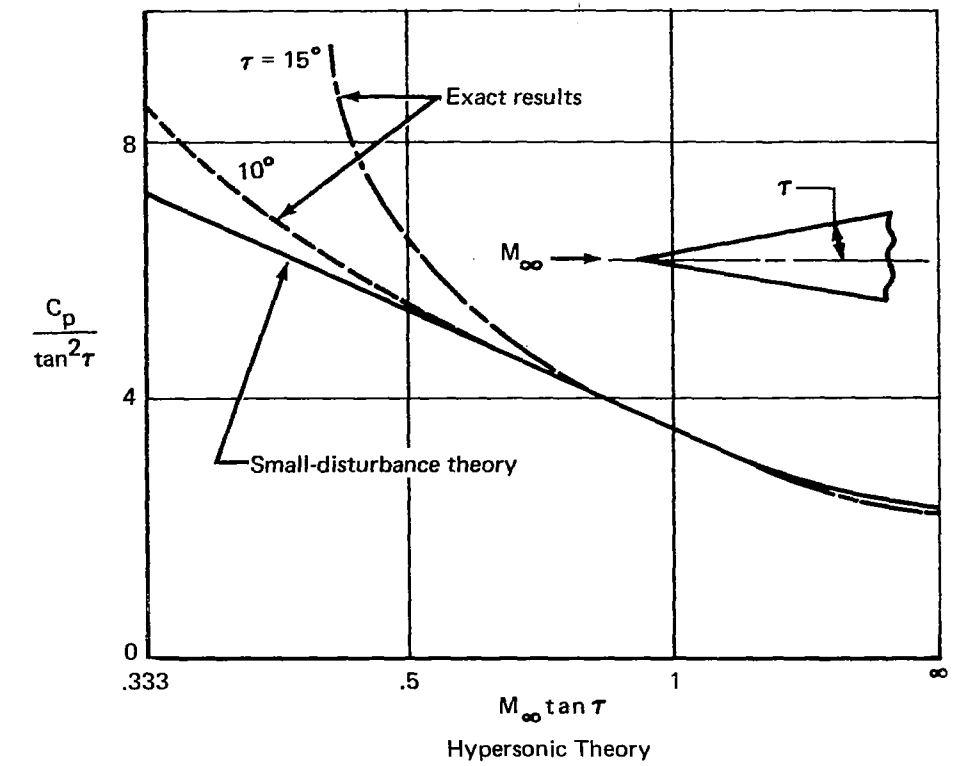


FIGURE 2.—COMPARISON OF HYPERSONIC THEORY AND UNIFIED THEORY FOR FLOW OVER A WEDGE

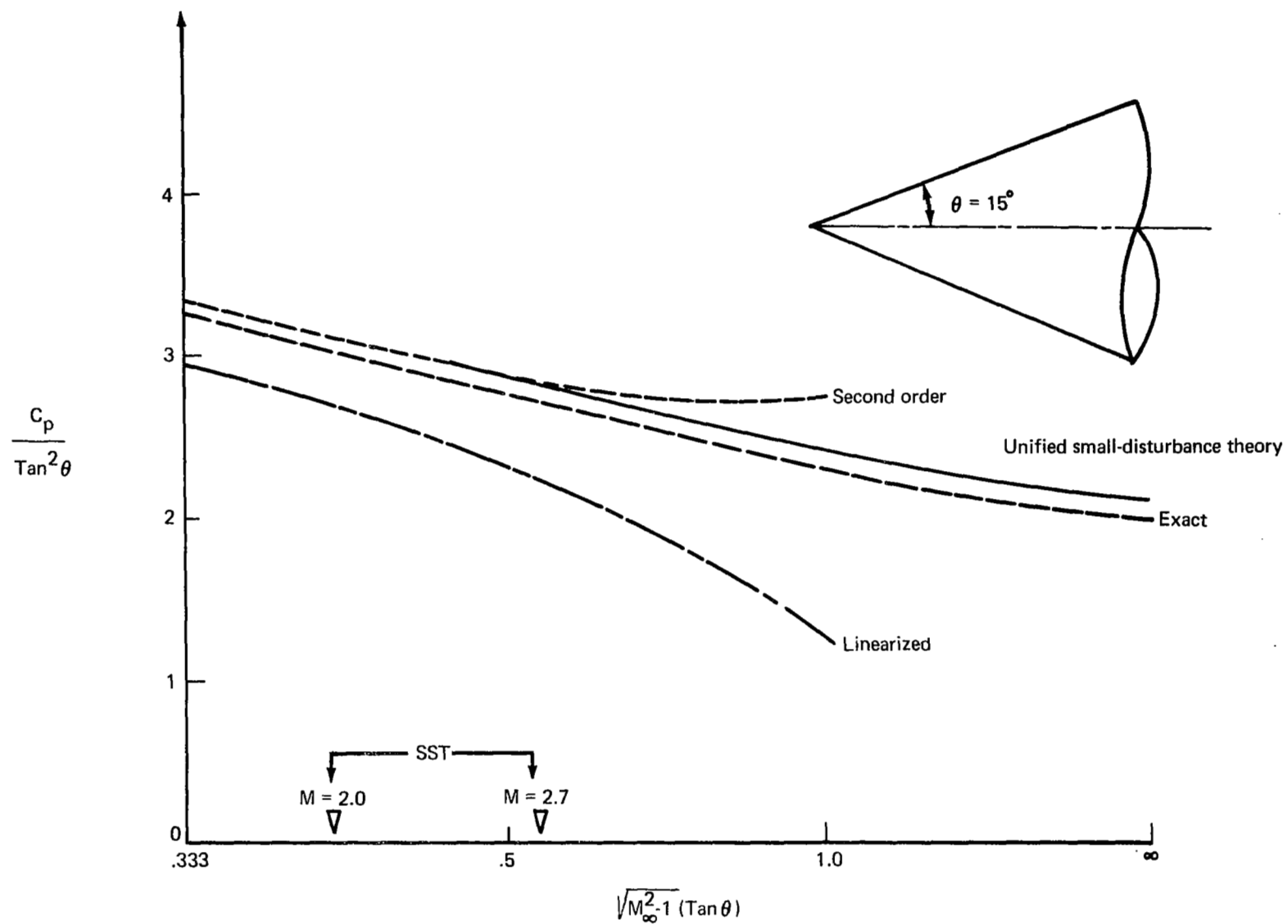


FIGURE 3.—ACCURACY OF THE UNIFIED THEORY FOR FLOW OVER A CONE

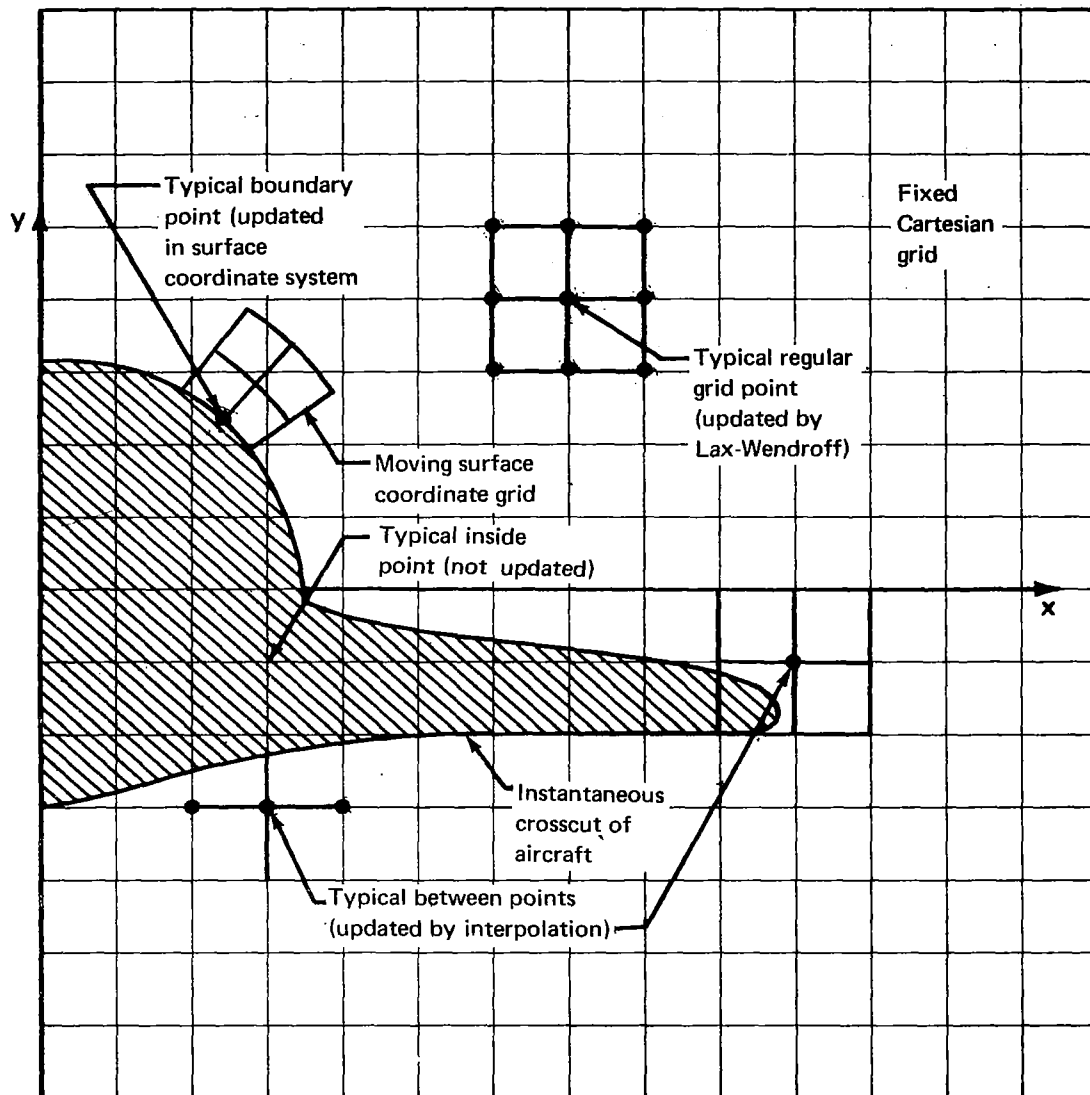


FIGURE 4.—GRID SYSTEM IN CROSS-FLOW PLANE

The state of mesh is very fluid in that, as time progresses and the contour deforms, the Cartesian points are continuously being interchanged within the above three classes. The flow properties of these points are determined quite differently.

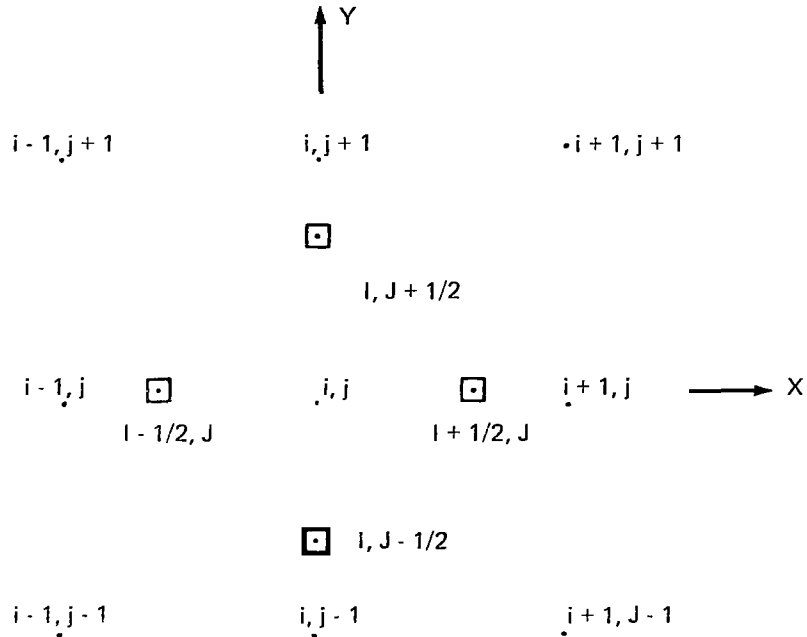
Differencing method for update of regular grid points.—The equations of motion (7) through (12) are nondimensionalized and written in conservative form as

$$\frac{\partial W}{\partial t} + \frac{\partial f}{\partial x} + \frac{\partial g}{\partial y} = 0 \quad (13)$$

where

$$\begin{aligned} W &= [\rho, \rho u, \rho v, E] \\ f &= [\rho v, p/\gamma\beta^2 + \rho v^2, \rho vu, v(p(\gamma - 1) + E)] \\ g &= [\rho u, \rho uv, p/\gamma\beta^2 + \rho u^2, u(p(\gamma - 1) + E)] \\ \beta &= \sqrt{M_\infty^2 - 1} \\ E &= p + \frac{1}{2} \rho (v^2 + u^2) \gamma (\gamma - 1) \beta^2 \end{aligned}$$

The numerical scheme for updating the regular grid points proceeds as follows



The properties are known at time t at the nine points shown above denoted by a dot (.). The first step in the two-step method is to determine W at the four squares at time $t + \Delta t/2$. For example,

$$\begin{aligned} [W_{I+1/2, J}]_{t+\Delta t/2} = & \left[\frac{W_{i+1, j} + W_{i, j}}{2} \right]_t - \frac{\Delta t}{2} \left\{ \frac{1}{\Delta x} (f_{i+1, j} - f_{i, j})_t + \right. \\ & \left. \frac{1}{2\Delta y} \left(\frac{g_{i, j+1} + g_{i+1, j+1}}{2} - \frac{g_{i, j-1} + g_{i+1, j-1}}{2} \right)_t \right\} \end{aligned}$$

From the values of W at $t + \Delta t/2$ f and g are computed at the square points at $t + \Delta t/2$.

The second step then calculates $W_{i,j}(t + \Delta t)$ as follows:

$$\begin{aligned} [W_{i, j}]_{t+\Delta t} = & [W_{i, j}]_t - \Delta t \left[\frac{f_{I+1/2, J} - f_{I-1/2, J}}{\Delta x} + \frac{g_{I, J+1/2} - g_{I, J-1/2}}{\Delta y} \right]_{t+\Delta t/2} + \\ & O(\Delta x^3, \Delta y^3, \Delta t^3) \end{aligned}$$

The differencing system described has been found to be generally quite stable so long as the flow satisfies the Courant Friedrichs condition. Mathematically, this requires that the maximum time step size Δt , at each state in the computations, is limited by

$$\Delta t \leq \frac{\Delta x}{(q + a)\sqrt{2}} \Big|_{\max}$$

where q is the speed of flow and a the speed of sound. The above stability condition ensures that numerical signal speed is always greater than the rate at which the physical sound waves propagate ($q + a$).

Differencing method for update of body points.—To update the points on the moving contour is perhaps the most crucial task in the method. To understand the philosophy, it is helpful to examine figure 5. The local surface coordinate system associated with point P (also called point 2) is shown attached to the contour as well as the basic Cartesian mesh. The eight points in the surface coordinate system surrounding point P are determined as follows. First, points 1 and 3 are located on the contour a distance Δs on either side of point 2. Points 4 and 7, 5 and 8, and 6 and 9 are located Δn and $2\Delta n$ away from the contour surface along contour normals through points 1, 2, and 3, respectively. The arc length and normal directions are computed from knowledge of the analytic contour definition.

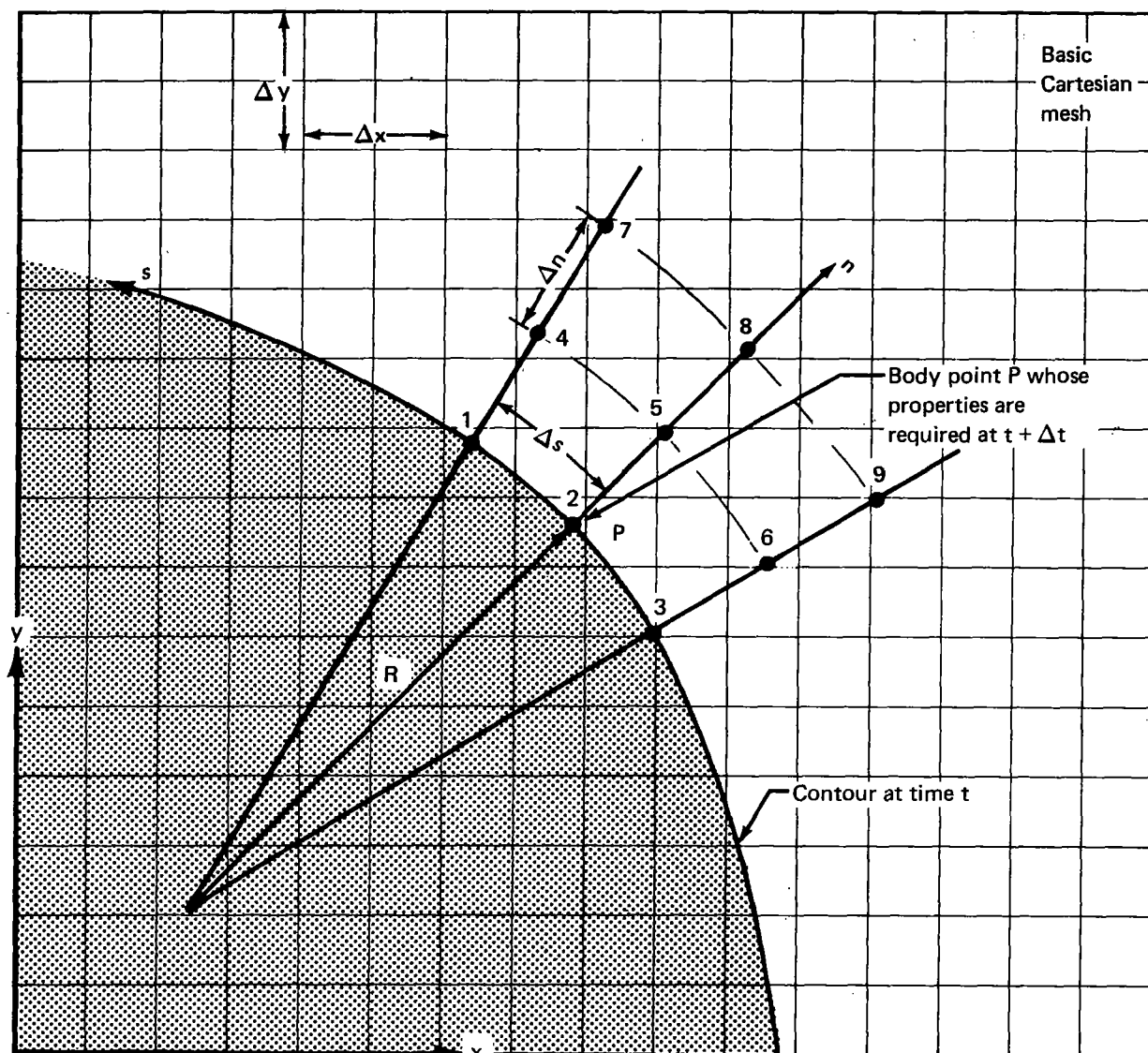


FIGURE 5.—CONSTRUCTION OF SURFACE COORDINATE SYSTEM TO UPDATE SURFACE PROPERTIES

The flow properties are known at the boundary point P at time t as well as the properties at the other boundary points (not shown) and the rectangular Cartesian grid points. The problem then is to determine the flow properties at point P (as well as the other boundary points) at the new time level $t + \Delta t$. During this time, the contour moves. To update point P , the flow properties at the other points (1, 3, 4, 5, 6, 7, 8, and 9) must also be known at time t . The properties at points 1 and 3 are determined by interpolation along the contour from the other boundary points at times t . The properties at points 4 through 9 are determined by interpolation from the Cartesian mesh points. This latter step is done by first determining which Cartesian square the point lies in, and then performing bilinear interpolation.

The actual updating of the flow quantities is then done in a moving coordinate system by one of two optional methods. The first method, called BND1, was developed at Boeing and updates point P in a manner that maintains the conservative nature of differential equation (13). The second method, called BND3, relies on the method of characteristics to update the boundary point. This second method has been used extensively by Moretti (ref. 12). The details of BND1 and BND3 are given in appendixes A and B. Experience has shown that the treatment of body points is usually a delicate matter, so it was felt desirable to have the separate methods available as options.

Update of between-grid points.—Having updated the regular grid points, using Lax-Wendroff, and the surface grid points, using either BND1 or BND3, it now remains to update the between-grid points (see fig. 4). These points are updated by interpolation from the updated regular grid points and updated surface grid points using a Laplace-type star. Since several between-grid points may be located on the same horizontal or vertical, point relaxation is used and the between-grid points are updated very quickly in an iterative manner.

Geometry Definition

Since the step size Δt is controlled by the program stability criterion, the capability of defining the crosscut contour at any station must be provided. This is accomplished as follows: The body is divided into a number of "interpolation sections" along the time-like z-axis. A crosscut contour is given at each end of an interpolation section, and it is defined by the x,y coordinates of selected points. The number of points on each contour pair is taken to be equal. To locate points on an intermediate contour, a curve connecting corresponding point pairs is interpolated. Although the number of contour points used in a particular interpolation section is fixed, it can vary from one section to the next.

The pointwise definition of the crosscut contour is rendered continuous by fitting a cubic spline. This spline is allowed to have slope or curvature discontinuities at specified interior points. The user must give the tangent angle or curvature on each side of a discontinuity point.

For several simple geometries, special subroutines were written that generate the interpolation section information directly using parameters given by the user. The treatment for general bodies is outlined in appendix C, and an example is given in appendix D.

Initial Conditions

Hypersonic small-disturbance equations (7) through (12) require initial conditions to complete the problem definition. The logical place to impose the initial condition is at the nose of the aircraft ($t = 0$). However, at the nose of the aircraft, equations (7) through (12) are either singular (for example, with a pointed body) or not applicable (for example, a blunted body). In addition, the numerical method requires that the geometry cross-section size be at least several mesh spaces. For these reasons, it is necessary to commence the flow a short distance downstream of the nose. The task is then how to determine the flow conditions at this downstream location. While several approaches came to mind, during the present contract period, the simplest "impulsive start" method was used most extensively. This method is illustrated in figure 6 for an axisymmetric body. Upstream of $t = 0.2$, the flow is uniform and at $t = 0.2$ it is impulsively disturbed by the body. As might be expected, and experience indeed verifies, downstream of this impulse or body extension, the flow approaches the same condition as if the extension were not present. Later in the program, use was made of the tangent wedge and tangent cone method so as to provide more realistic initial conditions. This is also shown in figure 6. As was expected, this allowed a shorter region for initial transients to decay.

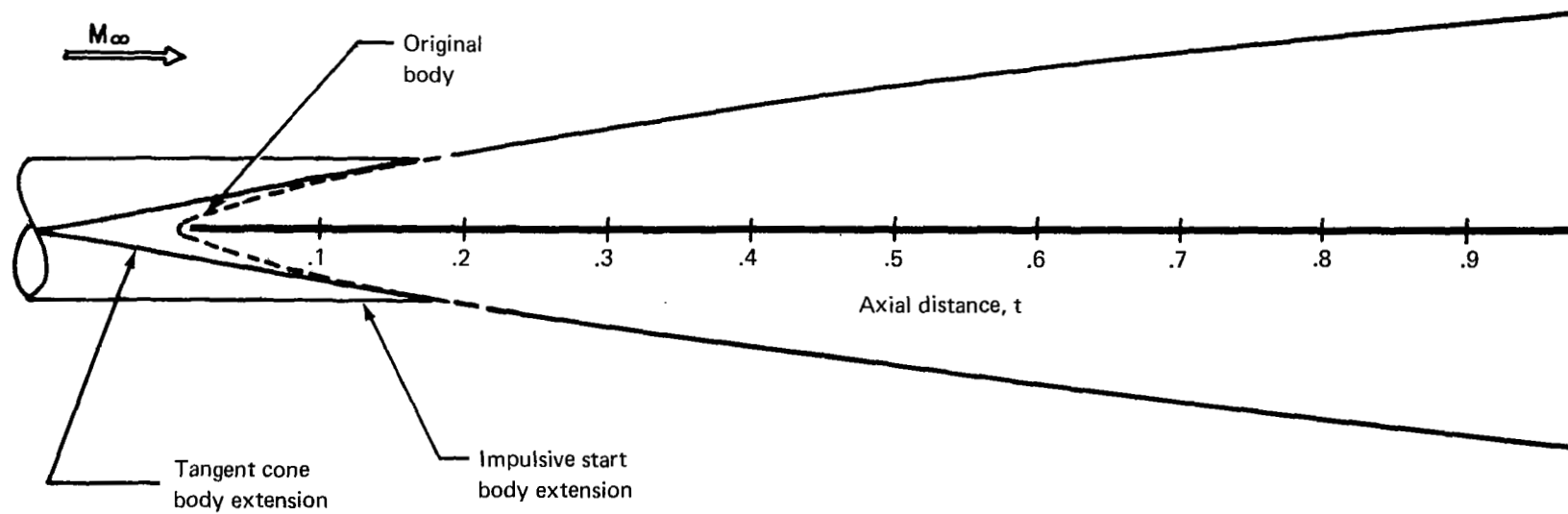


FIGURE 6.—MODIFICATION OF BODY TO ALLOW FOR AN IMPULSIVE START OR TANGENT CONE START

COMPUTER PROGRAM USE

The present method for solving supersonic/hypersonic flow problems is contained in a single overlaid program. The program is coded in CDC FORTRAN 2.3 language for the CDC 6400/6600 computers and the SCOPE 3.1 operating system.

The following sections will give an overview of the program in operation and discuss its use. Complete descriptions of the card input are given. Test cases and a detailed description of the computer program are found in Part II of this report.

Program Elements

The program was designed to ensure that the total field length could be less than 70000g. To accomplish this, the OVERLAY feature of the loader is used. This allows a complete program to be divided into smaller programs that are called by the main overlay. Also, geometry and flow data storage requirements are alleviated by using high-speed disc storage.

The overlay structure is shown in figure 7. The initialization overlay (INIT) is called only once at the beginning of program execution, at which time it allocates information used in the time integration loop. The remaining primary overlays are called repetitively to perform the specific tasks necessary to take a time step. The calling order is indicated by the numbers in figure 7.

The user chooses one of the boundary update programs—BNDRY (displaced conservative scheme) or BNDRC (reference plane characteristics scheme)—for use in a particular run segment. FINDCT interpolates for the crosscut contour at the new time level. MAPS locates intersections of the Cartesian grid lines with the new contour and generates "maps" of inside, between, and Lax-Wendroff grid points. The latter information is used in LAXWDF and BETWN to control the update schemes used for the field points. RESET and STBPRN determine the time step size and do some bookkeeping.

The array A in the main overlay program TEA270D is used in the primary overlays for temporary storage of geometry and flow data brought into core from disc. The program has been designed so that the length of this work area and, hence, the field length of the program can be changed by altering a single card in the program.

All input cards are read by the initialization overlay. Using these parameters, it performs three functions:

- 1) Sets parameters controlling the numerical solution procedure including grid size, choice of boundary update procedure, storage allocation, data output, and termination of execution.
- 2) Generates crosscut contour interpolation information and stores it on disc for later use by FINDCT.
- 3) Initializes the flow arrays using either the freestream flow conditions (impulsive start) or restart data stored on magnetic tape in a previous run.

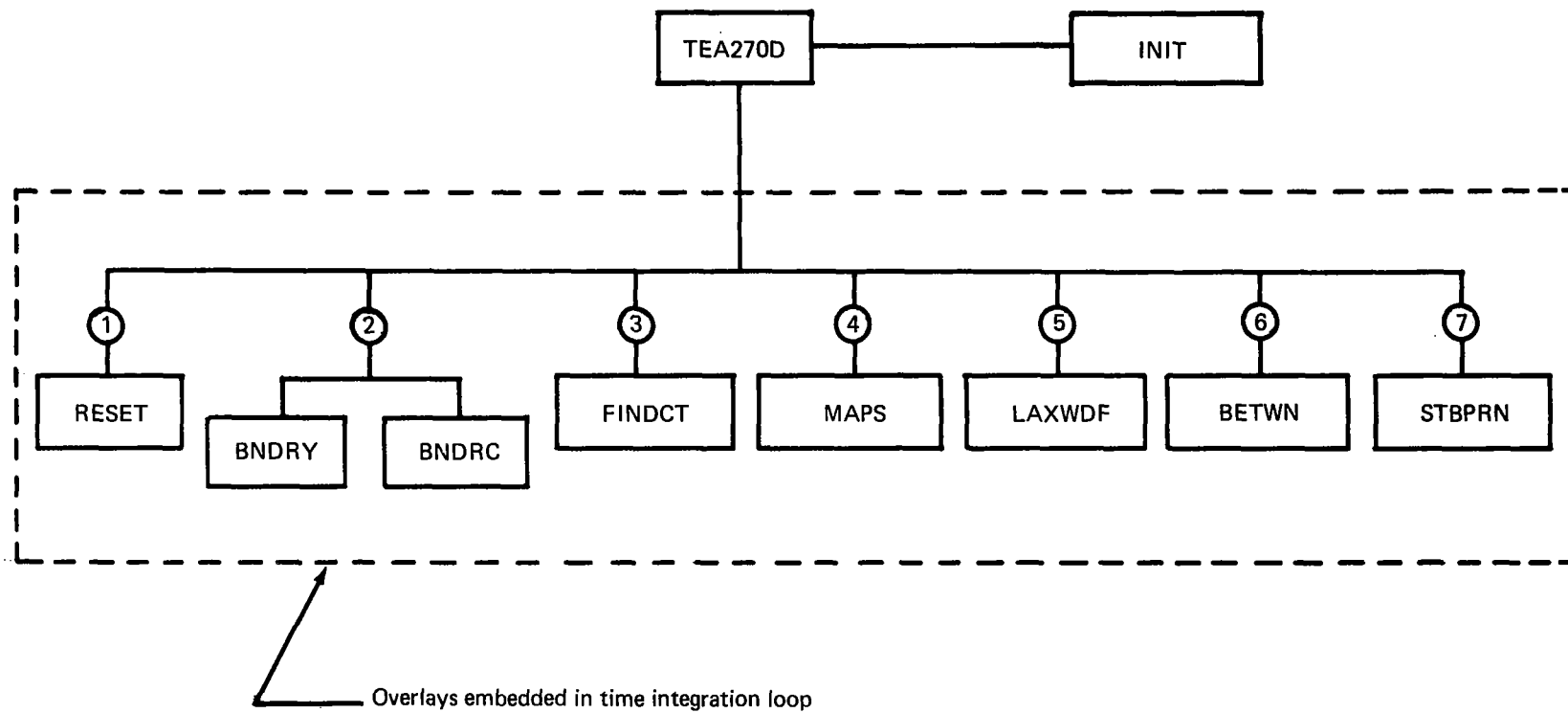


FIGURE 7.—PROGRAM OVERLAY STRUCTURE

There are six different geometry generation packages that can be used in the initialization overlay. They are

- 1) CONBOD—General conical bodies with a given Jordan curve* as directrix
- 2) ELLBOD—Bodies with elliptic cross sections and specified axial variation of the semi-minor and semimajor axes; axisymmetric bodies treated as special cases
- 3) SLBDEL and SLBDEL CUSP—Slab delta wing geometry with either a circular or cusped leading edge
- 4) SLBDEL APPROX—Approximate slab delta wing geometry except that curvature is continuous
- 5) CONE SLBDEL and CONE SLBDEL CUSP—Simple wing-body geometry consisting of a circular cone and a slab delta wing with either a circular or cusped leading edge
- 6) REDBOD—General bodies with Jordan curves as crosscut contours

The first five packages are for special geometries actually treated during the contract period. The last package is quite general and allows the program to treat almost any simple wing/body combination.

To prevent the initialization overlay from becoming too large, the geometry generation packages were made interchangeable. That is, the subroutines in each package are given the same FORTRAN name BODGOM for the primary subroutine, and BGAUX1, BGAUX2, etc., for subsidiary subroutines. The names given above are functional names assigned to differentiate the packages.

For each run, the user normally has to compile the geometry generation package that will be used. This leads to the recommended running configuration shown in figure 8. In it, it is assumed that a binary list of the compiled program is contained on TAPEA, and, on TAPE10, binary data will be stored to restart the program. The correction decks would include the geometry generation package as well as TEA270D if the total field length is to be changed.

Two routines are included in INIT to initialize the flow arrays. START1 embodies the impulsive start procedure, that is, all flow variables are set to their freestream values. It is used at the beginning of a sequence of runs. START2 is used to restart the program from data previously saved on magnetic tape.

The save-tape and restart capabilities provide flexibility in running cases. It allows long runs to be separated into smaller, more manageable segments. Each segment can include a given number of time steps or a given axial distance or require a given amount of CPU time; all these are included as options for terminating program execution.

*A Jordan curve is one that is continuous, does not fold back on itself, and has continuous left- and right-hand derivatives at any given point.

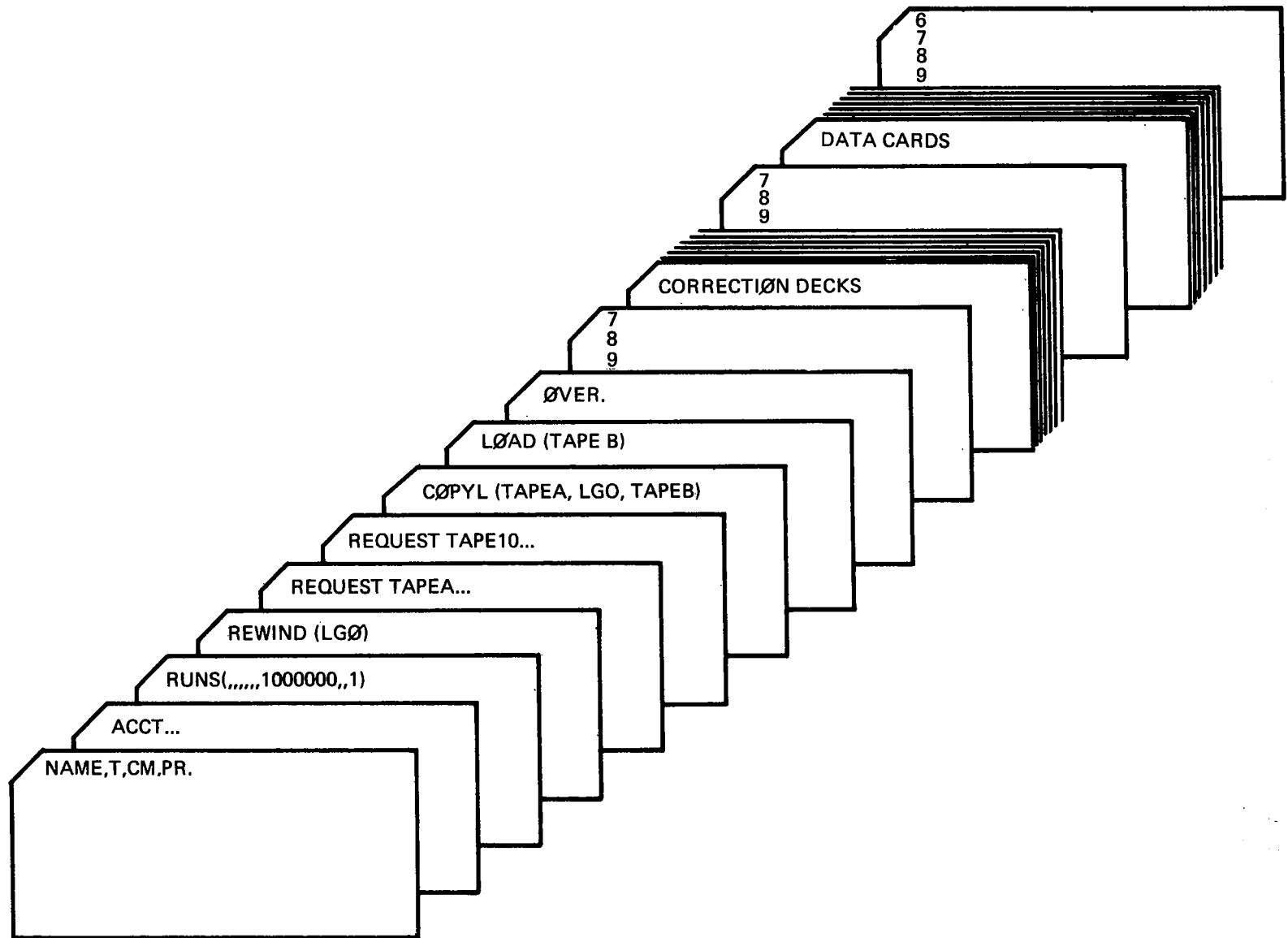


FIGURE 8.—COMPUTER DECK SETUP

A large amount of printed output can be provided to analyze the results of a particular run segment. This can range from summary output to detailed output useful for debugging or understanding the program, at the user's option. In general, however, the output should be kept to the minimum required by the user. A detailed output can require a considerable amount of CPU time. The output given by the program will be discussed further under "Printed Output Data."

Input Data Preparation

Input data consist of free-field titles, control words, and numbers. Control words are used only as input to the geometry generation packages. With one exception, decimal points should always be punched for every input number; the exceptional card is noted in the discussion below (card 8).

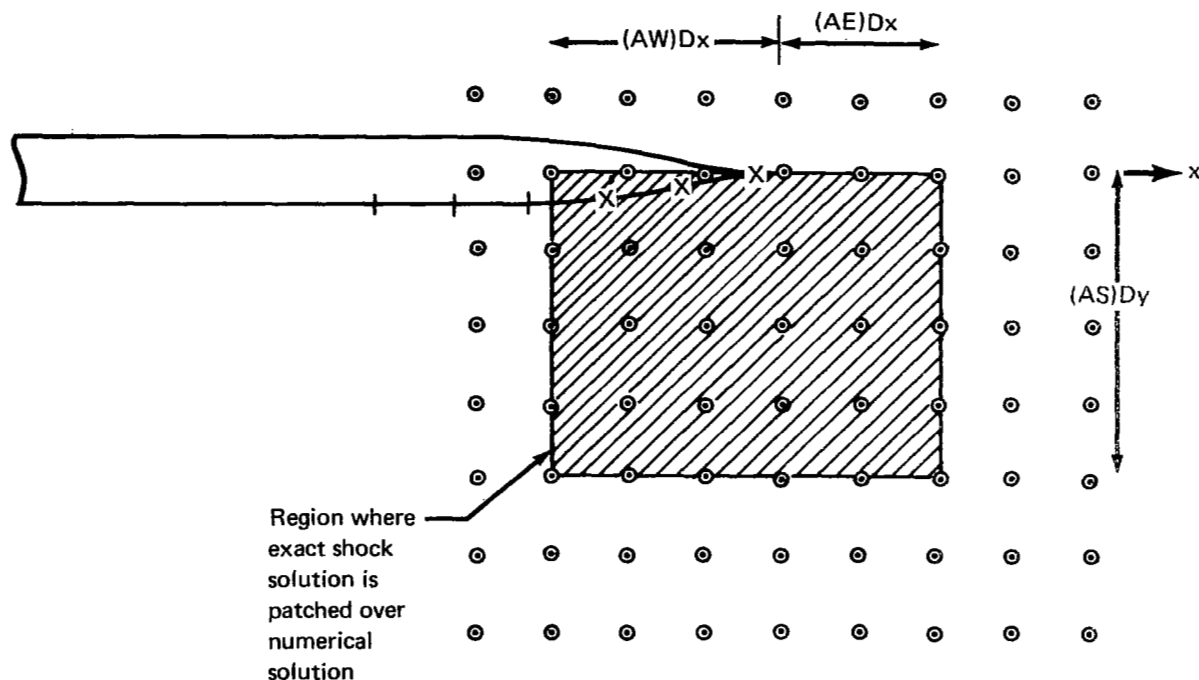
The input data cards are described below. Practical advice as to the selection of some of the variables is given later in "Comments on Program Use."

	<u>Code</u>	<u>Column</u>	<u>Explanation</u>
Card 1	TITLE	1-80	Title for the case being run
Card 2	NX	1-10	Number of Cartesian grid lines cutting x-axis
	NY	11-20	Number of Cartesian grid lines cutting y-axis
	MDY	21-30	Number of grid spaces between lower boundary of the Cartesian grid and the x-axis
	DX	31-40	Cartesian mesh step size in the x-direction
	DY	41-50	Cartesian mesh step size in the y-direction
	DS	51-60	Local tangential surface coordinate increment
	DN	61-70	Local normal surface coordinate increment
Card 3	UNIFY	1-10	Small-disturbance theory option— = 0.0; hypersonic theory used = 1.0; unified supersonic/hypersonic theory used
	FSMN	11-20	Freestream Mach number of flow
	GAMMA	21-30	Ratio of specific heats
	ALFAD	31-40	Angle of attack in degrees
Card 4	BND	1-10	Boundary update option— = 1.0; displaced conservative scheme = 3.0; reference plane characteristics scheme
	BNDISC	11-20	Discontinuity point option— = 0.0; standard boundary update scheme at all boundary points = 1.0; interpolation scheme (used at points where the slope and/or curvature are discontinuous)
	BNDPRN	21-30	Detailed printout option— = 0.0; no printout from BND1 or BND3 = 1.0; summary printout of steps taken in BND1 or BND3

	<u>Code</u>	<u>Column</u>	<u>Explanation</u>
Card 5	NCTMX	1-10	Maximum number of contour points expected in a certain run segment; can vary between runs
	NBTMX	11-20	Maximum number of between-grid points allowed for all run segments associated with a case
	KX	21-30	Twice the maximum number of intersections of grid lines parallel to the y-axis with the crosscut contour
	KY	31-40	Twice the maximum number of intersections of grid lines parallel to the x-axis with the crosscut contour
Card 6	NPRNT	1-10	Controls printed output defining flow properties at Cartesian grid points: output given every NPRNT time steps; no output given if NPRNT = 0.
	NBUG	11-20	Controls detailed (debug) printed output related to field point update: output given every NBUG time steps; no output given if NBUG = 0.
	NSAVE	21-30	Controls how often binary output is saved on magnetic tape for restarting program execution; data are saved every NSAVE time steps; no restart data are saved if NSAVE = 0.
Card 7	TMX	1-10	Program execution is terminated when the axial station is greater than or equal to TMX.
	NTMX	11-20	Program execution is terminated when the total number of time steps (all run segments) is NTMX.
Card 8	IOCTL	1-10	Program execution is terminated before the run CP time (in octal seconds) is exceeded; this number should be the same as given on the first control card in the deck and is a fixed-point octal number that must be right adjusted.
Card Set 9			This is the card set read by the particular geometry generation package being used; the specific data cards are discussed in appendix D.
Card 10	NSTART	1-10	Flow array initialization option— = 1.0; START1 is called = 2.0; START2 is called
Card 11	TSTART or FLSTART	1-10	If NSTART = 1.0; input the axial distance (TSTART) at which integration is to begin. If NSTART = 2.0; input the file number (FLSTRT) of the file on the restart tape to be used to restart the computation.
Card 12	FILSAV	1-10	The file position on the restart tape at which the program should begin saving data for this run segment

	<u>Code</u>	<u>Column</u>	<u>Explanation</u>
Card 13	STRTTYP	1-7	If STRTTYP = CONSTRT, the initial flow field is computed from cone tables, assuming zero angle of attack. If STRTTYP = TANWEDG, the initial flow field is computed by using the tangent wedge method. If STRTTYP is not CONSTRT or TANWEDG, the initial flow is set at freestream.
Card Set 14			If STRTTYP = CONSTRT then card set 14 consists of card 14A and card set 14B.
Card 14A	BKD	1-10	Surface slope in degrees (semiangle of starting cone)
	FX	11-20	Shock slope angle—a constant from Babenko's cone tables (ref. 13)
	R1	21-30	Radius of initial cross-section that must be circular
	ANTAB	31-40	The number of cards in card set 14B
Card Set 14B			This set consists of ANTAB cards. A typical card is described:
	XI	1-10	Distance from cone surface to shock
	F1(XI)	11-20	Value of v from cone tables
	F2(XI)	21-30	Value of p from cone tables
	F3(XI)	31-40	Value of ρ from cone tables
Card Set 14			If STRTTYP = TANWEDG, then card set 14 consists of a single card, card 14.
Card 14	ALAMD	1-10	Sweepback angle of wing in degrees
Card Set 14			If STRTTYP is not CONSTRT or TANWEDG, then this card set contains no cards.
Card 15	TIPSOL	1-5	If TIPSOL = PATCH, then a solution is patched in under the wing tip. If TIPSOL is not equal to PATCH, then no special action is taken.
Card Set 16			If TIPSOL is not equal to PATCH, then this card set contains no cards. If TIPSOL = PATCH then card set 16 consists of two cards—card 16A and card 16B.
Card 16A	ALAMD	1-10	Sweepback angle in degrees
Card 16B	AS	1-10	
	AE	11-20	
	blank	21-30	
	AW	31-40	
	ABOUND	41-50	

The variables AS, AE, AW, ABOUND of card 16B are explained with the help of the sketch below. In this sketch, AS = 4.0, AE = 2.0, AW = 3.0, and ABOUND = 3.0. The solution is patched in at the grid points marked with circles and at the boundary points marked with crosses. The first point to the right (east) of the tip is the reference point from which AS, AE, and AW are recorded.



The card input from each geometry generation package is given in appendix D. A short explanation of the primary function of each package and a discussion of the options is also included. Note that the following assumptions are made concerning crosscut contours:

- 1) The crosscut contour at any time is a closed Jordan curve with a fixed line of symmetry.
- 2) The contour is continuously differentiable in the vicinity of the line of symmetry and has zero slope on the line of symmetry.
- 3) Only the right-half contour ($x \geq 0$) is actually considered.
- 4) The half-contour is defined pointwise beginning with the bottom symmetry point.

The geometry data placed on disc for later use in the integration loop consist of crosscut contour pairs at user-specified axial stations. These "interpolation sections" are generally defined on the last set of geometry data cards after all contour generation parameters are read. The REDBOD package is an exception. In it the crosscut contour pairs are read directly from data cards; they are not generated.

Printed Output Data

The computer printout is intended to be self-explanatory. Its salient features and the options available will be discussed here. Sample cases are given in Part II of this document.

The standard printed output can be divided conveniently into three categories:

- 1) Preliminary output data
- 2) Data output within the time integration loop
- 3) Data output at the end of execution

Part of the preliminary output lists the input data. This listing establishes a record of the run and is useful for pinpointing input errors. Information generated in the initialization overlay is also summarized. This includes output from the geometry generation package and one of the start sub-routines. Of particular interest is the CORE STORAGE ANALYSIS. This shows the storage required by certain crucial subroutines and specifies the manner in which Cartesian grid data are subdivided into blocks.

There are four levels of data output within the time integration loop, depending on the parameters BNDPRN, NPRNT, and NBUG. The basic output gives Cartesian flow properties at boundary points, defines the crosscut contour at the new time level, and gives CP and PP times used in each overlay and for the complete time step. With BNDPRN=1 output is given at each time step adequate to follow in detail the update procedure at each boundary point. The remaining levels of output are given every NPRNT and NBUG time steps, respectively. Output of flow properties at all Cartesian grid points is controlled by NPRNT. This output is given by blocks according to the disc storage scheme, and flow properties inside the crosscut contour are always set to -2. NBUG controls output from the MAPS and BETWN overlays. The output from MAPS includes Cartesian grid/contour intersection information and the "maps" of outside and between-grid points (in octal form). The output from BETWN allows one to follow the between-grid point update procedure.

The output controlled by BNDPRN, NPRNT, and NBUG is quite extensive. It should only be requested when needed because it can cause CPU time to increase considerably.

At the end of a run, information is given that summarizes the data stored on the restart tape during the run. These data are output every NSAVE time steps and at the end of the run. The reason execution was terminated is also given.

In addition to the standard output, diagnostic information is output when a fatal execution error is encountered in one of the subroutines. A programmer can then resolve or explain the difficulty.

Comments on Program Use

In this section, the user is given some practical advice on the effective operation of this program. While there is no substitute for first-hand experience, it is hoped that the following comments will be helpful. A natural way of introducing this information is to describe the motivation for choosing various parameters, as was done under "Input Data Preparation." In what follows, reference is made to that section. Only variables that are not self-evident will be discussed.

Card 2 contains the significant geometry information. The Cartesian grid is bounded by a "solution rectangle" formed by the outermost gridlines and the axis of symmetry. The size of the solution rectangle is chosen so that the bow shock is contained within the mesh boundaries during a particular run segment. This is necessary because freestream boundary conditions are enforced on the outermost gridlines, and these conditions are inappropriate after shocks arrive. If there is interest only in surface values, the run can be somewhat longer because the initial reflection waves from the outer boundary take some time to reach the contour surface. An estimate of the shock extent is usually based on experience, experimental data, or some simple theoretical estimate. The solution rectangle should not be chosen too large as its size influences run time.

Having an estimate of the outer grid dimensions, the mesh step sizes (Δx , Δy , Δs and Δn) must be selected. These values are chosen so that the expected flow detail can be accurately represented. The smaller these quantities are chosen, the more accurate will be the results. However, to avoid large computer run times, they should not be chosen too small. Table 1 in the "Results" section provides some typical values.

Generally, the four quantities are all made equal. Once the mesh step sizes are selected and the geometry scale decided, NX and NY can be determined easily by dividing the solution rectangle width and height, respectively, by the step size. MDY is chosen so as to position the crosscut contour along the y-axis in such a way that the expected flow field is contained within the mesh. Thus, if the windward shock is expected to lie closer to the cross-section contour than the leeward flow, the cross-section would be moved down from the center of the y-axis.

Card 4 contains information that is significant for the update of the boundary properties. First, a choice must be made between the two update schemes BND1 and BND3 (see apps. A and B). Experience has been that each of these methods has advantages and disadvantages. The "Results" section and table 1 give examples using the two methods. The following general observation and advice is given. For flows without geometric surface discontinuities and with shock waves at least five or six mesh points away from the contour surface, both BND1 and BND3 give essentially the same results—BND3 perhaps being more efficient. For the supersonic delta wing cases, BND1 worked best; for the hypersonic cases, BND3 was used. Understanding of the behavior of these two methods is yet incomplete, particularly when discontinuities are present. Should one technique give unreasonable results, the other should be tried.

The value of BNDISC in card 4 allows crosscut geometry points to be treated, where discontinuities occur, in one of two ways. When BNDISC = 0.0, the contour points are updated at geometric discontinuity locations without modification of the update scheme. This can be somewhat risky as the density may become negative. More recent experience indicates that the second way, BNDISC = 1.0, is advisable.

Card 5 contains information needed to partition the computer work array. A good estimate for NBTMX is the integer nearest $1.5 \cdot \text{PER}/D$ where

$$\text{PER} = \text{estimated maximum curve length of a half-contour } D = (DX + DY)/2$$

It is best to overestimate NBTMX (hence, the factor 1.5) because, with the current program, it cannot be increased in subsequent restarts.

With card 6, the recommended value for NPRNT used is 10. This causes the complete flow field to be printed out every 10 time steps. To limit printout, a smaller value is not recommended. The recommended value of NSAVE is 10. This causes all the data required for a restart to be saved every 10th time step. In the event of a mishap, not more than 10 time steps are lost.

Card 7 contains information for terminating a run segment. The use of this card is best understood by first considering the transient effects. These effects play an important part in obtaining meaningful solutions. The time required for the impulsive start transients to decay depends in a complicated way on Mach number, geometry, and the angle of attack. The user is advised to proceed as follows. For the first segment of the run, TMX is set at the length of the aircraft (or to a large number for a conical body) and NTMX is set at 10.

After 10 time steps, the user can check over the results and be sure that all is well. The program is thereafter run in segments of approximately 50 time steps (NTMX set at 50.0). The user then can chart the progress of the run and decide when the starting transients have decayed sufficiently. For a conical flow, once the starting transients have decayed sufficiently, the run may be stopped.

Nonconical cases are easiest to treat when they have a conical foreflow. First it must be established that the conical foreflow portion is free of starting transients before proceeding on downstream to the nonconical portion of the flow.

Card 12 contains information regarding use of input tapes. If NSTART = 1.0; card 12 should be blank. The first batch of restart data is saved on file one of the tape. If NSTART = 2.0, the first batch of restart data from the run is saved on file number FILSAV, which must be less than or equal to (FLSTRT + 1.0). The usual value of FILSAV is (FLSTRT + 1.0).

Card set 14 allows various initial conditions to be applied. Experience indicates that the tangenet wedge and cone starts are much preferable to the impulsive start. It is important when using these that at least several grid points are located between the body and the shocks. For a fixed step size, this can be accomplished by initializing the flow sufficiently aft of the nose.

Card set 15 was set up for an experiment and allows the user the capability of inputting the leading edge shock for the lower surface of flat delta wings. This capability is currently only available for supersonic leading edges with attached shock waves. The constants AE, AW, and AS allow the extent of the patch to be varied. AE is chosen as one or two but AS and AW should be chosen so that there will be several mesh points between the leading edge shock and the delta wing surface. On the other hand, the size of the patch should not be so large that the actual flow that exists away from the leading edge is misrepresented.

Several additional comments will next be made concerning the use of the geometry packages described in appendix D and required in card set 9 of the “Input Data Preparation” section of the main text. It has been found that the best accuracy occurs when the contour points are input in such a way that the distance between two contour points is always approximately equal to Δs (the arc length increment used in the boundary update scheme—card 2).

Thus, for example, in card set 5 of appendix D, the axial increments between locations T1 and T2 ($T2-T1$) and the number of contour points NC are chosen so that the contour arc spacing between contour points is always approximately equal to Δs .

For geometry routines that use the cubic spline fit to define contours, boundary point location influences the quality of the cubic spline fit. Point density in regions of high curvature is especially important. A good rule of thumb is not to allow the acute angle between successive chord lines to exceed 30° . Beware the fact that this rule is scale independent, so it applies even to contour segments of small dimension. There should not be a rapid variation in point spacing, as this could adversely affect the quality of the spline fit and flow properties.

Using the hints provided in this section and the sample run cases in Part II, and using as examples the results given in the “Results” section following, the user should be able to obtain good results quickly. As experience with the program develops, increasingly sophisticated cases can be analyzed.

RESULTS

The computer program was used to test the numerical solution to the unified small-disturbance equations for a variety of geometries and flow conditions. The geometries considered were a cone, several axisymmetric bodies, elliptic cones and elliptic cone/wedge, delta wings, and cone/delta wing combination. The cases were selected so as to allow comparison, where possible, of the present method with other methods as well as with experimental data. These cases allow a fairly extensive test of the method and were selected to establish the accuracy of the technique for both simple type flows, such as for a cone, as well as for the very complicated singular-type flows, such as presented in the delta wing and wing/body cases. For all the cases considered, unified theory was used and γ was set at 1.4. Table 1 lists the significant run variables.

**TABLE 1.—NUMERICAL VALUES OF SIGNIFICANT PARAMETERS USED IN
COMPUTER RUNS FOR FIGURES 9 TO 35**

Figure number	Boundary update ^a	ΔX	ΔY	Δn	Δs	NX	NY	NC ^b
9	BND1	0.005	0.005	0.005	0.005	50	100	19
10	BND1/BND3	0.005	0.005	0.005	0.005	50	100	19
11	BND1	0.005	0.005	0.005	0.005	50	100	19
12	BND1	0.005	0.005	0.005	0.005	50	100	19
13	BND1	0.009	0.009	0.009	0.009	50	100	19
14	BND1	0.009	0.009	0.009	0.009	50	100	19
15	BND1	0.005	0.005	0.005	0.005	50	100	19
16	BND3	0.015	0.015	0.015	0.015	50	100	19
17	BND1/BND3	0.015	0.015	0.015	0.015	50	100	19
18	BND1/BND3	0.005	0.005	0.005	0.005	50	100	19
19	BND1/BND3	0.040	0.040	0.040	0.040	50	100	13
20	BND1	0.005	0.005	0.005	0.005	50	100	37
21	BND1	0.0042	0.0042	0.0042	0.0042	60	90	37
22	BND1	0.0042	0.0042	0.0042	0.0042	50	100	37
23	BND1/BND3	0.005	0.005	0.005	0.005	80	120	37
24	BND3	0.005	0.005	0.005	0.005	80	120	37
25	BND1	0.05	0.05	0.05	0.05	61	121	27/65
26	BND1/BND3	0.05	0.05	0.05	0.05	61	121	27/65
27	BND1/BND3	0.05	0.05	0.05	0.05	61	121	27/53
28	BND1	0.05	0.05	0.05	0.05	61	121	27/53
29	BND1	0.05	0.05	0.05	0.05	101	121	6/89
30	BND3	0.25	0.25	0.25	0.25	101	121	60/150
31	BND3	0.25	0.25	0.25	0.25	101	121	60/150
32	BND3	0.05	0.0125	0.0125	0.05	101	83	21/101
33	BND3	0.05	0.0125	0.0125	0.05	101	64	23/147
34	BND3	0.05	0.05	0.05	0.05	101	121	39/235
35	BND3	0.05	0.05	0.05	0.05	101	121	39/235

^aThe symbols are defined in "Input Data Preparation" section.

^bNumber of contour points; when two numbers are given, the first is for start of run and the second is for end of run.

Cone

The results from the cone cases are presented in figures 9 through 14. Figure 9 illustrates the approach to steady state, after an impulsive start, of the surface density and pressure in a typical run at Mach 5 with a 10° half-angle at zero angle of attack. At each time step, the maximum and minimum values around the perimeter are plotted. Initially, there is a large overshoot that occurs when the shock is very near the cone's surface. However, after 35 steps, the surface values are within 5% of the exact values obtained from cone tables.

Shown in figure 10 are the results for a 10° cone at Mach 6 and at 5° angle of attack. The results compare very well with numerical solution of the exact equations obtained by Babenko (ref. 13). The two results are within 5% agreement.

Figure 11 shows the steady-state pressure distribution for a 10° cone at Mach 5 and a 7.5° angle of attack. It is compared with the exact solution obtained by Babenko and the tangent cone result. The agreement is again excellent. Figure 12 shows the steady-state pressure distribution for a 10° cone at Mach 5 and a 12.5° angle of attack. The lee side expansion leads to a pressure distribution that shows evidence of a recompression shock ($\theta \simeq 160^\circ$).

Figure 13 shows the present results for Mach 3.53 flow over a 15° cone at 20° angle of attack. Also shown in this figure are experimental data as well as the results from Van Dyke's hybrid supersonic theory (ref. 14). The present results agree well with the experimental data, except close to the windward ray. The errors near $\theta = 0^\circ$ are attributed to the rather extreme flow deflection angle ($\sim 35^\circ$) in this region. An additional feature of interest is the shock-like behavior occurring at $\theta = 150^\circ$ on the leeward side of the cone.

Figure 14 shows a plot of the cross-flow Mach number, and the transonic behavior is even more evident. The spreading of the shock waves over several grid points is typical of the numerical scheme. Kutler, using a conical flow program that he developed (ref. 7), also observed this transonic cross-flow behavior for cones.

Axisymmetric Bodies

The results for the axisymmetric bodies (other than the cones) are presented in figures 15 through 17. Most of these results used the impulsive-start technique to initialize the flow. The superior tangent cone start technique was not available in the program when these cases were run. Figure 15 shows the results for Mach 10, and zero angle of attack flow over the power law body generated from the equation $r = 0.15t^{2/3}$. The flow was started impulsively at $t = 0.2$, and subsequent development is compared to the tangent-cone method. Note that, for axial distances greater than about 0.6, the agreement is quite satisfactory. Upstream, however, the greater disparity is due to the impulsive starting conditions.

Figure 16 shows the results of the present method as well as experimental data (refs. 15 and 16), for Mach 5.05 flow over a circular-arc ogive at 5° angle of attack. Figure 17 is for the same configuration except the angle of attack is 15° . For both cases, the results agree well with the data downstream of the initial adjustment period. In figure 17, the two surface update schemes were tried, and both are seen to give essentially the same results.

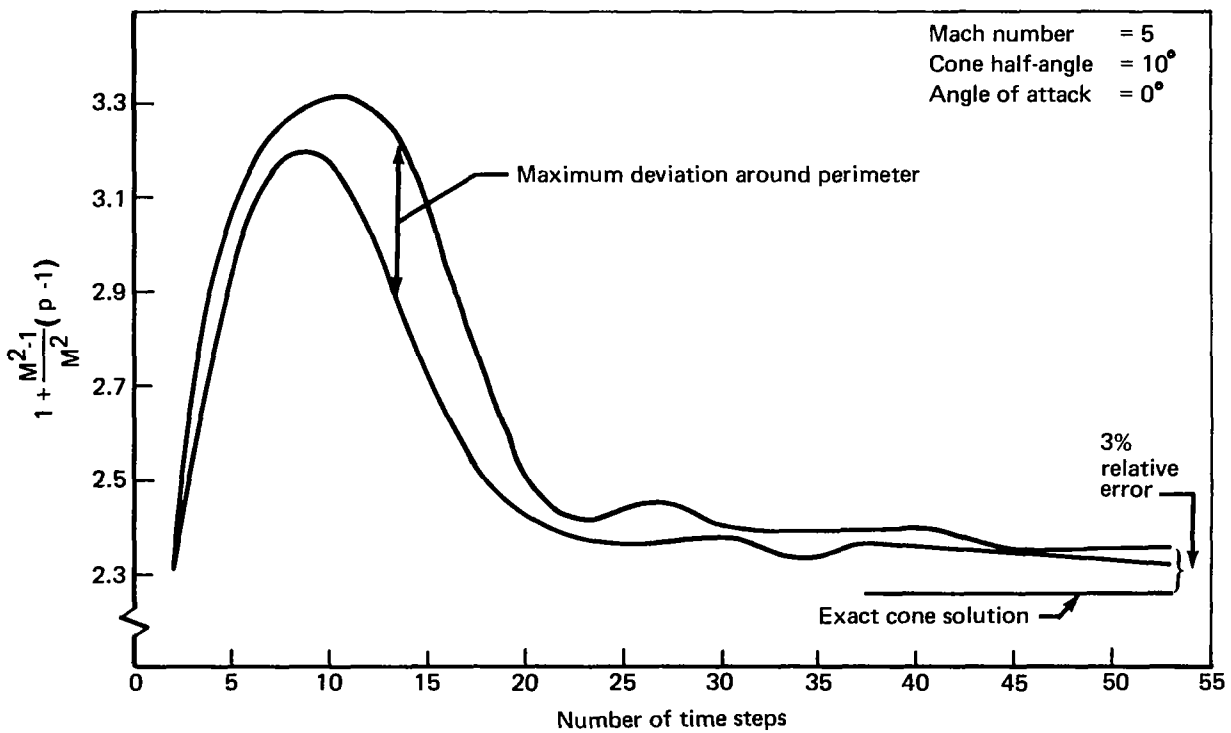
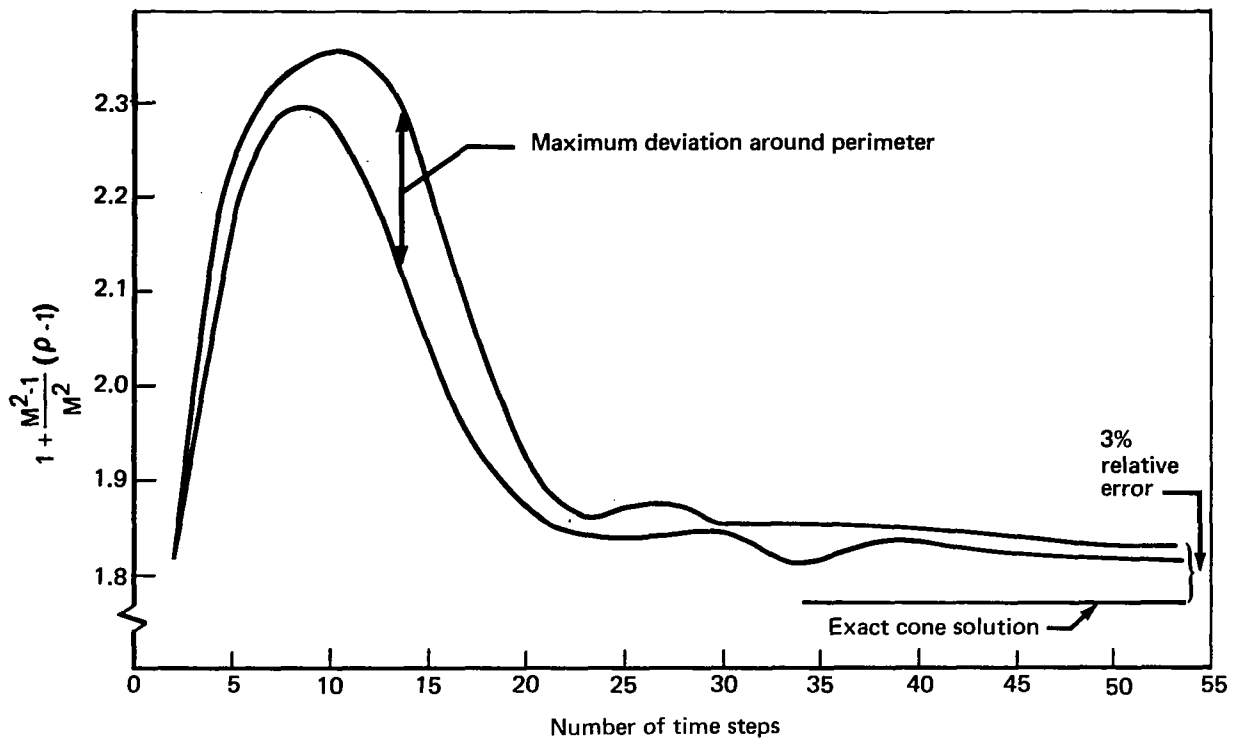


FIGURE 9.—ASYMPTOTIC CONVERGENCE TO A STEADY STATE AFTER AN IMPULSIVE START

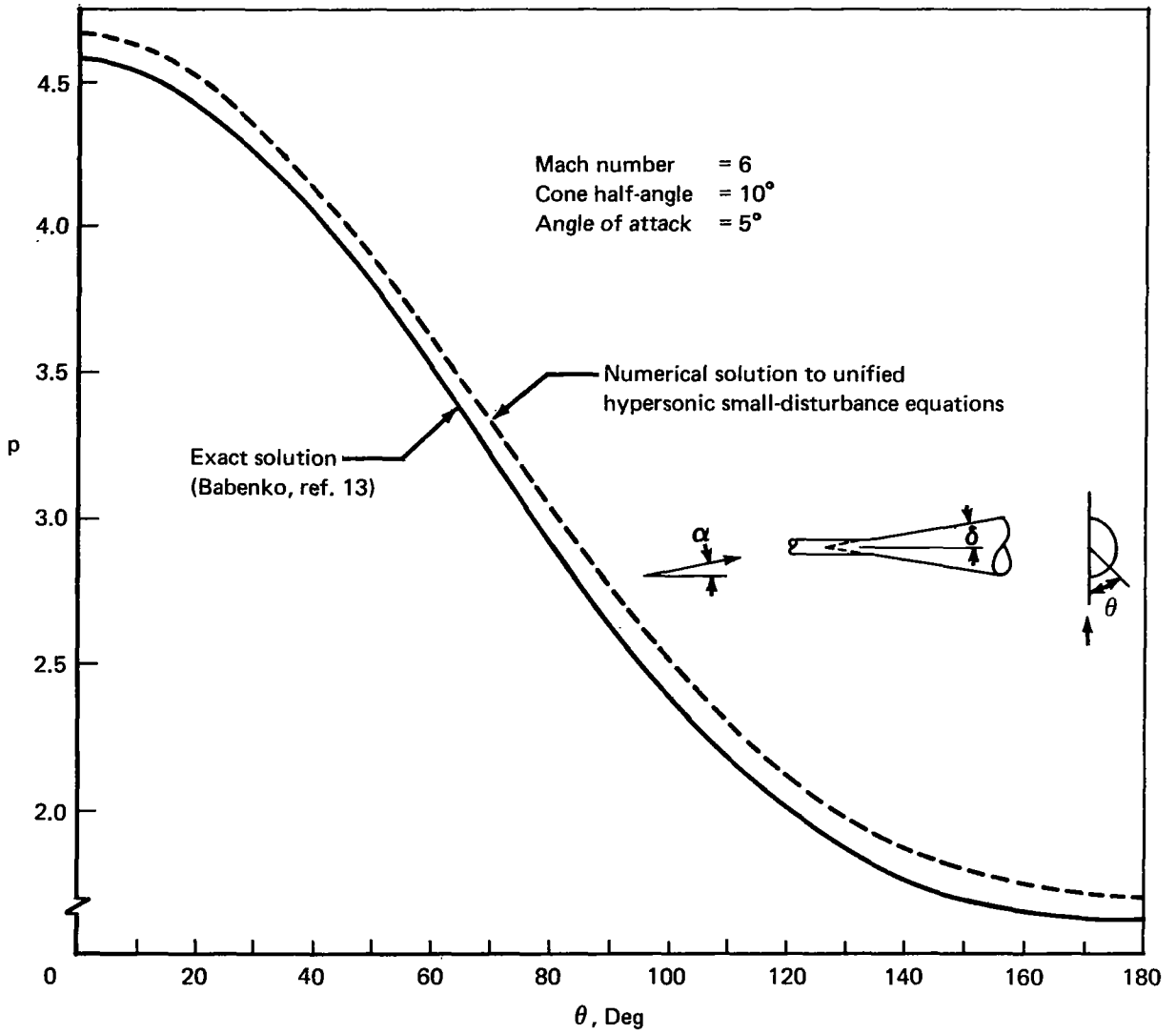


FIGURE 10.—COMPARISON OF THE STEADY-STATE PRESSURE DISTRIBUTION AFTER AN IMPULSIVE START WITH THE EXACT PRESSURE DISTRIBUTION

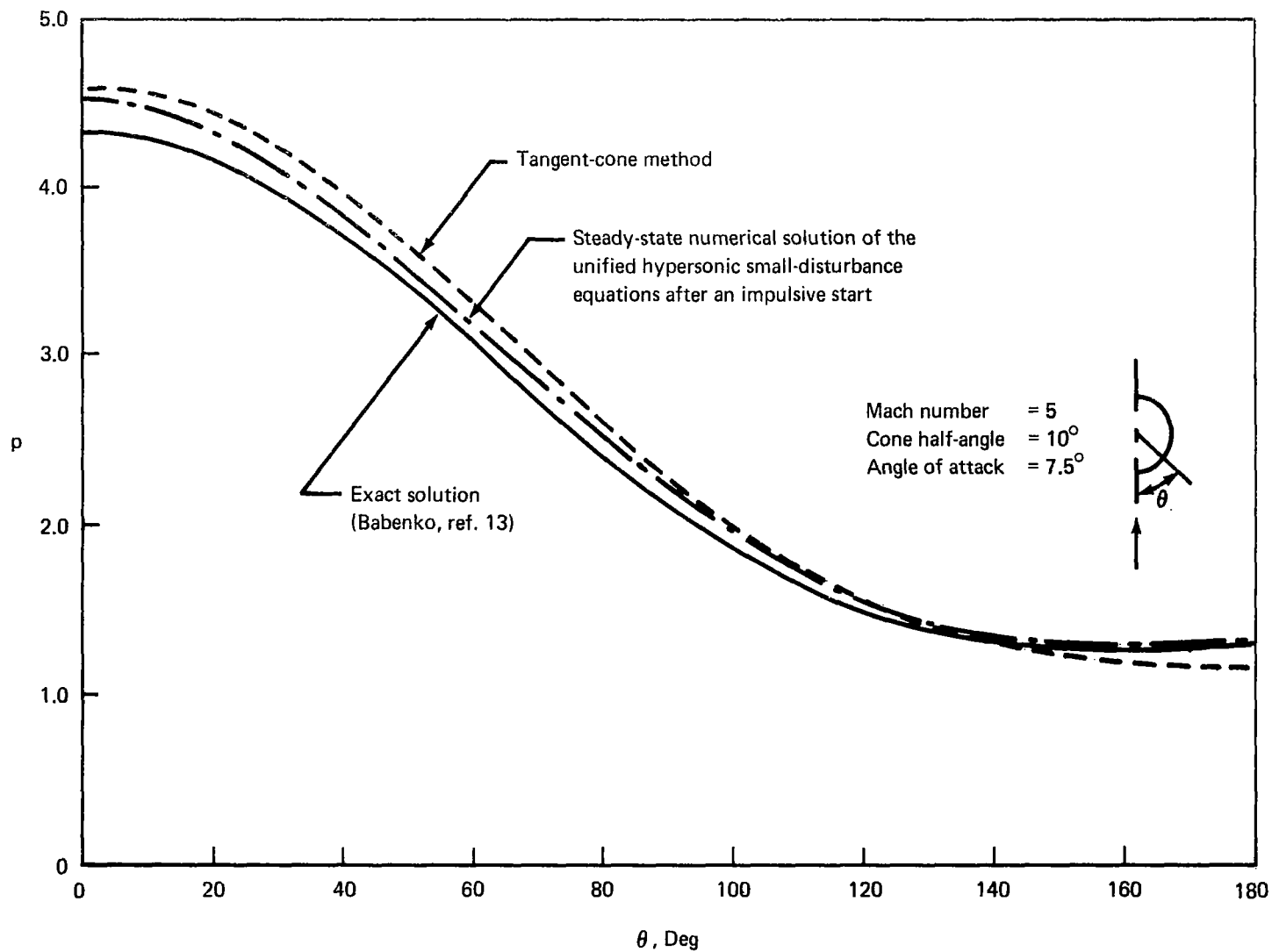


FIGURE 11.—COMPARISON OF PRESSURE DISTRIBUTIONS FOR A CONE AT ANGLE OF ATTACK OBTAINED USING DIFFERENT METHODS

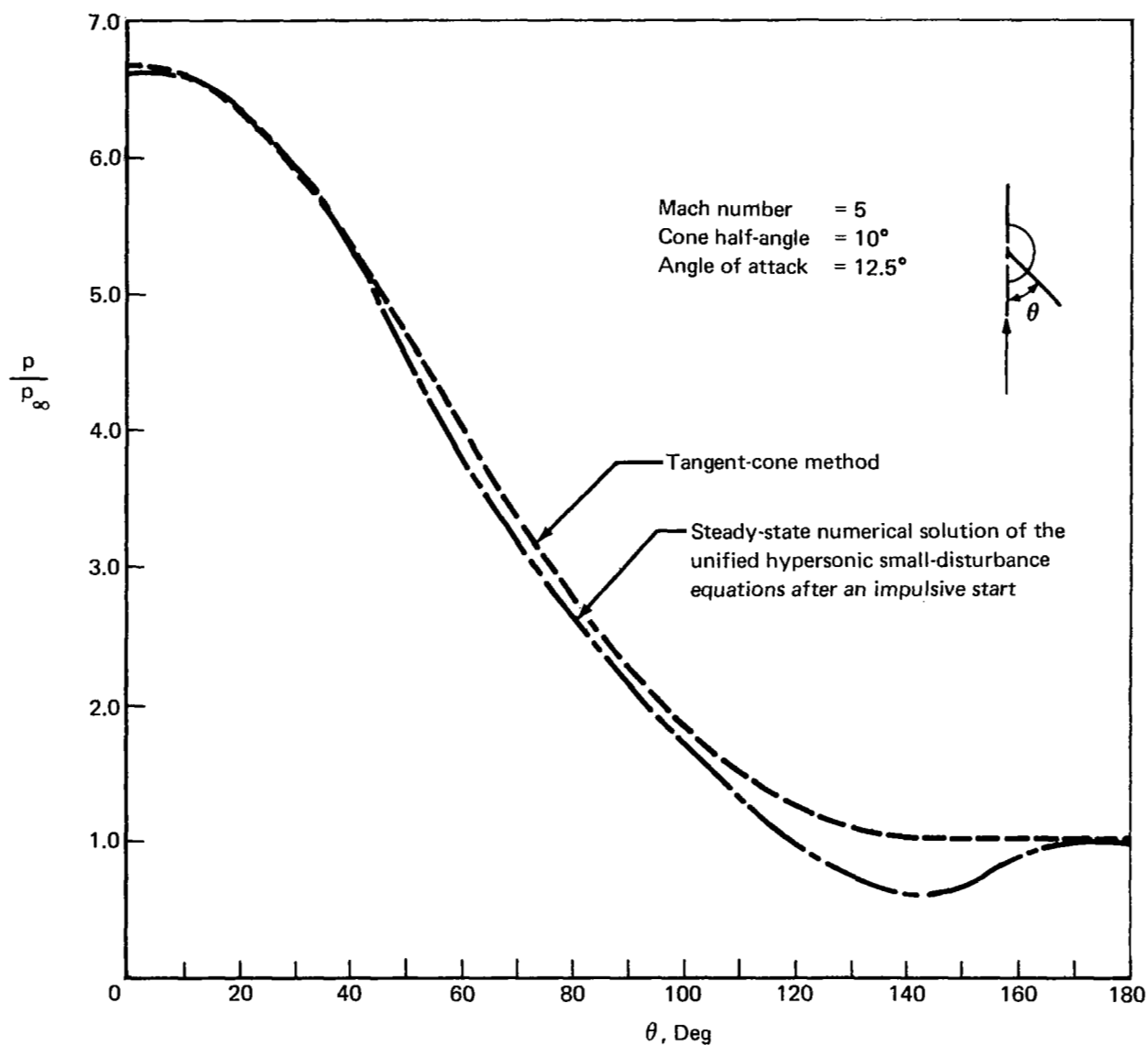


FIGURE 12.—COMPARISON OF PRESSURE DISTRIBUTIONS FOR A CONE AT
 ANGLE OF ATTACK OBTAINED USING DIFFERENT METHODS

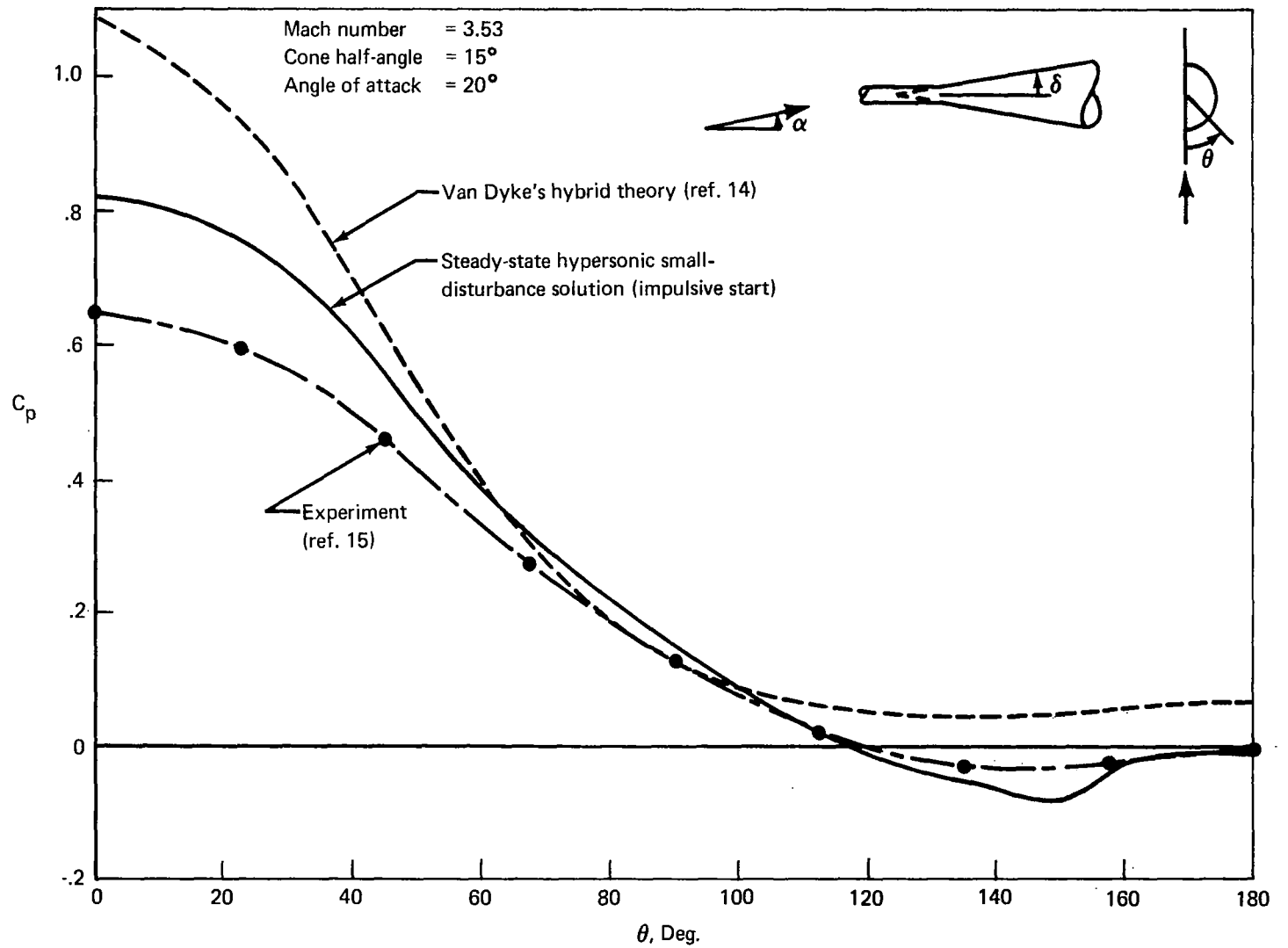


FIGURE 13.—SUPERSONIC FLOW OVER CONE AT ANGLE OF ATTACK

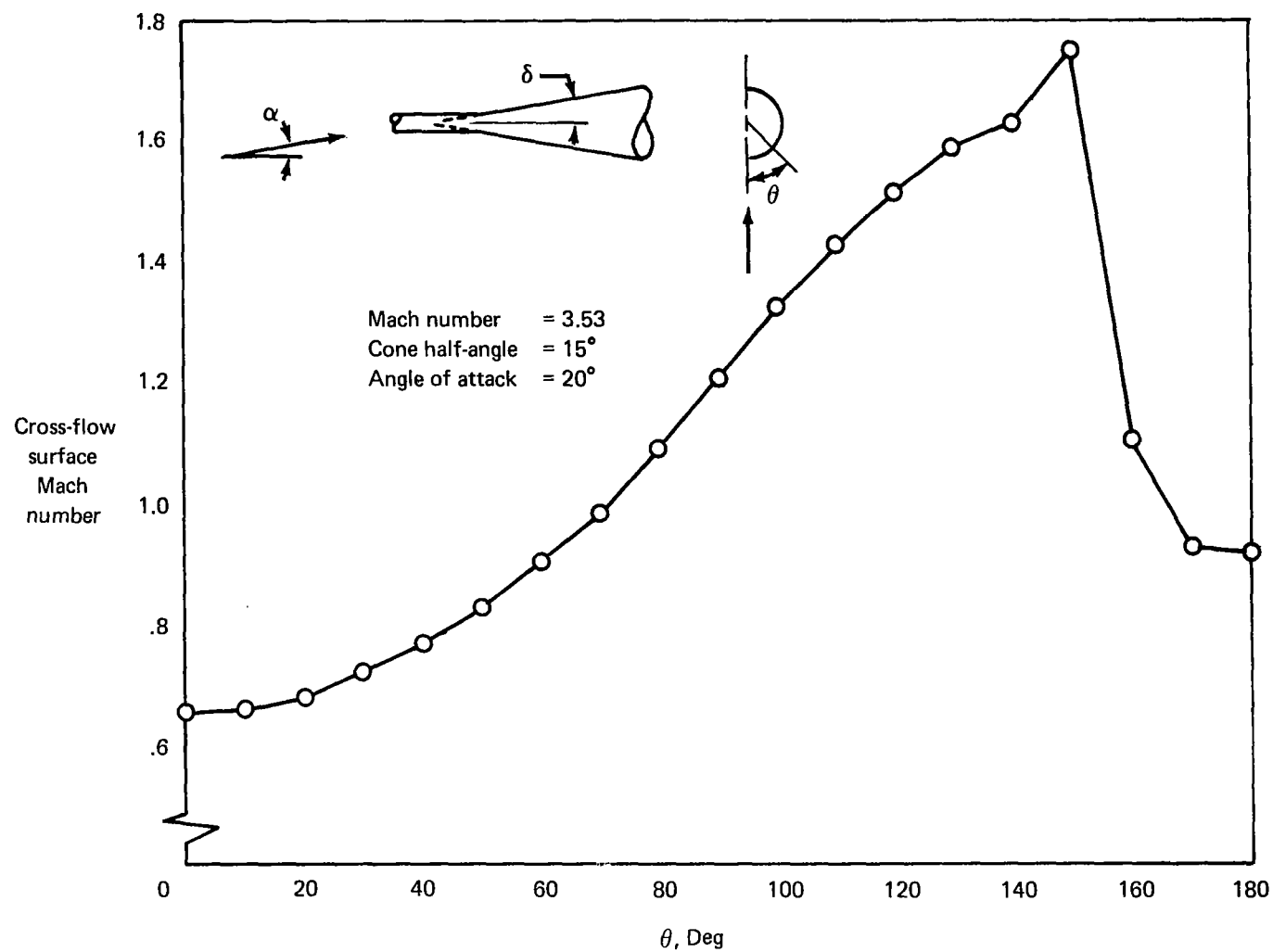


FIGURE 14.—SURFACE MACH NUMBER

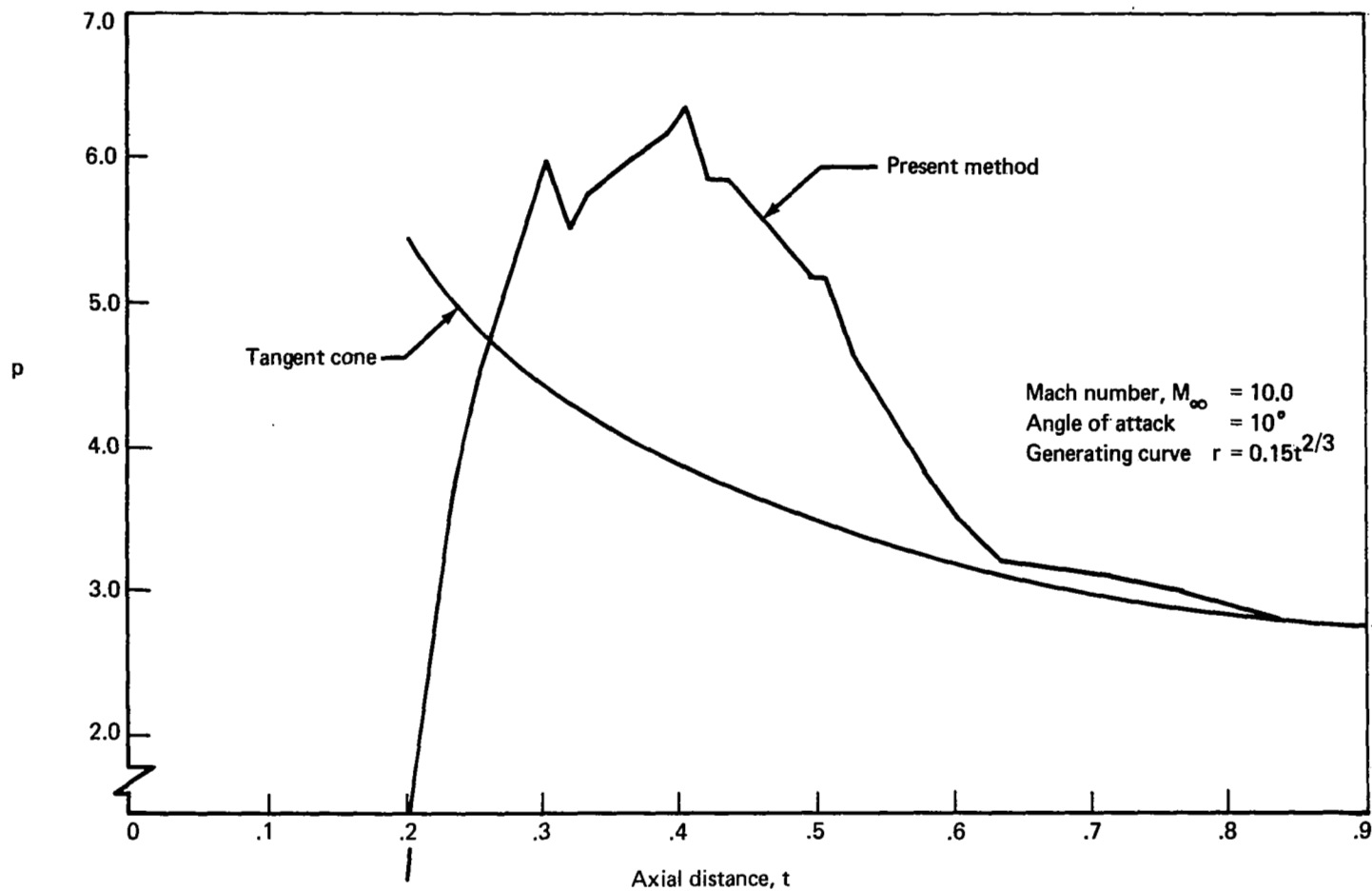


FIGURE 15.—DEVELOPMENT OF THE PRESSURE DISTRIBUTION ON A
 POWER LAW BODY AFTER AN IMPULSIVE START

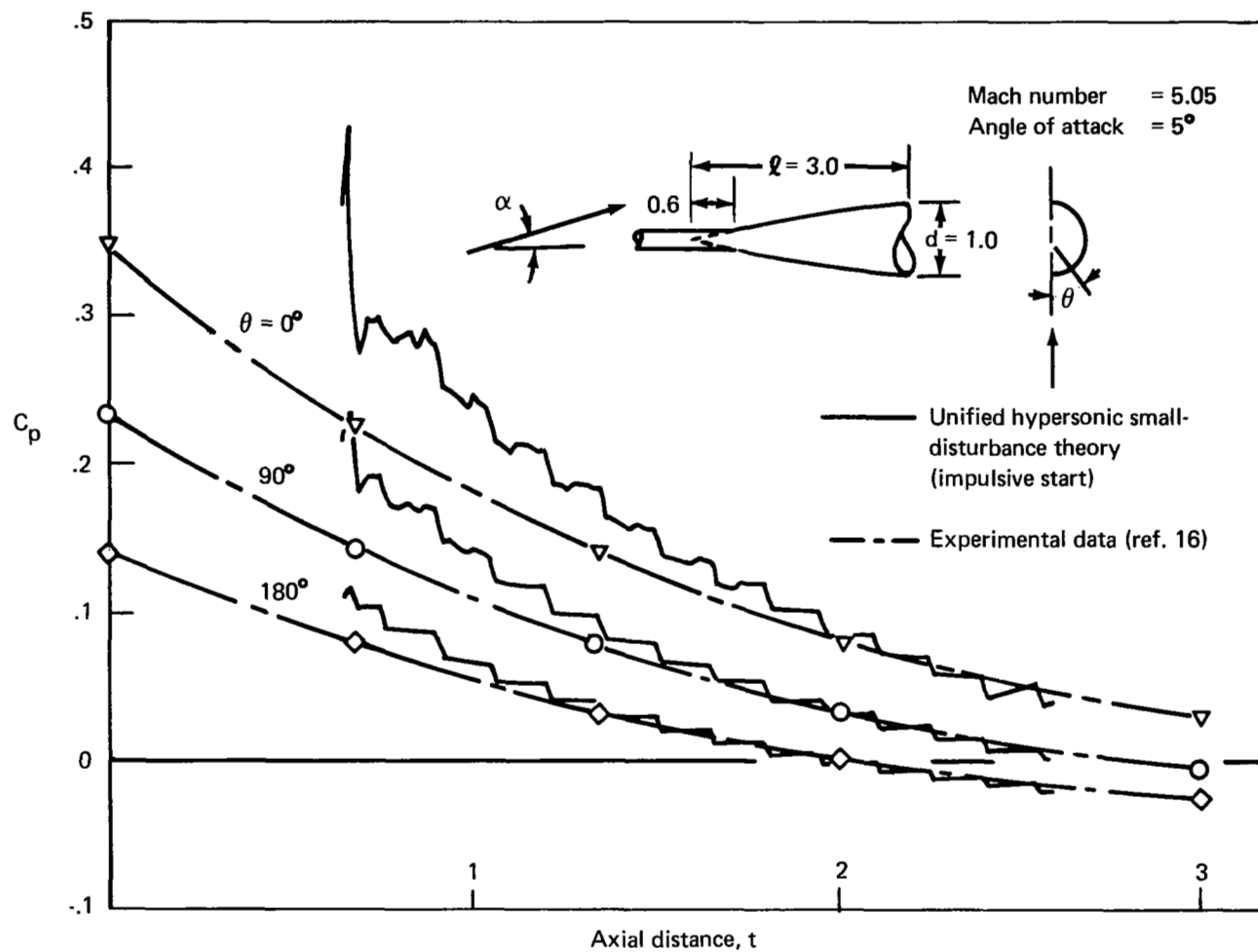


FIGURE 16.—PRESSURE COEFFICIENT ON AN $\ell/d = 3$ CIRCULAR-ARC OGIVE

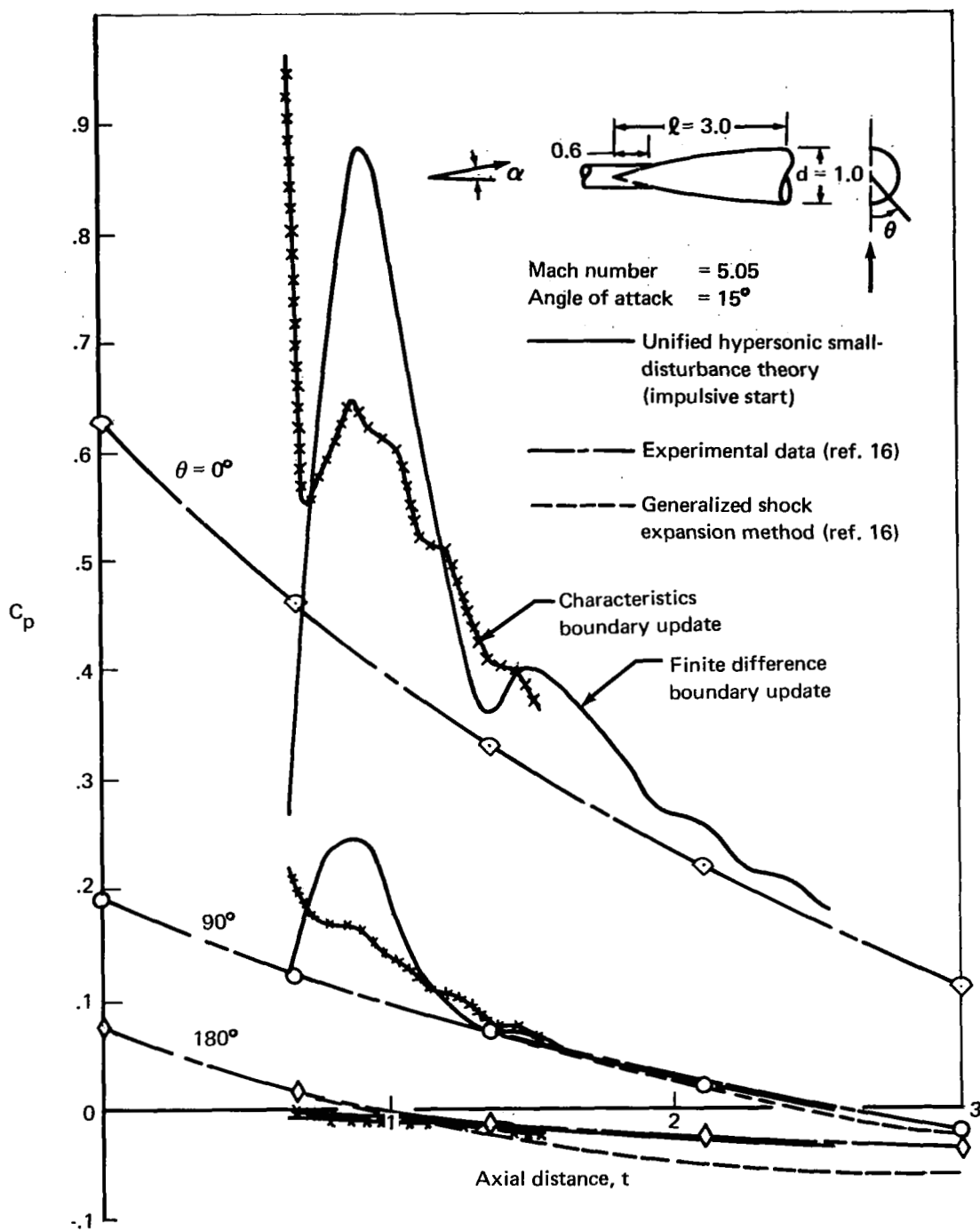


FIGURE 17.—PRESSURE COEFFICIENT ON AN $l/d = 3$ CIRCULAR-ARC OGIVE

Figure 18 shows the results for Mach 5.0 flow over a cone/cylinder combination. These results compare favorably with an exact method of characteristics solution. The overshoot at the beginning of the run ($t \approx 0.2$) is again attributed to the impulsive-start condition. Aft of the cone/cylinder juncture, two boundary update schemes were tested. For this particular case, the characteristics update BND3 is seen to be superior to the finite difference update BND1.

Figure 19 shows the results for axisymmetric supersonic flow over a circular-arc body. In this figure, a method of characteristics solution is shown as well as the results of the present method using the impulsive-start technique. Also shown are the results of the present method using tangent-cone starting conditions. These results clearly show the advantage of using good initial conditions.

Wiggles or steps in the impulsive-start curve are due to approximating the body by local straight-line segments in the streamwise direction. These wiggles do not appear using the latter version of the computer program (with which the tangent-cone start case was run) since higher order streamwise interpolation is now standard.

Elliptic Cones and Elliptic Cone/Wedge

A series of elliptic cones of cross sectional fineness ratio 2 were analyzed. These results are shown in figures 20 through 23. Also, the results for an elliptic cone/wedge are presented in figure 24. Figure 20 shows the results for Mach 5.8 flow over a 6° elliptic cone at zero angle of attack. Figures 21 and 22 show results for angles of attack 4° and 6° . Included for comparison in these figures are the experimental results as well as results from other analytical techniques. Agreement is seen to be generally satisfactory in all cases. The elliptic cone results in figure 23 are for the condition Mach 7.0, cone half-angle of 7.631° , and 1° angle of attack. Both boundary update schemes were tested. This case is significant in that it provides the forebody flow for the elliptic cone/wedge combinations of figure 24.

The elliptic cone/wedge case was rather extensively studied by Rakich (ref. 1) due to its importance as a possible hypersonic transport (ref. 17). Shown in figure 24 are the results for two corner geometries:

- 1) Sharp corner between the cone and wedge sections
- 2) Rounded corner between the cone and wedge sections of axial extent 0.01

Results obtained by Rakich (with a rounded corner) using a three-dimensional method of characteristics are shown for comparison. Immediately behind the corner, the agreement is not good, but downstream the curves are converging. We question the pressure rebound found by Rakich. As a matter of interest, the pressure behind a Prandtl-Meyer expansion fan and its small-disturbance counterpart are also shown.

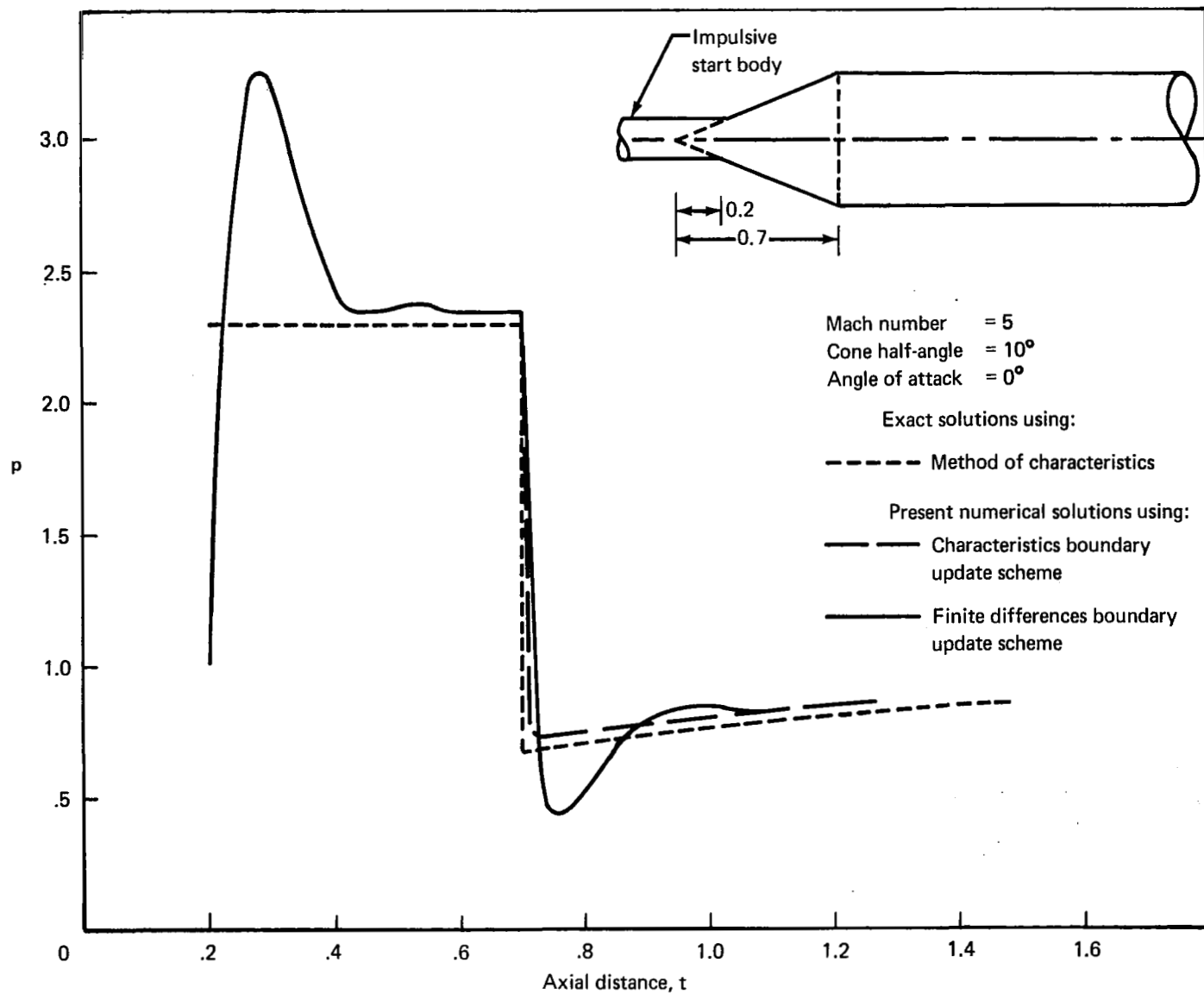


FIGURE 18.—HYPERSONIC FLOW OVER A CONE-CYLINDER

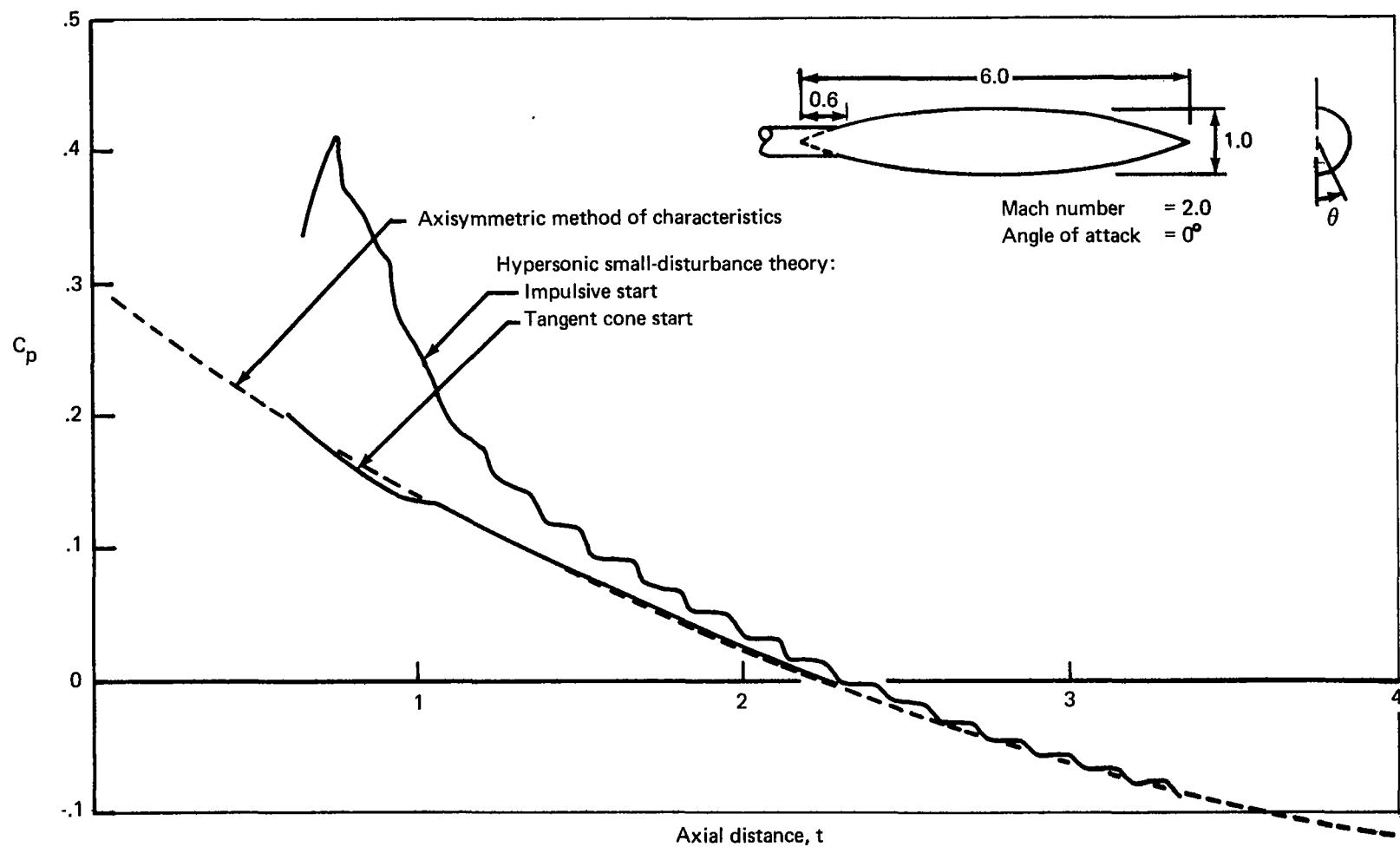


FIGURE 19.—SUPERSONIC FLOW OVER CIRCULAR-ARC BODY

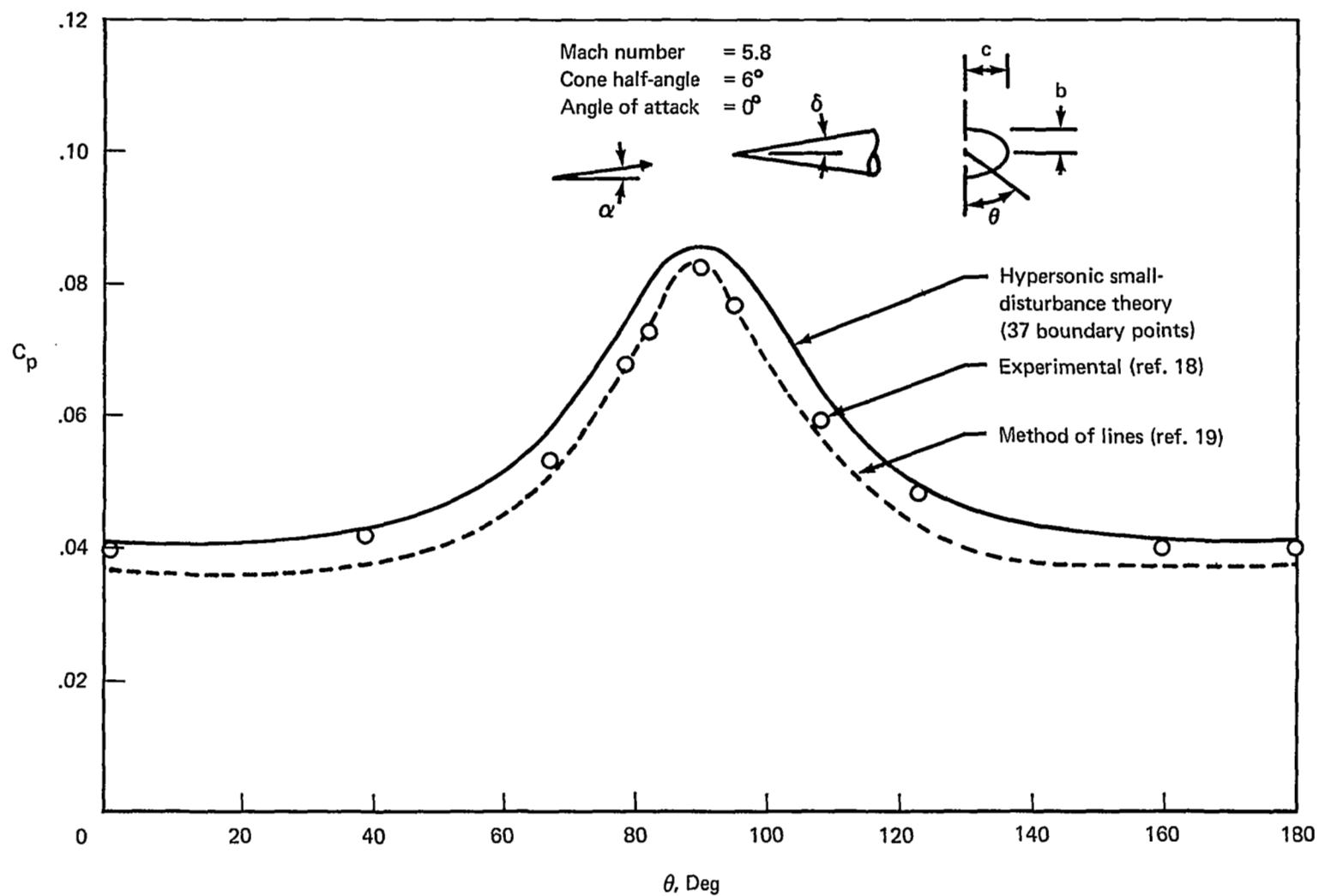


FIGURE 20.—PRESSURE DISTRIBUTION ON AN ELLIPTIC CONE, $\alpha = 0^\circ$

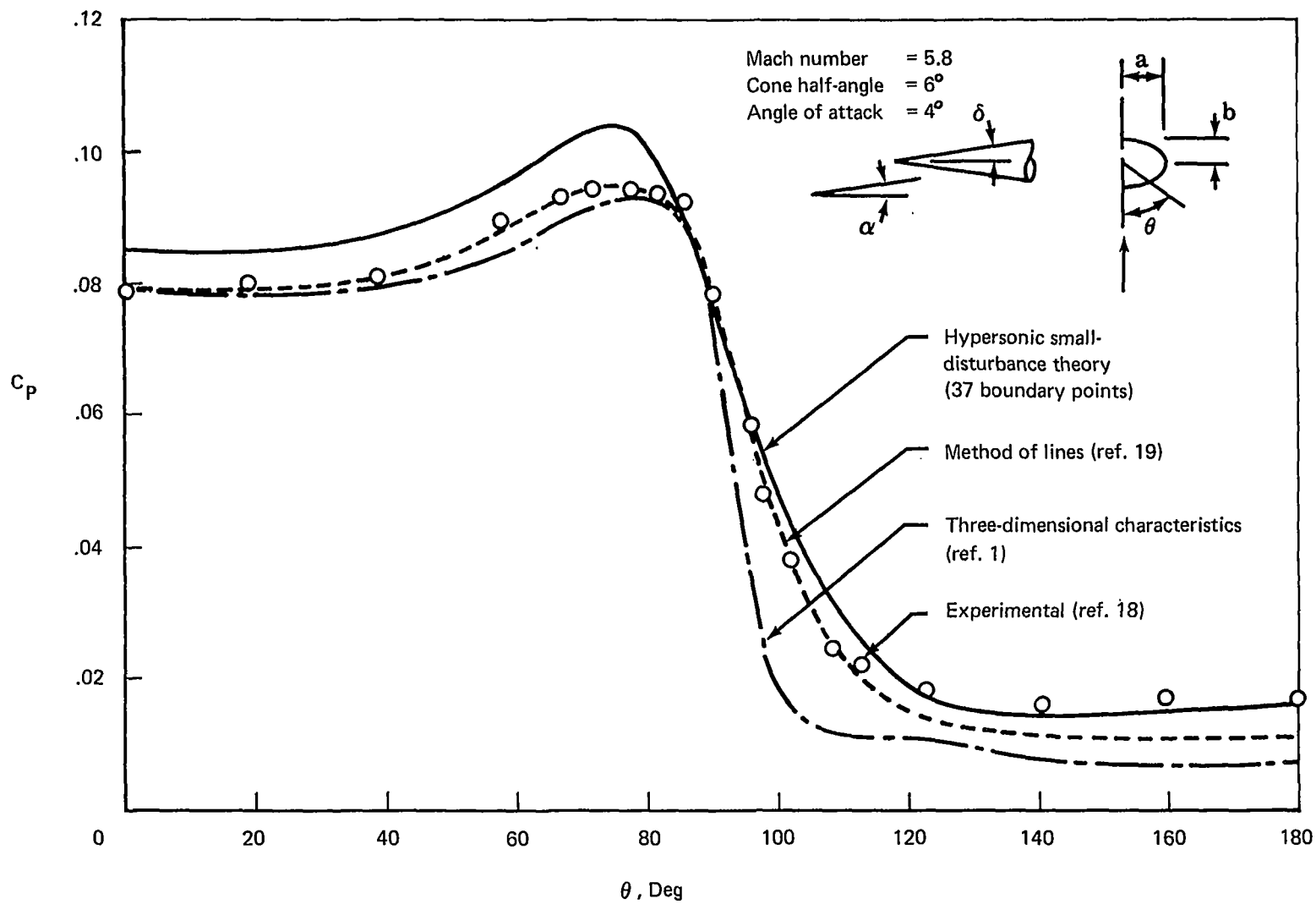


FIGURE 21.—PRESSURE DISTRIBUTION ON AN ELLIPTIC CONE, $\alpha = 4^\circ$

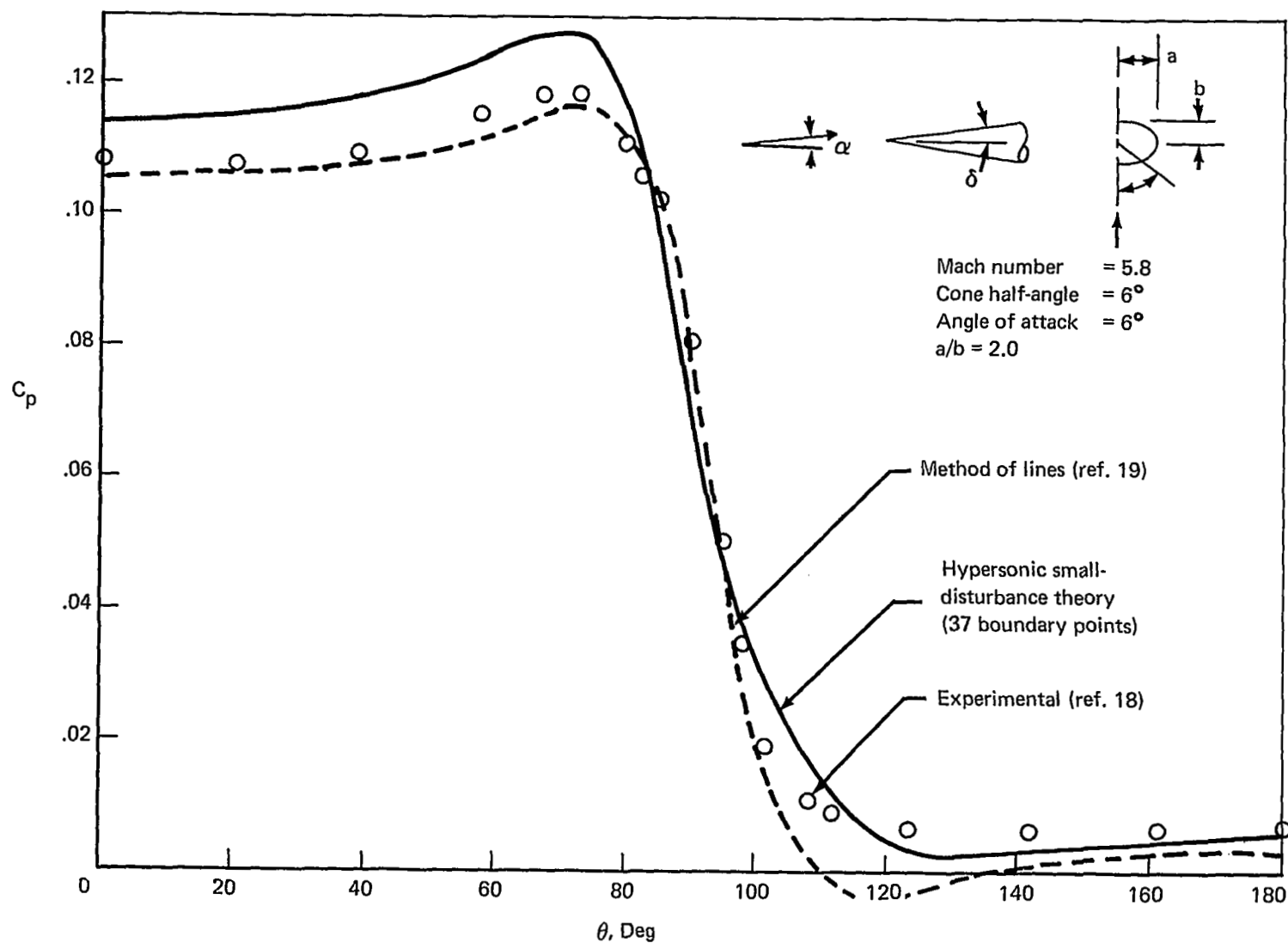


FIGURE 22.—PRESSURE DISTRIBUTION ON AN ELLIPTIC CONE, $\alpha = 6^\circ$

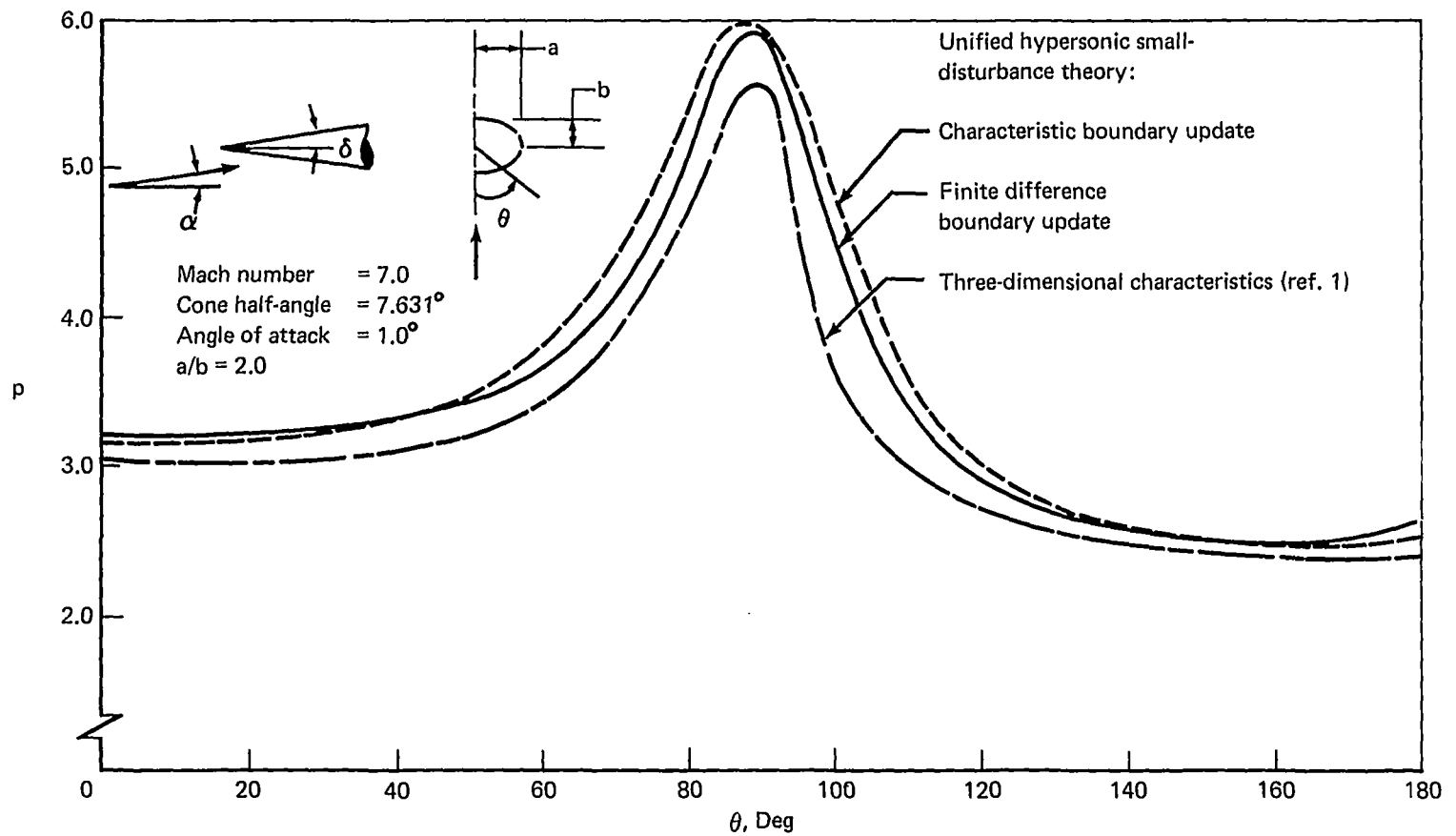


FIGURE 23.—PRESSURE DISTRIBUTION ON AN ELLIPTIC CONE, $\alpha = 1.0^\circ$

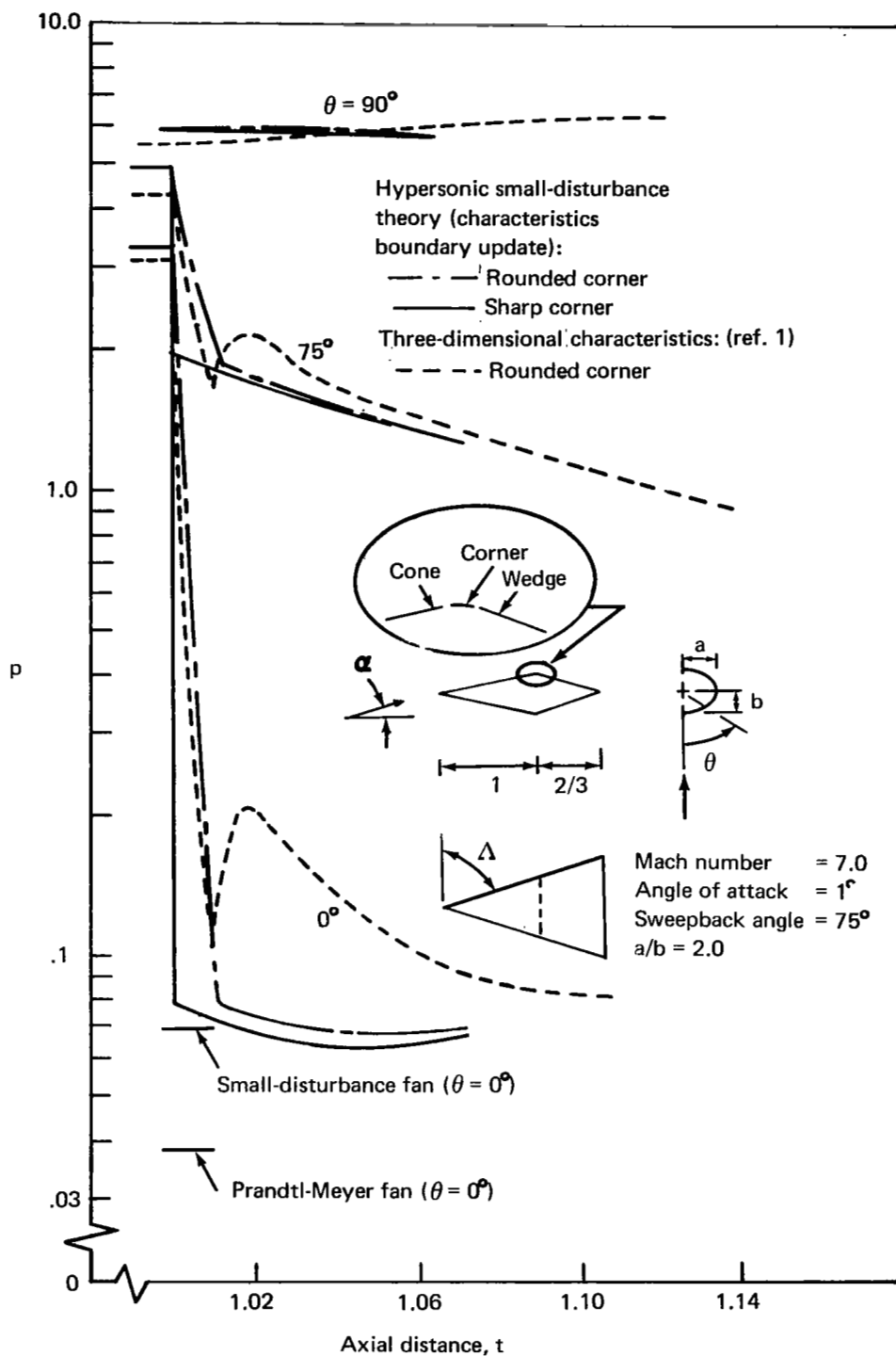


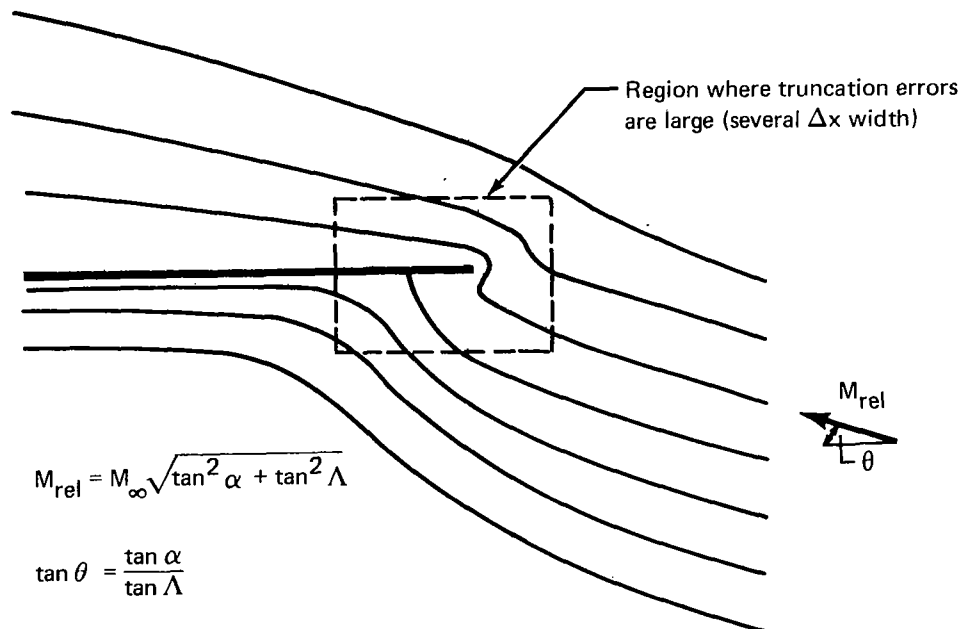
FIGURE 24.—SURFACE PRESSURE ON AN ELLIPTIC CONE/WEDGE

The previous cases dealt with smooth cross section geometries with flows that contained no singularities. It is both of theoretical as well as practical interest to examine how the method works for the more complicated singular-type flows. To this end, experiments were performed using the method on two flat delta wing geometries with a supersonic freestream flow of $\text{Mach}\sqrt{2}$ at 10° angle of attack. The first case had a sweepback angle of 67.5° (subsonic flow normal to leading edge), whereas the second case had supersonic leading edges with a sweepback angle of 30° . The results for these cases will be discussed separately.

Subsonic leading edge.—The results for the subsonic case are shown in figures 25 and 26. In figure 25, the surface pressure coefficient is shown plotted against the span for various time levels (or against axial locations in three dimensions). It is seen that, after 100 steps, the flow is stationary everywhere except near the leading edge. Also shown plotted are the corresponding results from linear theory. The oscillation near the leading edge will be discussed below. The lower surface experimental results of Rogers and Berr (ref. 20) for very flat elliptic cones at $\text{Mach}\sqrt{2}$, angle of attack 10.2° , and sweepback angle 60° are also shown plotted. The experimental data, which were discovered after the case was run, were corrected slightly to account for the small difference in sweepback angle (67.5° for theory vs 60° for experiment). This was accomplished by assuming that the difference between the linear theory and the experiment at 60° would be the same as at 67.5° .

The agreement is excellent. Rogers and Berry reported that the upper surface experimental results were dominated by viscous effects. Figure 25 compares the results from using the BND1 and BND3 update schemes. The two methods seem to give essentially the same results.

The nature of the leading edge flow is considered next in more detail. The sketch below is what the ideal inviscid flow should look like—relative to the leading edge for a flat delta wing (with subsonic leading edges).



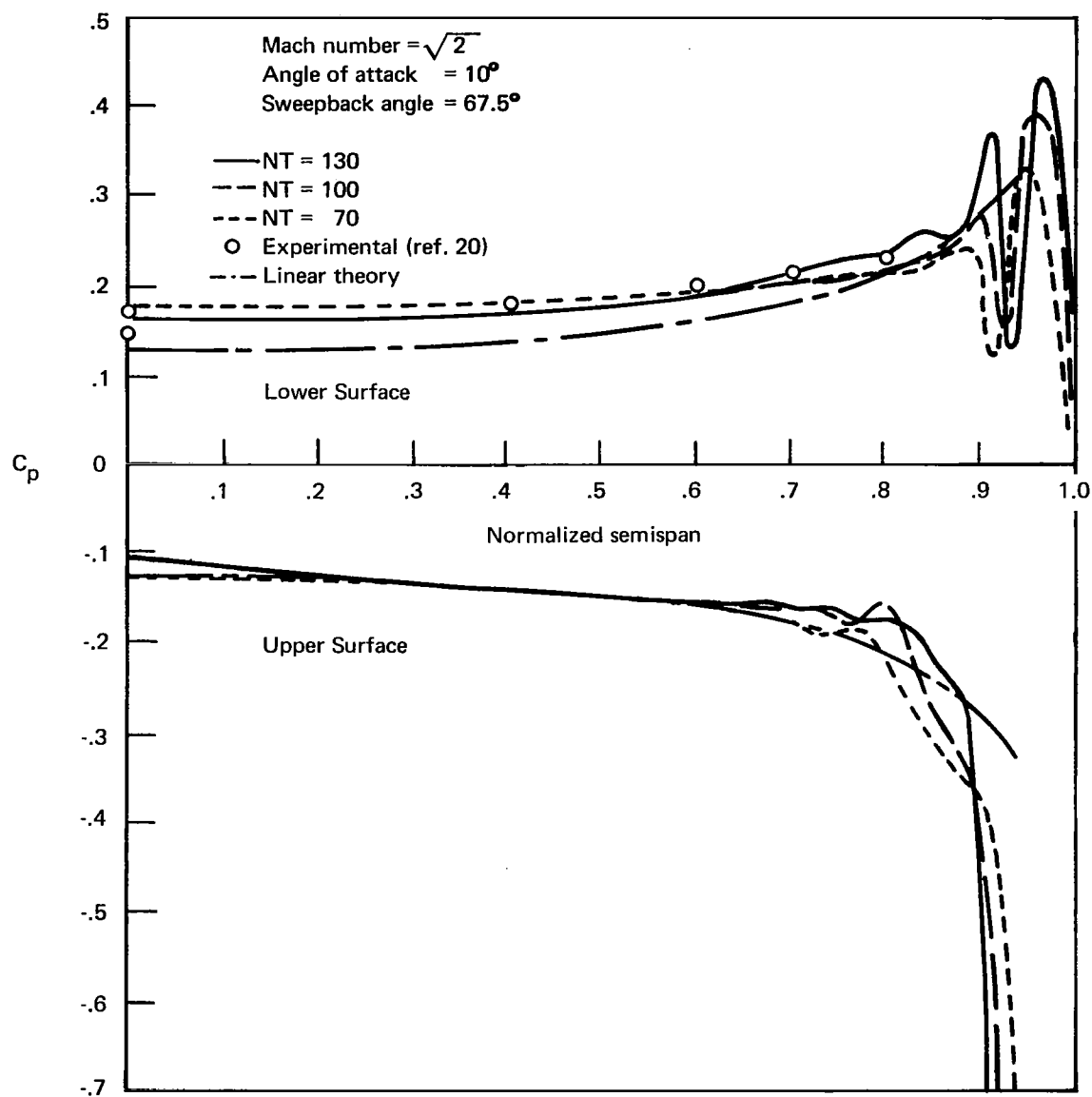


FIGURE 25.—PRESSURE DISTRIBUTION FOR SUPERSONIC DELTA WING WITH SUBSONIC LEADING EDGES

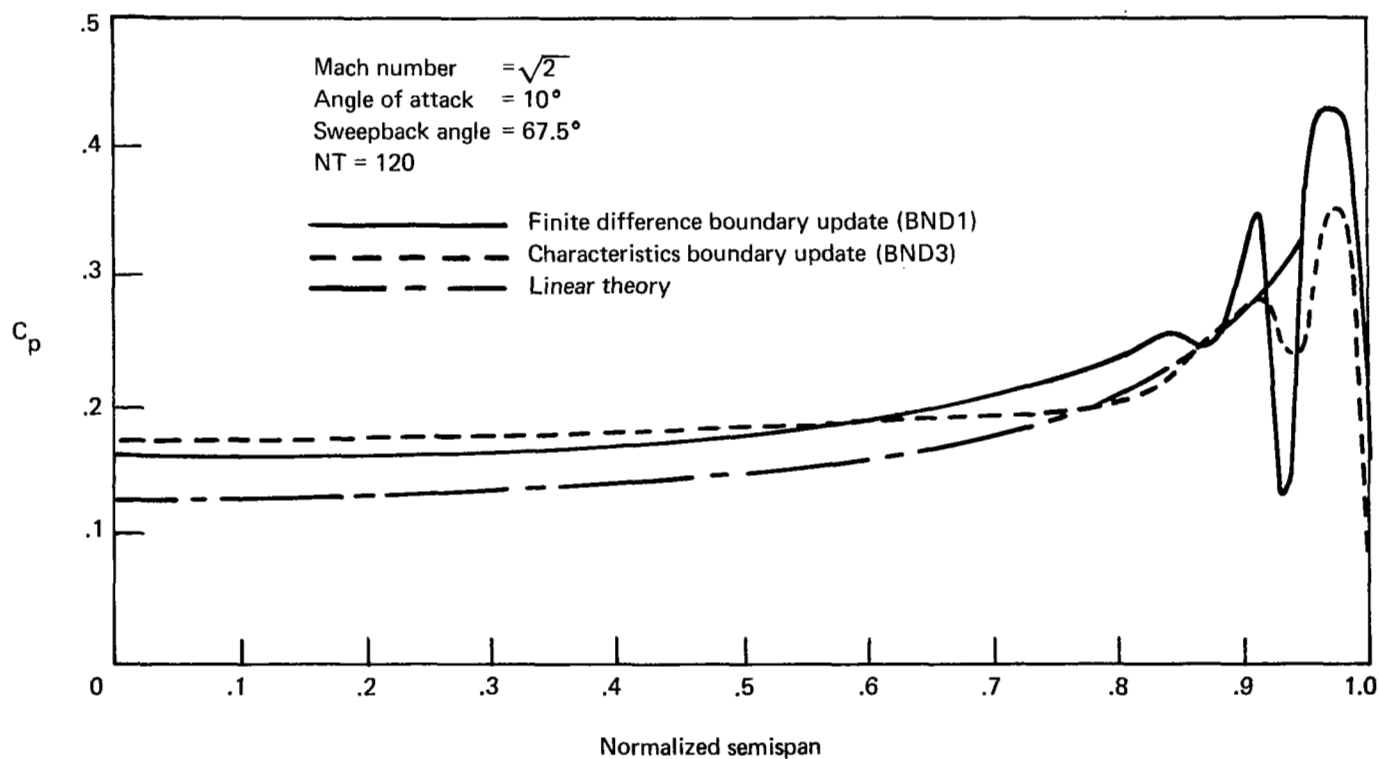


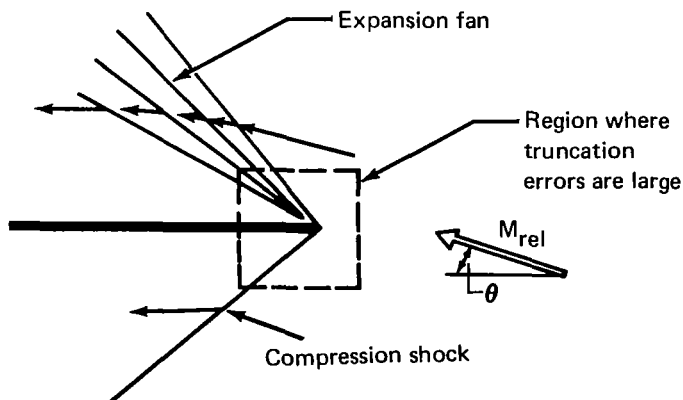
FIGURE 26.—COMPARISON OF SURFACE UPDATE SCHEME 3, BND1, AND BND3 FOR SUPERSONIC FLOW OVER DELTA WING

The flow at the leading edge is singular, so, within a distance of at least several mesh steps, the numerical method will have a significant truncation error. Unfortunately, this error does not remain localized because any fluid particles that pass through this numerical “viscous like” region (shown by the dashed box) become adversely influenced and pick up vorticity. For the present case, the relative stagnation streamline was very close to the leading edge, so the fluid particles in (and near) the upper and lower wing surfaces have properties that are in error. Figures 27 and 28 show the results of this influence on tangential momentum and density distributions. Figure 27 is reminiscent of the boundary layer type of behavior for the flow near the surface. The particles have picked up vorticity from the viscous-like numerical error created in the boxed-in region at the leading edge. Fortunately, as seen in figure 28, the density distribution (and hence pressures) is less affected. Note that the gradients are less severe as the fluid particles move away from the leading edge. This decay is attributed to the numerical “viscosity.”

A number of numerical experiments were attempted to try and minimize this boundary layer effect. Rounding the edge without refining the mesh made the situation worse because the region of the error was extended. To remedy this solution by rounding would require a very fine local mesh. Since the computer program is currently not capable of a local mesh refinement, it was decided to at least localize the extent of the error region by using a sharp leading edge. In the future, it would be best to treat this local region analytically and match it to the numerical solution some distance away from the edge. Such experiments are described later, for the hypersonic flow case, in “Delta Wings—Hypersonic Flow.”

Supersonic leading edge.—The results for the supersonic leading edge case (sweepback angle 30°), are shown in figure 29 for several time levels. The results were run with the BND1 update scheme. Except near the leading edge, it is evident the results for $NT = 85$ are essentially the converged conical value. For comparison, the results from linear theory are shown. Experimental results were not available for further comparison. The oscillations near the wing leading edge are again attributed to the singular behavior of the flow at the leading edge. Sketched below is the behavior expected for the flow relative to the supersonic leading edge.

The particles going over the top are affected by the singularity near the foot of the expansion wave. On the other hand, the particles going over the lower surface are strongly affected by the numerical representation of the shock wave. To remedy this situation, the numerical solution should be matched to the local exact solution several mesh points away from the leading edge. Boundary-layer-type behavior, such as observed in figures 27 and 28, was also observed for the supersonic leading edge case.



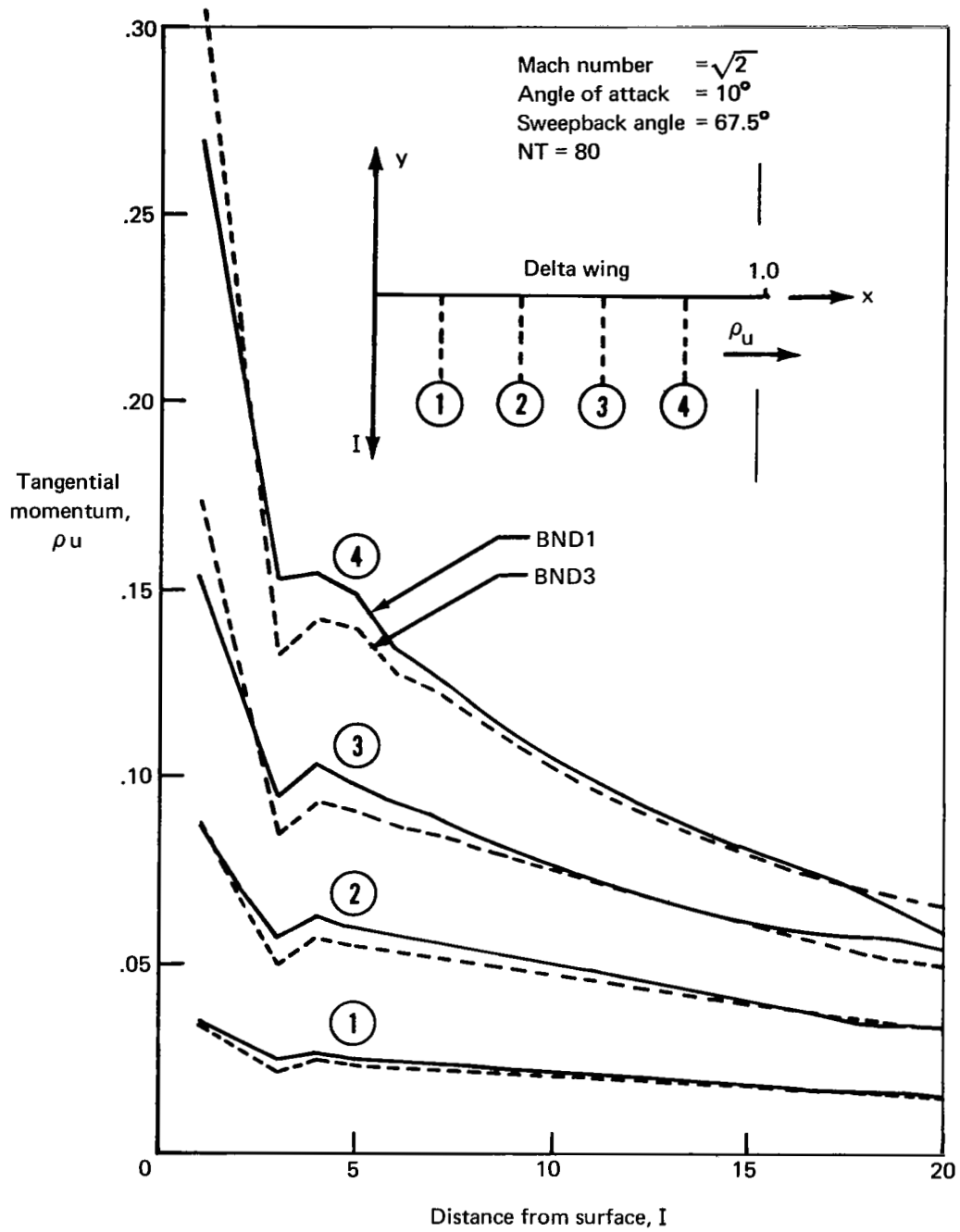


FIGURE 27.—TANGENTIAL MOMENTUM VARIATION

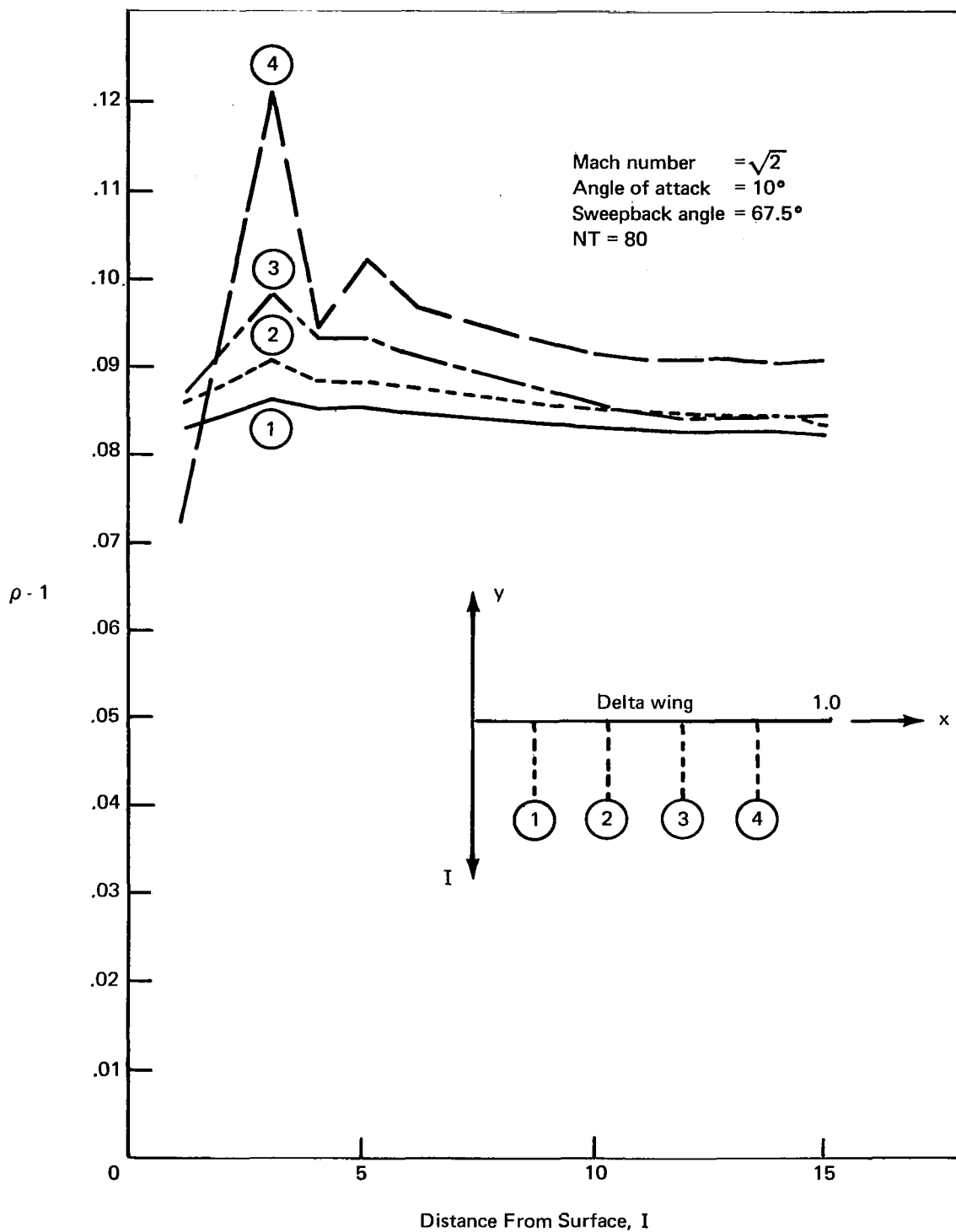


FIGURE 28.—DENSITY VARIATION

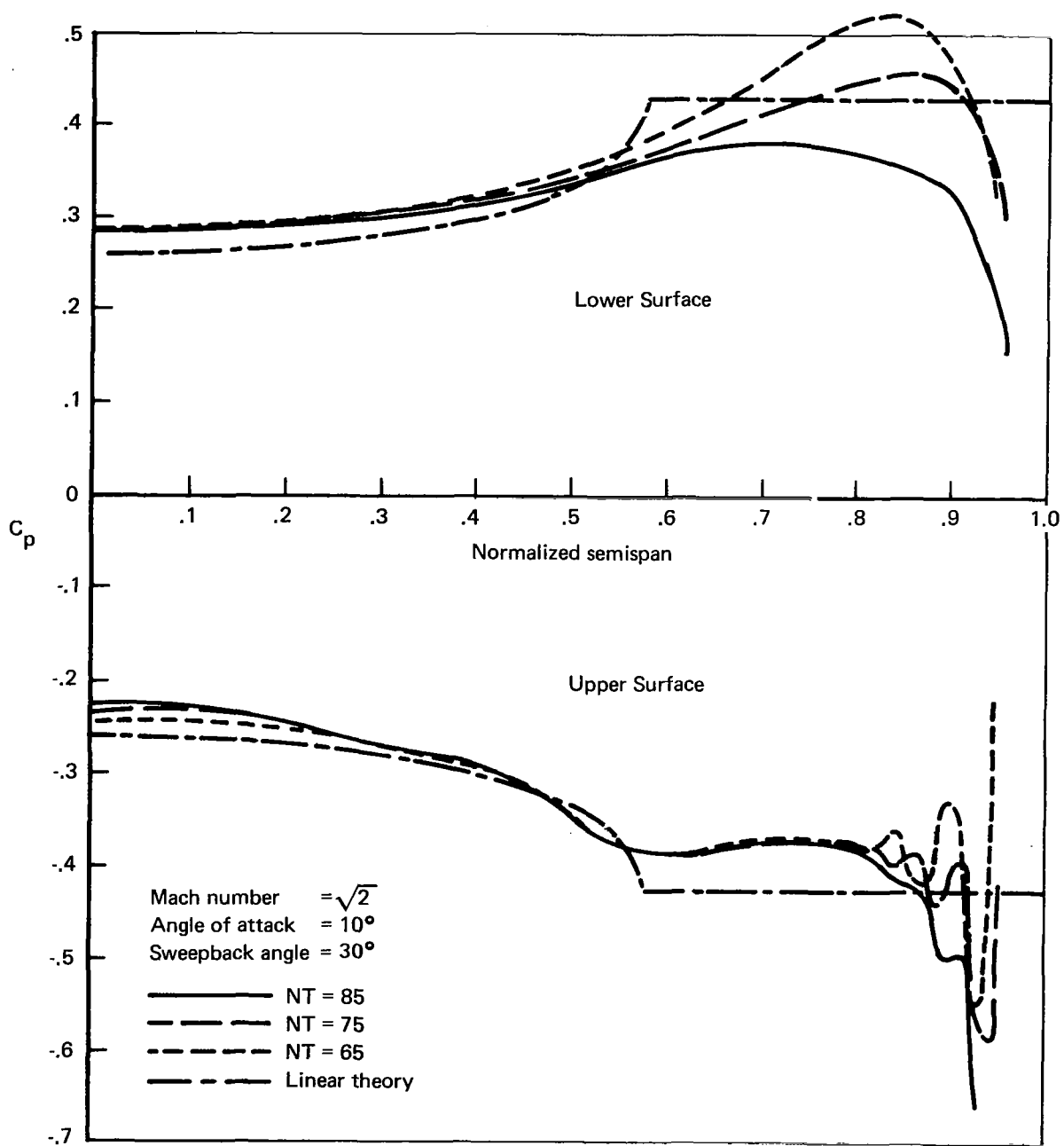


FIGURE 29.—PRESSURE DISTRIBUTION OF SUPERSONIC DELTA WING WITH SUPERSONIC LEADING EDGES

In figures 30 and 31, the results are shown for Mach 8.08 flow over a slab delta wing, with sweepback angle 73° at angle of attack 10° . The rounded leading edge was considered with the hope that the previously noted leading edge error could be eliminated. The shock shape is shown in figure 30. Note that the shock effectively wraps around the leading edge, so a large numerical error is picked up by the fluid particles that pass through this region. The pressure oscillations shown in figure 31 are due to this behavior. However, away from the leading edge, good agreement with the result of Kennett's method (ref. 21) is seen.

Figure 32 shows the results of several experiments performed on this case. The dash line shows the converged results from figure 31. The solid line is a result of rerunning this case using a flat-plate geometry with two additional significant modifications. The first modification was to use tangent wedge initial conditions instead of the impulsive start. The second modification fits a shock wave to the lower surface of the delta wing leading edge to eliminate the leading edge error. (The procedure was discussed earlier in "Input Data Preparation.") The extent over which the leading edge flow is analytically determined is also indicated in figure 31. The simple modifications provide a drastically improved result—freedom from the oscillations and other peculiarities noted earlier.

Figure 33 shows the results of the present method for Mach 4.0 flow over a flat delta wing with 50° sweepback at 10° angle of attack. Also shown are the results of several other theoretical solutions to this problem. For this case, the leading edge shock was also inserted but the impulsive-start technique was used to initiate the flow. The present method is seen to agree well with the other methods. The slight oscillation of the present method at about 20% semispan is attributed to the slowly decaying transients produced by the impulsive-start initial conditions.

Wing/Body Combination

In figures 34 and 35 are the results for a midwing cone/delta wing combination. Mach number 5.08, angle of attack 11° , cone half-angle 12.5° , and sweepback angle 65° were chosen so that comparison with Randall's (ref. 24) experimental data would be possible. Figure 34 shows the crosscut geometry and shock shape. The shock envelope appears to be composed of a blending of the wing shock (with inclination 46°) and the cone shock. The overlap appears to occur at about the midspan.

In figure 35, the pressure coefficient is plotted against the semispan for various time steps after the initial impulsive start. Also shown are the experimental results of Randall and the analytical results that Kutler obtained from a conical-flow solution to the exact inviscid equation. The agreement is reasonable except near the wing/cone junction and the wing leading edge. The oscillation at the leading edge is a result of not fitting in the leading edge shock. (This case was run before the leading edge shock option was available in the program.) The spike at the root juncture is caused by numerical error introduced by not properly treating the root boundary points. This is due to the small radius of curvature in this region resulting from an attempt to smooth the root slope discontinuity. Since the flow is nonsingular in this region, it would have been better to have updated the surface corner point by interpolation from its nearest neighbors. It is hoped that this case can be rerun in the future using tangent cone/wedge starting conditions, the shock fit analytically at the leading edge, and the wing/body intersection point properly updated.

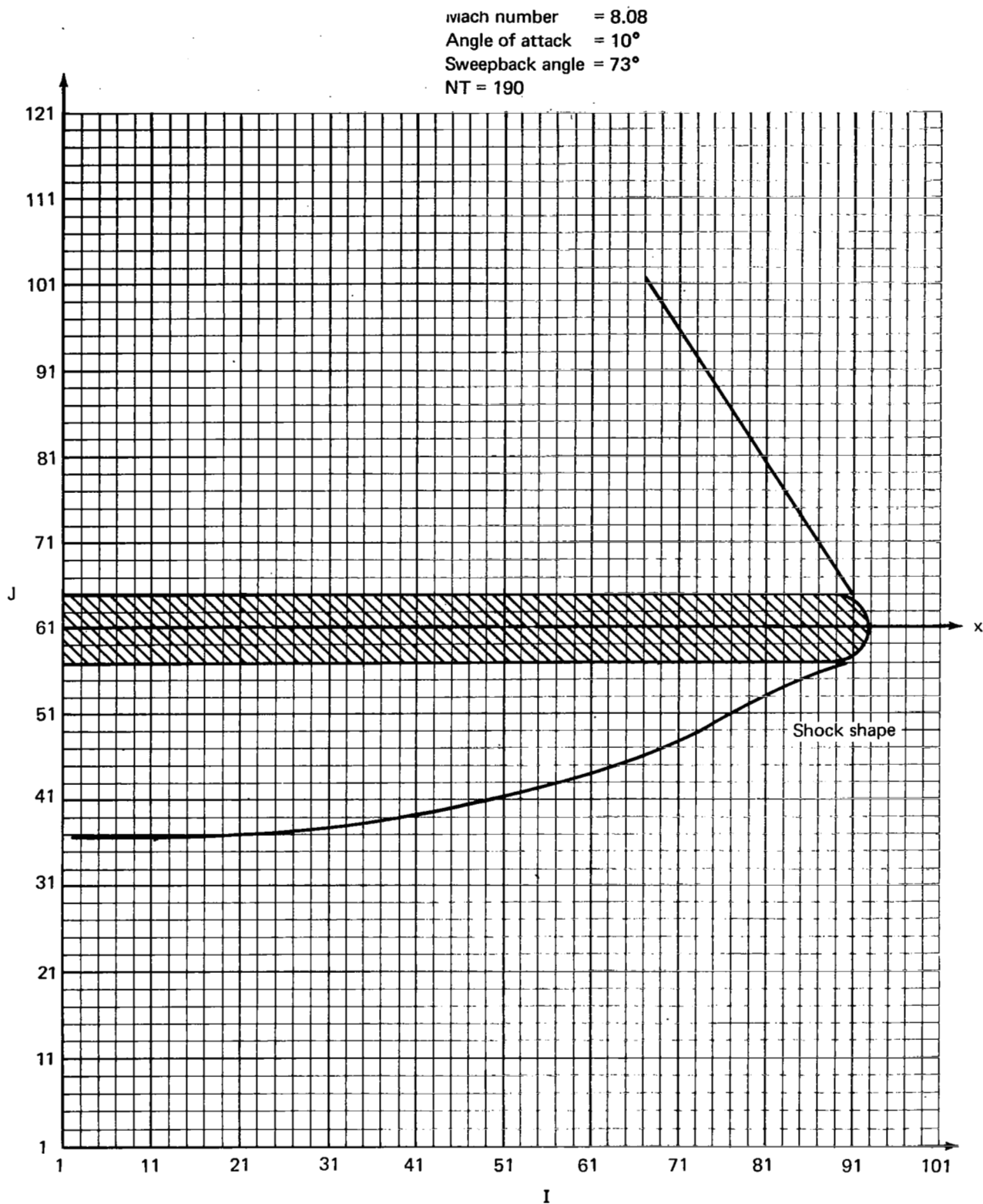


FIGURE 30.—SHOCK SHAPE FOR HYPERSONIC FLOW OVER SLAB DELTA WING

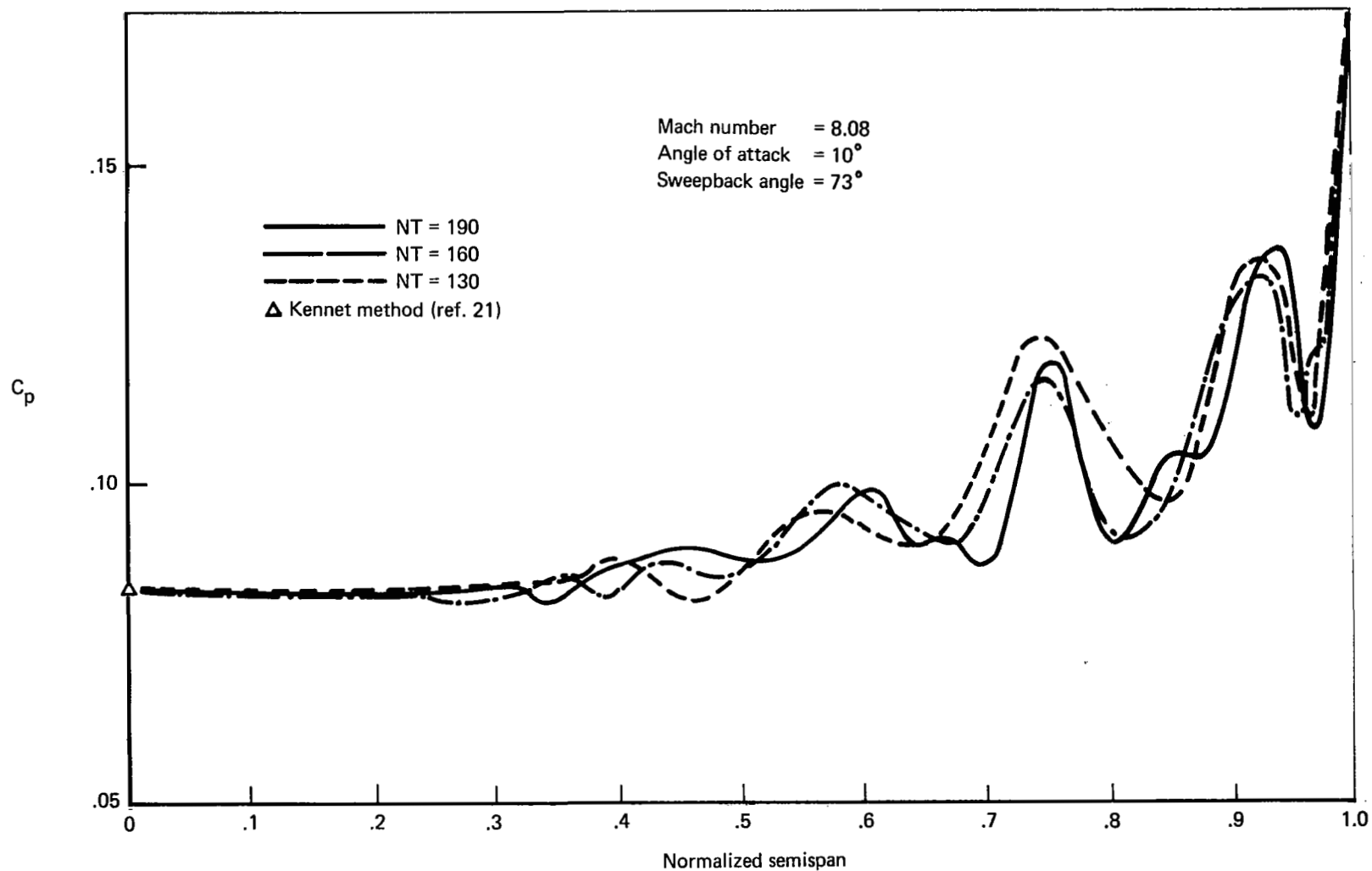


FIGURE 31.—PRESSURE DISTRIBUTION FOR LOWER SURFACE OF
 HYPERSONIC SLAB DELTA WING

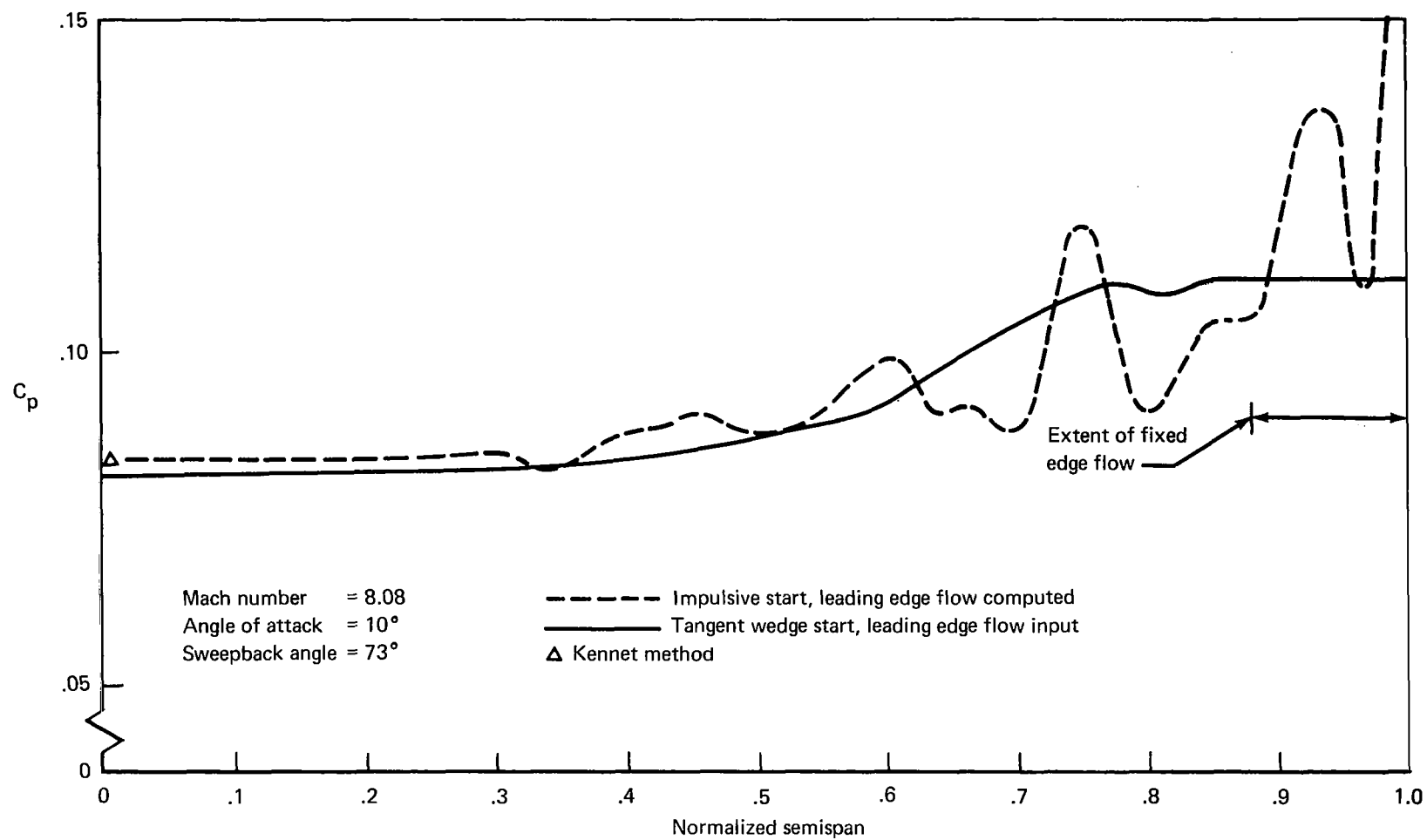


FIGURE 32.—DELTA WING PRESSURE DISTRIBUTION WITH LEADING EDGE AND INITIAL CONDITIONS MODIFIED

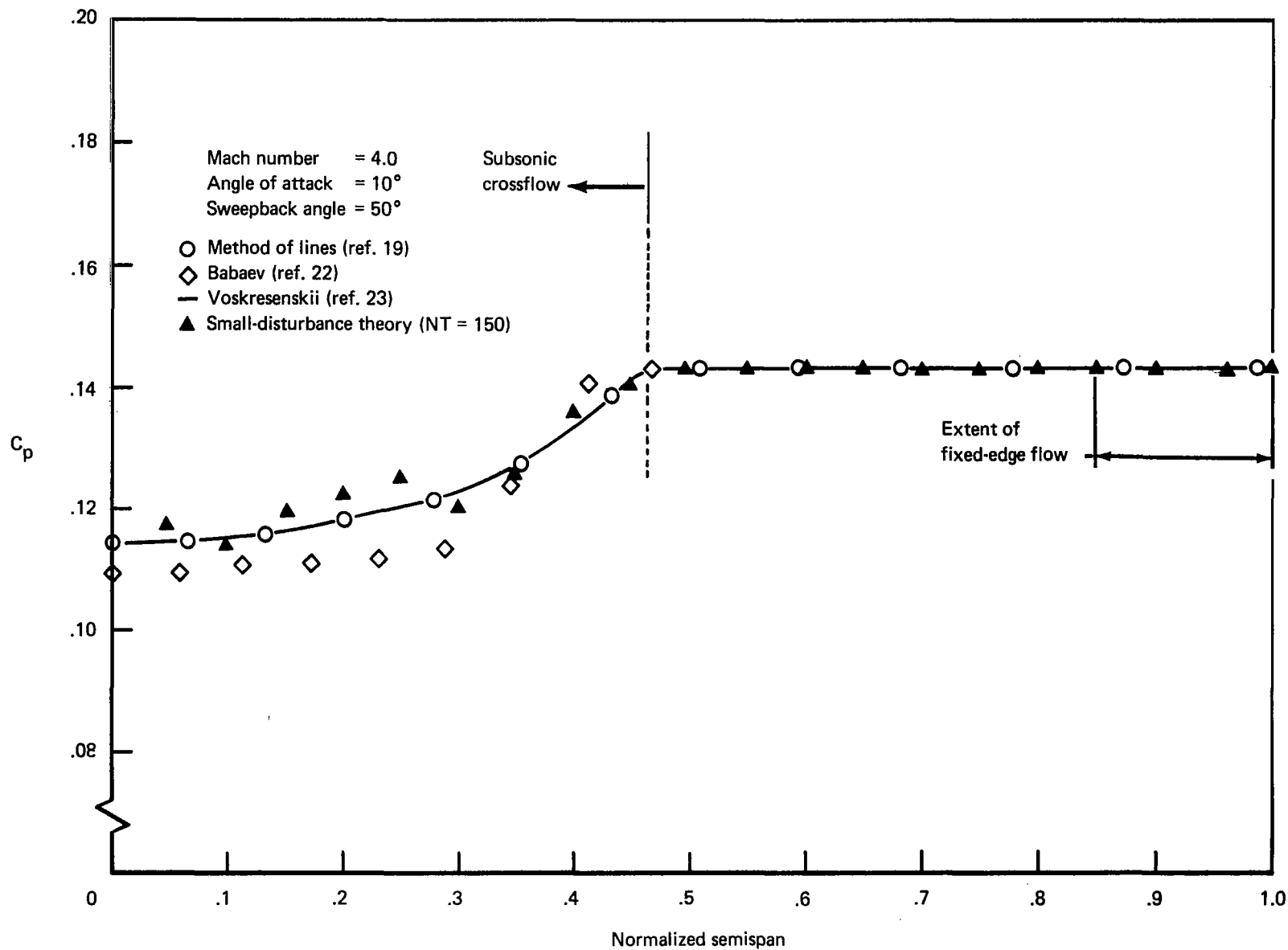


FIGURE 33.—PRESSURE DISTRIBUTION FOR FLAT DELTA WING

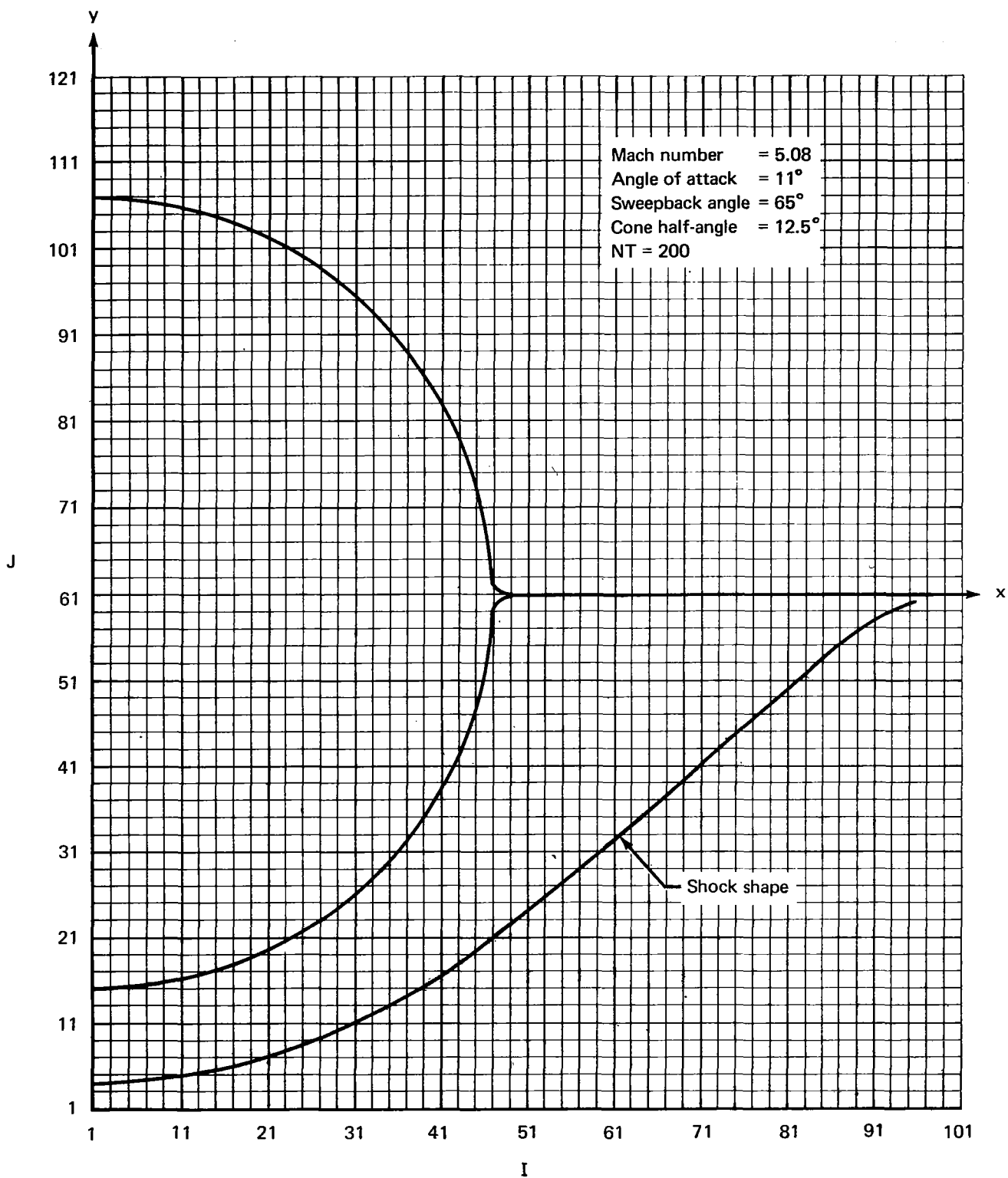


FIGURE 34.—SHOCK SHAPE FOR FLOW OVER WING/BODY COMBINATION

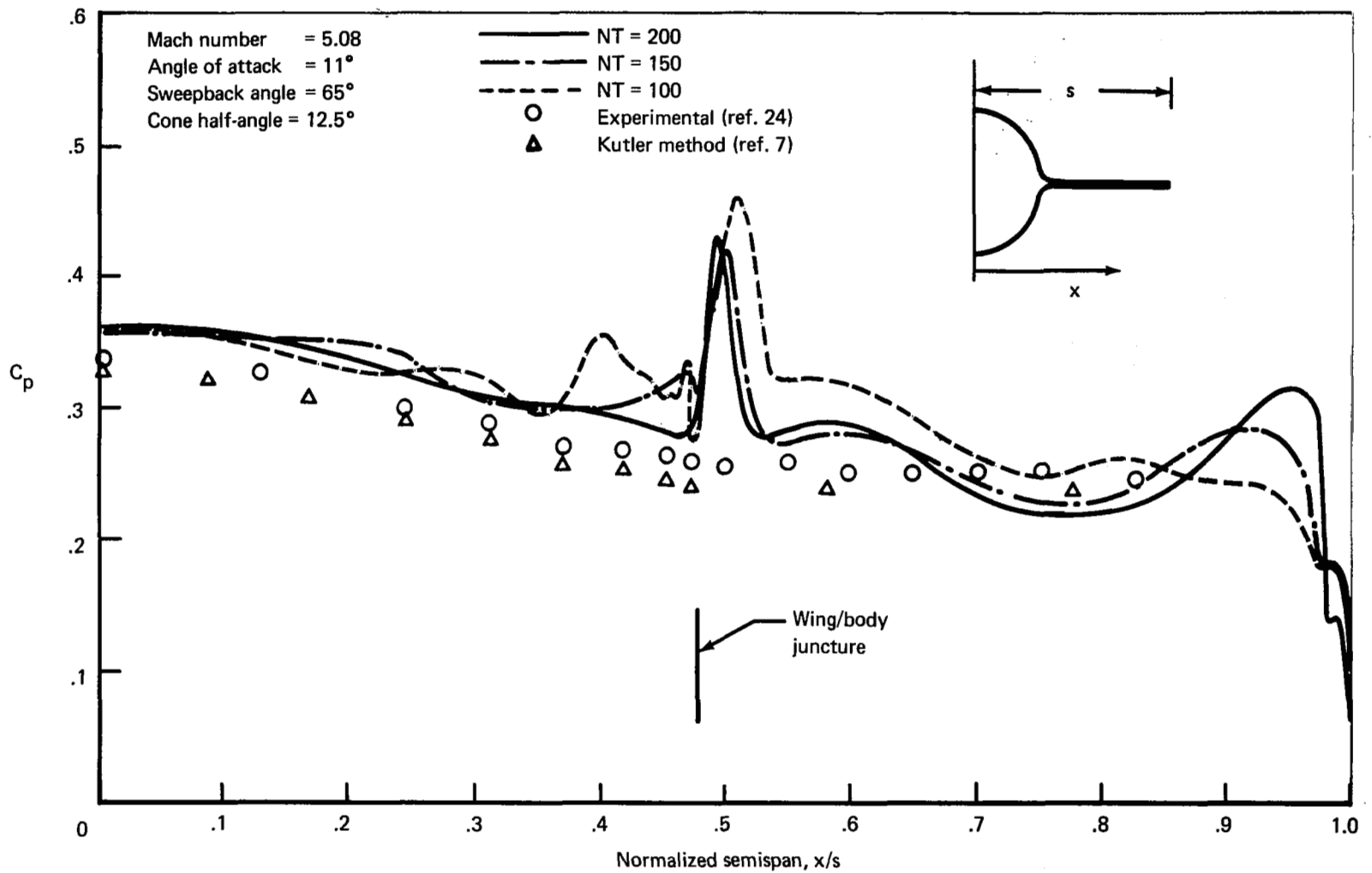


FIGURE 35.—PRESSURE DISTRIBUTION FOR FLOW OVER WING/BODY COMBINATION

CONCLUSIONS

All of the contract commitments have been met. From the experience gained during the development and operation of this program, certain conclusions and recommendations for further study can be made.

The most important conclusion is that the basic numerical techniques and concepts (described in "Analysis") have been demonstrated and validated. The basic numerical approach has proved to be sound. During the operation of the program, no unexpected difficulties occurred and the computer program is reliable to use and simple to operate. For a general (nonconical) flow method, this is a significant advance in the state of the art.

After examination of the cone results, axisymmetric bodies results, and the elliptic cone results, it is judged that the primary discrepancy between the exact solutions and the present numerical solution is due to the small-disturbance assumption. The delta wing series results and the wing/body combination results have, in addition, however, a purely numerical-type oscillation in the vicinity of the leading edges. Away from the leading edges, the results are satisfactory.

To remedy these features, it is felt that, in future work, the exact equations should be solved rather than the small-disturbance equations. In addition, the local flow singularities (such as occur at wing leading edges) that affect the fluid flowing over the aircraft surface should be given special consideration. This can be done either by using a local mesh refinement in the vicinity of the rapid surface flow changes or by using a local analytical solution and overlapping this on the numerical grid (some distance away from these special regions). During the present contract period, it was possible to incorporate only the lower surface leading edge region solution for flat supersonic leading edge cases. It is relatively straightforward to generalize this idea for other leading edge geometries.

During the present investigation, the impulsive start technique ("Initial Conditions" section) was used extensively to initialize the flow. In all cases, the transients disappeared and the asymptotic conical or nonconical solution was obtained. However, this was somewhat costly in computer time and it was shown that more realistic initial conditions, such as tangent wedge or cone, speed up the calculations. It would be best in the future, however, to use exact initial conditions that could come from a blunt-body program for aircraft with blunt noses or from a conical-flow program for aircraft with conical forebodies.

Since the time of the original implementation of the Lax-Wendroff techniques described in "Differencing Method for Update of Body Points," it has been noted (refs. 7 and 25) that there are more sophisticated and accurate versions of this method. The utility of these other Lax-Wendroff variants as well as some of the better first-order methods could very easily be tested.

A more accurate and simple technique has been developed for overlapping the surface mesh and the basic Cartesian mesh in the two-dimensional transonic program. This technique could also be used in future versions of the present program.

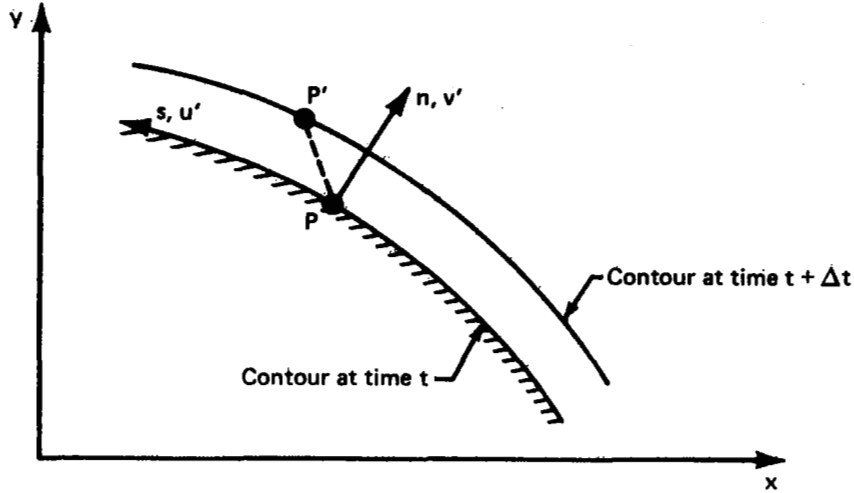
It is also felt that future versions of this program should include plot packages. The plot packages would be used to check out the input geometry as well as plot out the flow-field variables. This latter capability is especially useful in obtaining a good understanding of the nature of the computed fluid mechanics.

The computer program was specifically written so as to ensure a maximum degree of flexibility. This is a very attractive feature since all the suggested improvements or experiments mentioned so far would result in relatively minor modifications to the program.

In summary, it is felt that, with the present program, a very significant step has been made in developing a method that can be used to analyze SST, HST, and space shuttle-type configurations. Due to the basic simplicity and dependability of this method, the groundwork has been laid for future improvements of, and extensions to, the present program.

APPENDIX A BOUNDARY UPDATE SCHEME BND1 (CONSERVATIVE DIFFERENCING)

The conservative boundary update scheme attempts to update the boundary point using a modification to the Lax-Wendroff technique described in "Grid System" in the main text.



In the above sketch, the boundary contour is shown at two different time levels. The point P moves both tangentially, at speed $\dot{\gamma}$, and normally at speed $\dot{\lambda}$. A new relative coordinate system is defined by

$$\tilde{n} = n - \dot{\lambda}t$$

$$\tilde{s} = s - \dot{\gamma}t$$

and relative normal velocity

$$\tilde{v} = v' - \dot{\lambda}(t)$$

$$\tilde{u} = u'$$

\tilde{n} and \tilde{s} are relative coordinates and \tilde{v} is a relative velocity. The equations of motion in \tilde{s}, \tilde{n} coordinate system become

$$\frac{\partial W}{\partial t} + \frac{\partial f}{\partial n} + \frac{1}{1 + \frac{\tilde{n} + \lambda(t)}{R(s)}} \frac{\partial g}{\partial \tilde{s}} + h - \dot{\gamma} \frac{\partial W}{\partial \tilde{s}} = 0$$

where:

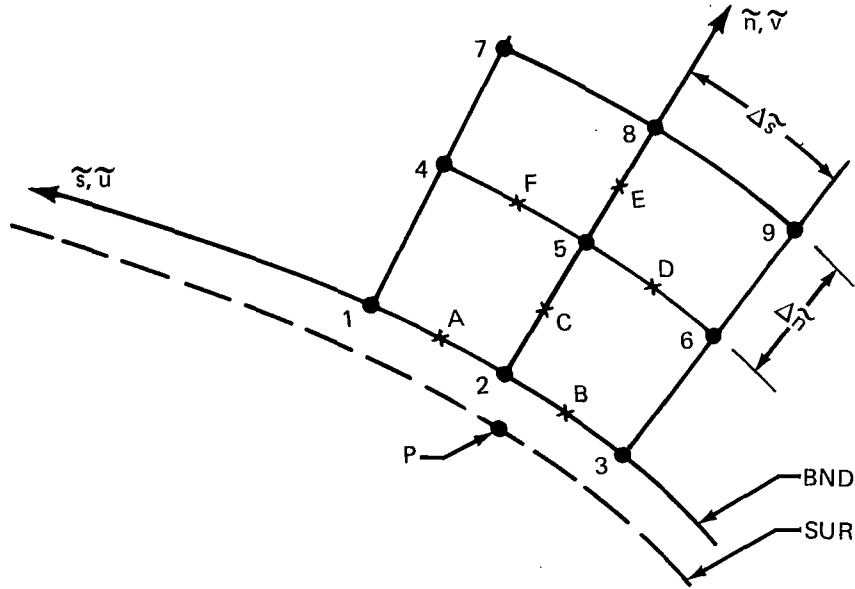
$$W = [\rho, \rho \tilde{v}, \rho \tilde{u}, \rho \tilde{s}]$$

$$f = [\rho \tilde{v}, p/\gamma \beta^2 + \rho \tilde{v}^2, \rho \tilde{u} \tilde{v}, \rho \tilde{v} \tilde{s}]$$

$$g = [\rho \tilde{u}, \rho \tilde{u} \tilde{u}, p/\gamma \beta^2 + \rho \tilde{u}^2, \rho \tilde{u} \tilde{s}]$$

$$h = \{1/[\tilde{n} + R(s) + \lambda(t)]\} \{ \rho[\tilde{v} + \lambda(t)], \rho[\tilde{v}^2 - \tilde{u}^2] + \rho \lambda \tilde{v} \\ + \rho \ddot{\lambda} [R + \lambda(t) + \tilde{n}], 2\rho \tilde{v} [\dot{\lambda} + \tilde{v}], \rho [\dot{\lambda} + \tilde{v}] \tilde{s} \}$$

The numerical solution to the above equation is considered next. The grid setup is shown below in the relative \tilde{s}, \tilde{n} coordinate system.



The central idea of the method is to attempt to update point 2, which is located a half mesh space away from the (relative) surface, using only the half-time level information at points A, B, and C and using the fact that there is no (relative) flow-through surface. Examination of the equations shows that this is possible for all quantities except $\rho \tilde{v}$.

To obtain $\rho \tilde{v}$ at point 2, we interpolate between the updated value of $\rho \tilde{v}$ at point 5 and the fact that $\rho \tilde{v} = 0$ at the surface point P.

1) Half-time levels

The half-time levels are updated as follows:

a) Compute $W(1, 2, 3, 4)$

$$W_F = \frac{W_5 + W_4}{2} - \frac{\Delta t}{2} \left\{ \frac{(f_7 + f_8) - (f_1 + f_2)}{4\Delta\tilde{n}} \right.$$

$$+ \frac{1}{\Delta\tilde{n}_2} (g_4 - g_5) \\ \left. 1 + \frac{R_2 + R_1}{\Delta\tilde{n}_2} \right\}$$

$$+ \frac{h_5 + h_4}{2} \left\{ + \frac{\Delta t}{2} \frac{\dot{\gamma}(0)}{\Delta\tilde{s}} (W_4 - W_5) \right.$$

$$W_E = \frac{W_8 + W_5}{2} - \frac{\Delta t}{2} \left\{ \frac{f_8 - f_5}{\Delta\tilde{n}} \right.$$

$$+ \frac{1}{1 + \frac{3/2\Delta\tilde{n}}{R_2}} \left[\frac{(g_7 + g_4) - (g_9 + g_6)}{4\Delta\tilde{s}} \right]$$

$$+ \frac{h_5 + h_8}{2} \left\{ + \frac{\Delta t}{2} \frac{\dot{\gamma}(0)}{4\Delta\tilde{s}} (W_7 + W_4 - W_9 - W_6) \right.$$

$$W_D = \frac{W_5 + W_6}{2} - \frac{\Delta t}{2} \left\{ \frac{(f_8 + f_9) - (f_2 + f_3)}{4\Delta\tilde{n}} \right.$$

$$+ \frac{1}{1 + \frac{\Delta\tilde{n}_2}{R_2 + R_3}} \left(\frac{g_5 - g_6}{\Delta\tilde{s}} + \frac{h_5 + h_6}{2} \right) \left\{ \right.$$

$$+ \frac{\Delta t}{2} \frac{\dot{\gamma}(0)}{\Delta\tilde{s}} (W_5 - W_6)$$

$$W_C = \frac{W_5 + W_2}{2} - \frac{\Delta t}{2} \left\{ \frac{f_5 - f_1}{\Delta\tilde{n}} \right.$$

$$+ \frac{1}{1 + \frac{\Delta\tilde{n}}{2R_2}} \left[\frac{(g_4 + g_1) - (g_6 + g_3)}{4\Delta\tilde{s}} \right]$$

$$+ \frac{h_5 + h_2}{2} \left\{ + \frac{\Delta t}{2} \frac{\dot{\gamma}(0)}{4\Delta\tilde{s}} (W_4 + W_1 - W_3 - W_6) \right.$$

$$\begin{aligned}
W_5\left(t + \frac{\Delta t}{2}\right) &= W_5(t) - \frac{\Delta t}{2} \left\{ \frac{f_8 - f_2}{2\Delta\tilde{n}} \right. \\
&\quad \left. + \frac{1}{1 + \frac{\Delta\tilde{n}}{R_2}} \left(\frac{g_4 - g_6}{2\Delta\tilde{s}} \right) + h_5 \right\} \\
&\quad + \frac{\Delta t}{2} \frac{\dot{\gamma}(0)}{2\Delta\tilde{s}} (W_4 - W_6)
\end{aligned}$$

b) Compute $W(1, 3, 4)$ only at points A, B, and 2.

$$\begin{aligned}
W_A &= \frac{W_1 + W_2}{2} - \frac{\Delta t}{2} \left\{ \frac{f_1 + f_2 + f_4 + f_5}{4\Delta\tilde{n}} \right. \\
&\quad \left. + \frac{g_1 - g_2}{\Delta\tilde{s}} + \frac{h_2 + h_1}{2} \right\} \\
&\quad + \frac{\Delta t}{2} \frac{\dot{\gamma}(0)}{\Delta\tilde{s}} (W_1 - W_2)
\end{aligned}$$

$$\begin{aligned}
W_B &= \frac{W_2 + W_3}{2} - \frac{\Delta t}{2} \left\{ \frac{f_2 + f_3 + f_5 + f_6}{4\Delta\tilde{n}} \right. \\
&\quad \left. + \frac{g_2 - g_3}{\Delta\tilde{s}} + \frac{h_2 + h_3}{2} \right\} \\
&\quad + \frac{\Delta t}{2} \frac{\dot{\gamma}(0)}{\Delta\tilde{s}} (W_2 - W_3)
\end{aligned}$$

$$\begin{aligned}
W_2\left(t + \frac{\Delta t}{2}\right) &= W_2(t) - \frac{\Delta t}{2} \left\{ \frac{f_5 + f_2}{2\Delta\tilde{n}} + \frac{g_1 - g_3}{2\Delta\tilde{s}} + h_2 \right\} \\
&\quad + \frac{\Delta t}{2} \frac{\dot{\gamma}(0)}{2\Delta\tilde{s}} (W_1 - W_3)
\end{aligned}$$

$$W_2(2) = \frac{W_C(2)}{2}$$

c) Compute F, G, and H at half-time level from above results.

2) Full-time levels

a) Boundary values

$$\begin{aligned}
 W_5(\Delta t) = & W_5(0) - \Delta t \left\{ \frac{f_E - f_C}{\Delta \tilde{n}} \right. \\
 & + \frac{1}{1 + \frac{\Delta \tilde{n} + \lambda(\Delta t/2)}{R_2}} \left(\frac{g_F - g_D}{\Delta \tilde{s}} \right) + h_5 \left. \right\}_{t+\frac{\Delta t}{2}} \\
 & + \Delta t \dot{\gamma} \left(t + \frac{\Delta t}{2} \right) \left(\frac{W_F - W_D}{\Delta \tilde{s}} \right)_{t+\frac{\Delta t}{2}}
 \end{aligned}$$

Except for $W_2(2)$

$$\begin{aligned}
 W_2(\Delta t) = & W_2(t) - \Delta t \left\{ \frac{f_C}{\Delta \tilde{n}} \right. \\
 & + \frac{1}{1 + \frac{\lambda(\Delta t/2)}{R_2}} \left(\frac{g_A - g_B}{\Delta \tilde{s}} \right) + h_2 \left. \right\}_{t+\frac{\Delta t}{2}} \\
 & + \Delta t \dot{\gamma} \left(t + \frac{\Delta t}{2} \right) \left(\frac{W_A - W_B}{\Delta \tilde{s}} \right)_{t+\frac{\Delta t}{2}}
 \end{aligned}$$

For $W_2(2)$

$$W_2(2, \Delta t) = \frac{W_5(2, t + \Delta t)}{3}$$

b) Surface values

The values of the properties at the surface point P are determined by extrapolating the updated results at points 2 and 5 as follows:

$$WS1 = \frac{1}{2} \left[3W_1(2) - W_1(5) \right]_{t+\Delta t}$$

$$WS2 = 0$$

$$WS3 = \frac{1}{2} \left[3W_3(2) - W_3(5) \right]_{t+\Delta t}$$

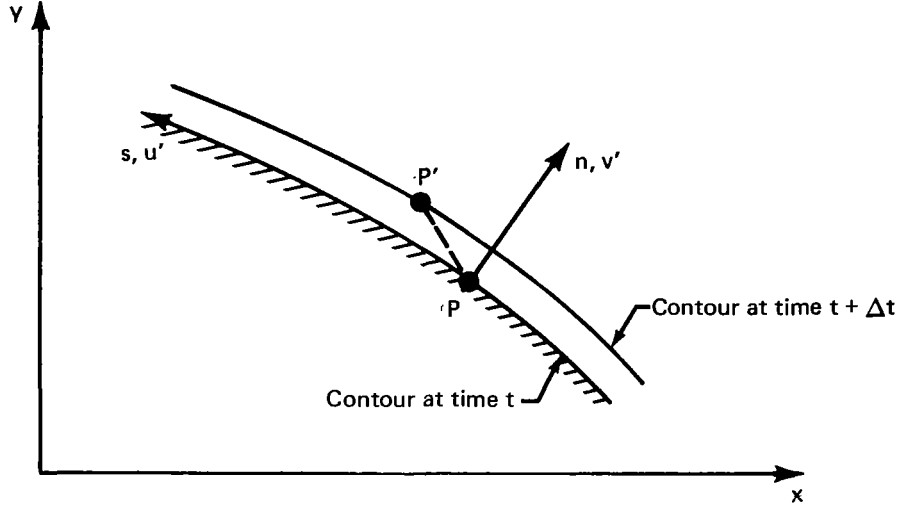
$$WS4 = \frac{1}{2} \left[3W_4(2) - W_4(5) \right]$$

Extrapolation is generally a very undesirable process (at least numerically) since it often leads to instabilities. However, this is not the case in BND1 since the WS values are used only for printout purposes. The WS values do not interact with the other computations (which could easily lead to an instability) since, when points 2 and 5 are updated, the only fact used is that there is no flow through the surface.

APPENDIX B BOUNDARY UPDATE SCHEME BND3 (METHOD OF CHARACTERISTICS)

Characteristic Equations in Body Coordinates

A segment of a typical body contour is shown in the sketch below for two different time levels.



The body coordinates are the arc length s and the distance from the contour along the outward normal n . The boundary contour actually distorts with time. However, in this development we adopt the point of view that we have a sequence of fixed body coordinate systems that happen to correspond to the boundary contour at each time level. This means we neglect rotation of the boundary contour, and hence the scheme is second order accurate only for a special class of bodies. We see that point P has in general both a tangential velocity component ($\dot{\gamma}$) and a normal component ($v'\delta$).

We work in a coordinate system moving with tangential speed $\dot{\gamma}$ and define the relative coordinates

$$\tilde{s} = s - \dot{\gamma}t$$

In terms of \tilde{s} , n , the characteristics equation necessary to update the boundary properties at point P are:

$$\left. \frac{du'}{dt} \right|_I = - \frac{c(x)}{1 + c(x)n} u' v' - \frac{1}{1 + c(x)n} \left\{ \frac{1}{2} \frac{\partial (u')^2}{\partial \tilde{s}} + \frac{1}{\gamma M_\infty^2} \frac{1}{\rho} \frac{\partial p}{\partial \tilde{s}} \right\} + \dot{\gamma} \frac{\partial u'}{\partial \tilde{s}} \quad (14a)$$

$$\left. \frac{d\bar{S}}{dt} \right|_I = - \frac{1}{1 + c(x)n} u' \frac{\partial \bar{S}}{\partial \bar{s}} + \gamma \frac{\partial \bar{S}}{\partial \bar{s}} \quad (14b)$$

$$\left. \frac{dn}{dt} \right|_{II} = v' - a \quad (15a)$$

$$\begin{aligned} \left. \frac{d}{dt} \left(v' - \frac{2a}{\gamma-1} \right) \right|_{II} + \frac{a}{\gamma(\gamma-1)} \left. \frac{d(\ln \bar{S})}{dt} \right|_{II} &= \frac{c(x)}{1 + c(x)n} [(u')^2 + av'] + \\ &\frac{1}{1 + c(x)n} \left\{ \frac{a}{\rho} \frac{\partial(\rho u')}{\partial \bar{s}} - u' \frac{\partial v'}{\partial \bar{s}} + \frac{a u'}{\gamma} \frac{\partial(\ln \bar{S})}{\partial \bar{s}} \right\} + \gamma \left\{ \frac{\partial v'}{\partial \bar{s}} - \frac{a}{\rho} \frac{\partial \rho}{\partial \bar{s}} - \frac{a}{\gamma \bar{s}} \frac{\partial \bar{S}}{\partial \bar{s}} \right\} \end{aligned} \quad (15b)$$

with:

$$p = \bar{S} \rho \gamma$$

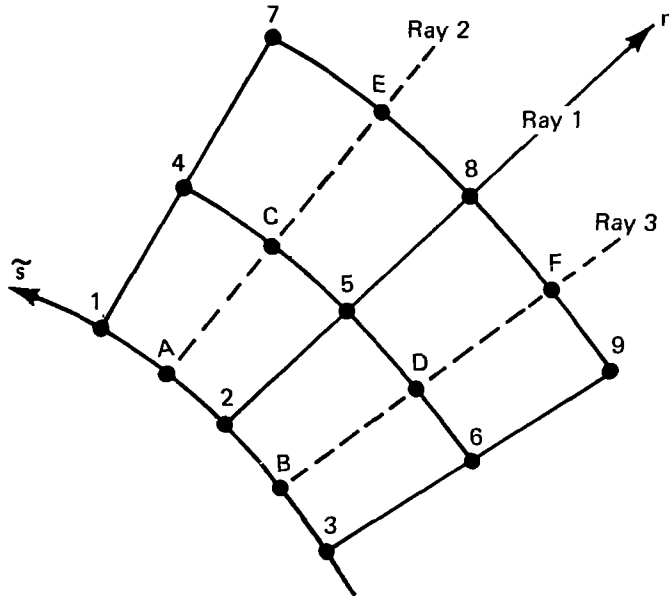
$$T = p/\rho$$

$$a = \sqrt{T}/M_\infty$$

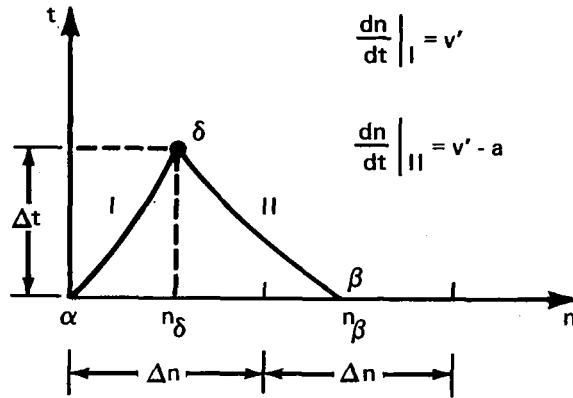
When using unified theory, M_∞ should be replaced by $\sqrt{M_\infty^2 - 1}$. In the above equations, the coordinate \bar{s} is measured relative to the moving point P.

Finite-Difference Scheme

In setting up the scheme, a modified Euler method was used. It is a two-step method, and there are no stability problems. The body coordinate grid to be used is labeled as follows.



The flow properties at time level t are needed only at the numbered points. Along each of rays 1, 2, 3, a characteristics intersection problem must be solved. The nomenclature to be used is indicated below.



The location n_δ , the normal velocity v'_δ , and tangential velocity component $\dot{\gamma}$ will be regarded as known in the following development. They are actually determined by the geometry package. Consistent with our neglect of rotation effects, we will assume v'_α , n_δ , v'_δ are the same for rays 1, 2, and 3.

There are four steps to get the final properties at point δ along ray 1.

- 1) Equations (14a) and (14b) \hat{S} are solved for tentative values of u' and S at point δ on rays 2 and 3 (denoted by \hat{u}'_δ and \hat{S}_δ).
- 2) Equations (15a) and (15b) are solved for tentative values of a and n_β along rays 2 and 3 (denoted by \hat{a}_β and \hat{n}_β).
- 3) The right sides of equations (14a) and (14b) are averaged between time t and $t + \Delta t$, and final values of u' and \bar{S} at point δ on ray 1 are determined (denoted by u'_δ and \bar{S}_δ).
- 4) The right hand sides of equations (15a) and (15b) are averaged between time t and $t + \Delta t$, and final values of a and n_β on ray 1 are determined denoted by a_δ and n_β).

Further details on each step are given as follows.

Step 1.—

$$\hat{u}'_{\delta(A)} = \hat{u}'_\delta|_{\text{ray 2}} = \frac{1}{2} [u'(1, t) + u'(2, t)] \left[1 - C_A v'_\alpha \Delta t \right] - \frac{\Delta t}{\Delta \bar{S}} \left\{ \frac{1}{2} [u'(1, t)]^2 - (u'(2, t))^2 \right\} +$$

$$\frac{2}{\gamma_{M_\infty}^2} \frac{p(1, t) - p(2, t)}{\rho(1, t) + \rho(2, t)} \left\{ + \dot{\gamma} \frac{\Delta t}{\Delta \bar{S}} [u'(1, t) - u'(2, t)] \right\}$$

$$\begin{aligned} \frac{\hat{S}_\delta(A)}{\hat{S}_\delta(B)} = \frac{\hat{S}_\delta}{\text{ray 2}} = \frac{1}{2} [\bar{S}(1, t) + \bar{S}(2, t)] - \frac{\Delta t}{\Delta \bar{S}} \frac{1}{2} [u'(1, t) + u'(2, t)] [\bar{S}(1, t) - \bar{S}(2, t)] + \\ \gamma \frac{\Delta t}{\Delta \bar{S}} [\bar{S}(1, t) - \bar{S}(2, t)] \end{aligned}$$

with similar expressions along ray 3 for $\hat{u}'_\delta(B)$ and $\hat{S}_\delta(B)$.

Step 2.—Define along ray 2.

$$\begin{aligned} G(n) = \frac{n_\delta - n}{\Delta t} - [v'(n) - a(n)] \\ \approx G_A - \left(\frac{3G_A - 4G_C + G_E}{2} \right) \left(\frac{n}{\Delta n} \right) + \left(\frac{G_A - 2G_C + G_E}{2} \right) \left(\frac{n}{\Delta n} \right)^2 \end{aligned}$$

with G_A , G_C , and G_E being the value of $G(n)$ evaluated at the appropriate point in the body coordinate grid. For example:

$$G_C = \frac{n_\delta - \Delta n}{\Delta t} - \frac{1}{2} [v'(4, t) + v'(5, t) - a(4, t) - a(5, t)]$$

when n_β is taken as the smallest positive root of the parabolic approximate of $G(n)$. To avoid round-off error problems in arriving at this root, it may be useful to recognize that if n_1 and n_2 are two roots of the equation $n^2 + C_1 n + C_0 = 0$, then they are related by $n_2 = C_0/n_1$. This is generally useful when n_1 is the largest root and C_0 is small.

Once \hat{n}_β has been determined, the flow properties \hat{v}'_β , \hat{a}_β , and \hat{S}_β can be evaluated by quadratic interpolation along ray 2. Then \hat{a}_β is determined by the equation

$$\left(\hat{v}'_\delta - \frac{2\hat{a}_\delta}{\gamma - 1} \right) - \left(\hat{v}'_\beta - \frac{2\hat{a}_\beta}{\gamma - 1} \right) + \frac{\hat{a}_\beta}{\gamma(\gamma - 1)} [\ln \hat{S}_\delta - \ln \hat{S}_\beta] = \Delta t F(\hat{n}_\beta)$$

where

$$\begin{aligned} F(n) = \frac{C_A}{1 + C_A n} [(u')^2 + av'] + \frac{1}{1 + C_A n} \left\{ \frac{a}{\rho} \frac{\partial(\rho u')}{\partial \bar{S}} - u' \frac{\partial v'}{\partial \bar{S}} + \frac{au'}{\gamma} \frac{\partial \ln \bar{S}}{\partial \bar{S}} \right\} + \gamma \left\{ \frac{\partial v'}{\partial \bar{S}} - \frac{a}{\rho} \frac{\partial \rho}{\partial \bar{S}} - \frac{a}{\gamma \bar{S}} \frac{\partial \bar{S}}{\partial \bar{S}} \right\} \\ \approx F_A - \left(\frac{3F_A - 4F_C + F_E}{2} \right) \left(\frac{n}{\Delta n} \right) + \left(\frac{F_A - 2F_C + F_E}{2} \right) \left(\frac{n}{\Delta n} \right)^2 \end{aligned}$$

F_A , F_C , and F_E are evaluated by averaging and central differencing the flow properties at the (nine) numbered grid points where they are known, for example,

$$u'(A, t) = \frac{1}{2} [u'(1, t) + u'(2, t)]$$

and

$$\frac{\partial v'}{\partial s}(A, t) = \frac{1}{\Delta s} [v'(1, t) - v'(2, t)]$$

A similar procedure can be applied along ray 3. This gives tentative values of u'_δ , \bar{s}_δ , a_δ , and hence all flow properties, determined along rays 2 and 3 at the next time level.

Step 3.—Along ray 1,

$$\begin{aligned} u'_\delta = u'(2, t) + \frac{1}{2} \left\{ -C_2 \Delta t u'(2, t) v'_\alpha - \frac{\Delta t}{2\Delta s} \left[\frac{(u'(1, t))^2}{2} - \frac{(u'(3, t))^2}{2} + \right. \right. \\ \left. \left. \frac{1}{\gamma \beta^2} \left(\frac{p(1, t) - p(3, t)}{\rho(2, t)} \right) \right] \right\} + \frac{1}{2(1 + \bar{c}_2 n_\delta)} \left\{ -\bar{c}_2 \Delta t \left(\frac{\hat{u}'_\delta(A) + \hat{u}'_\delta(B)}{2} \right) v'_\delta \right. \\ \left. - \frac{\Delta t}{\Delta s} \left[\frac{(\hat{u}'_\delta(A))^2}{2} - \frac{(\hat{u}'_\delta(B))^2}{2} + \frac{(\hat{p}_\delta(A) - \hat{p}_\delta(B))}{\rho_\delta(A) + \rho_\delta(B)} \frac{2}{\gamma \beta^2} \right] \right\} + \\ \frac{1}{2} \left\{ \dot{\gamma}(t) \left[\frac{\Delta t}{2\Delta s} \right] [u'(1, t) - u'(3, t)] + \dot{\gamma}(t + \Delta t) \left[\frac{\Delta t}{\Delta s} \right] [\hat{u}'_\delta(A) - \hat{u}'_\delta(B)] \right\} \end{aligned}$$

and

$$\begin{aligned} \bar{s}_\delta = \bar{s}(2, t) + \frac{1}{2} \left\{ -\frac{\Delta t}{2\Delta s} [u'(2, t)] [\bar{s}(1, t) - \bar{s}(3, t)] \right\} + \\ \frac{1}{2(1 + \bar{c}_2 n_\delta)} \left\{ -\frac{\Delta t}{\Delta s} \left[\frac{\hat{u}'_\delta(A) + \hat{u}'_\delta(B)}{2} \right] \left[\frac{\hat{s}_\delta(A) - \hat{s}_\delta(B)}{2} \right] \right\} + \frac{1}{2} \left\{ \dot{\gamma}(t) \frac{\Delta t}{2\Delta s} [\bar{s}(1, t) \right. \\ \left. - \bar{s}(3, t)] + \dot{\gamma}(t + \Delta t) \frac{\Delta t}{\Delta s} [\hat{s}_\delta(A) - \hat{s}_\delta(B)] \right\} \end{aligned}$$

where

$$\bar{c}_2 = c(\bar{s}_2 + \dot{\gamma} \Delta t)$$

$$= c_2 + (\dot{\gamma} \Delta t) \left[\frac{c_1 - c_3}{2\Delta \bar{s}} \right]$$

Step 4.—In this case, along ray 1,

$$G(n) = \frac{n_\delta - n}{\Delta t} - \frac{1}{2} \left[v'(n) - a(n) + v'_\delta - \hat{a}_\delta \right]$$

$$\approx G_2 - \left(\frac{3G_2 - 4G_5 + G_8}{2} \right) \left(\frac{n}{\Delta n} \right) + \left(\frac{G_2 - 2G_5 + G_8}{2} \right) \left(\frac{n}{\Delta n} \right)^2$$

and n_β is taken as the smallest positive root of the parabolic approximate of $G(n)$. Once n_β has been determined, v'_β , a_β , and \bar{s}_β can be evaluated by quadratic interpolation along ray 1. Then a δ is taken as determined by the equation

$$\left(v'_\delta - \frac{2a_\delta}{\gamma - 1} \right) - \left(v'_\beta - \frac{2a_\beta}{\gamma - 1} \right) + \frac{\frac{1}{2}a_\beta + \frac{1}{4}[\hat{a}_\delta(A) + \hat{a}_\delta(B)]}{\gamma(\gamma - 1)} \left[\ln \bar{s}_\delta - \ln \bar{s}_\beta \right] = \frac{\Delta t}{2} \left\{ F(n_\beta) \right\} +$$

$$\frac{\Delta t}{2} \left\langle \left(\frac{c_2}{1 + c_2 n_\delta} \right) \right\{ \left[\frac{\hat{u}'_\delta(A) + \hat{u}'_\delta(B)}{2} \right]^2 + \left[\frac{\hat{a}_\delta(A) + \hat{a}_\delta(B)}{2} \right] v'_\delta \right\} + \left(\frac{1}{1 + c_2 n_\delta} \right) \bullet$$

$$\left\{ \frac{\hat{a}_\delta(A) + \hat{a}_\delta(B)}{\hat{\rho}_\delta(A) + \hat{\rho}_\delta(B)} \left[\hat{\rho}_\delta(A) \hat{u}'_\delta(A) - \hat{\rho}_\delta(B) \hat{u}'_\delta(B) \right] + \right.$$

$$\left. \frac{1}{\gamma} \left[\frac{\hat{a}_\delta(A) + \hat{a}_\delta(B)}{2} \right] \left[\frac{\hat{u}'_\delta(A) + \hat{u}'_\delta(B)}{2} \right] \left[\ln \hat{\bar{s}}_\delta(A) - \ln \hat{\bar{s}}_\delta(B) \right] \right\} + \frac{1}{2} \dot{\gamma}(t + \Delta t) \Delta t \left\{ - \right.$$

$$\left. \left[\frac{\hat{a}_\delta(A) + \hat{a}_\delta(B)}{\hat{\rho}_\delta(A) + \hat{\rho}_\delta(B)} \right] \left[\frac{\hat{\rho}_\delta(A) - \hat{\rho}_\delta(B)}{\Delta \bar{s}} \right] - \frac{1}{\gamma} \left[\frac{\hat{a}_\delta(A) + \hat{a}_\delta(B)}{\hat{\bar{s}}_\delta(A) + \hat{\bar{s}}_\delta(B)} \right] \left[\frac{\hat{\bar{s}}_\delta(A) - \hat{\bar{s}}_\delta(B)}{\Delta \bar{s}} \right] \right\}$$

with

$$F(n) = \frac{c_2}{1 + c_2 n} \left((u')^2 + a v' \right) + \frac{1}{1 + c_2 n} \left\{ \frac{a}{\rho} \frac{\partial(\rho u')}{\partial \bar{x}} - u' \frac{\partial v'}{\partial \bar{x}} + \frac{a u'}{\gamma} \frac{\partial(\ln \bar{S})}{\partial \bar{x}} \right\} + \gamma \left\{ \frac{\partial v'}{\partial \bar{x}} - \frac{a}{\rho} \frac{\partial \rho}{\partial \bar{x}} - \frac{a}{\gamma \bar{S}} \frac{\partial \bar{S}}{\partial \bar{x}} \right\}$$

$$\approx F_2 - \left(\frac{3F_2 - 4F_5 + F_8}{2} \right) \left(\frac{n}{\Delta n} \right) + \left(\frac{F_2 - 2F_5 + F_8}{2} \right) \left(\frac{n}{\Delta n} \right)^2$$

and F_2, F_5, F_8 evaluated using the values of the flow properties along ray 1 at time t and central differencing.

Once $u'_\delta, \bar{S}_\delta$, and a_δ are known, all the other flow properties can be evaluated using the perfect gas law, and the boundary point is updated to the new time level.

APPENDIX C

INTERPOLATION SECTIONS FOR A GENERAL BODY

The surface interpolation procedure, described in "Geometry Definition" of the main text, requires a contour pair for each interpolation section with the same number of points, the same number of continuous segments, and similar spline boundary conditions. The user will often not have data of this sort. Therefore, a procedure is provided that will accept dissimilar definitions of the contour pair and render them similar. The procedure is implemented in the REDBOD package (see app. D) and discussed below.

To introduce the scheme, suppose the two contours of figure 36 are continuous (one segment). (Later the more general case will be considered.) Suppose there are two contours, 1 and 2, associated with times t_1 and t_2 , respectively. Associate a point Q on contour 2 with a given point P on contour 1. In its more crude form, the rule used is to do this as follows: Let S_1 and S_2 be the arc lengths along 1 and 2 measured from the lower symmetry point and let L_1 and L_2 be the total arc length of the two contours. Then, if point P is located at S_1 , locate point Q on curve 2 at $S_2 = (L_2/L_1)S_1$, i.e., a proportionate distance along curve 2. With this simple rule, there is always a point Q and it is unique. Contour points on intermediate contours are defined by passing a curve through points P and Q.

Unfortunately, the rule just stated is not satisfactory for all contours. The shortcoming is illustrated in figure 36 in which the interpolated dotted contour was constructed graphically with linear interpolation. The fault lies in assuming each segment of the contour distorts in the same way. In this example, the segment corresponding to the wing contour obviously distorts more. This leads to the lag between corresponding points on contours 1 and 2 and causes the interpolated curve to be poorly shaped.

This shortcoming is avoided by applying the rule to segments of the contour that distort in a similar fashion. In the above example, the wing tips, wing-fuselage intersection points, and the fuselage symmetry points would be taken as natural choices defining the ends of each segment. The resulting interpolated curve was constructed graphically and is shown in figure 37. The end points of the segments are circled and are called corresponding points. The interpolated curve is now satisfactory.

To rephrase the rule, the user specifies the location of certain corresponding points on contour 2; the proportional arc length algorithm is then applied between these fixed points to locate the intermediate corresponding points; for convenience, the fixed points are specified by giving a boundary point number, and they are associated with specified points on contour 1 (again specified by point number). The final result is a set of points defining contour 2 that correspond in a specified way to points on contour 1, and the number of points on the two contours are equal.

Now, suppose the two contours have points of curvature and/or slope discontinuity, not necessarily equal in number. The user is then required to include these discontinuity points in the set of specified corresponding points. They can be associated with either continuity or discontinuity points on contour 1. Thus, the number of segments on the final contour pair is made equal, and it is a composite of the number of segments on each of the original contours.

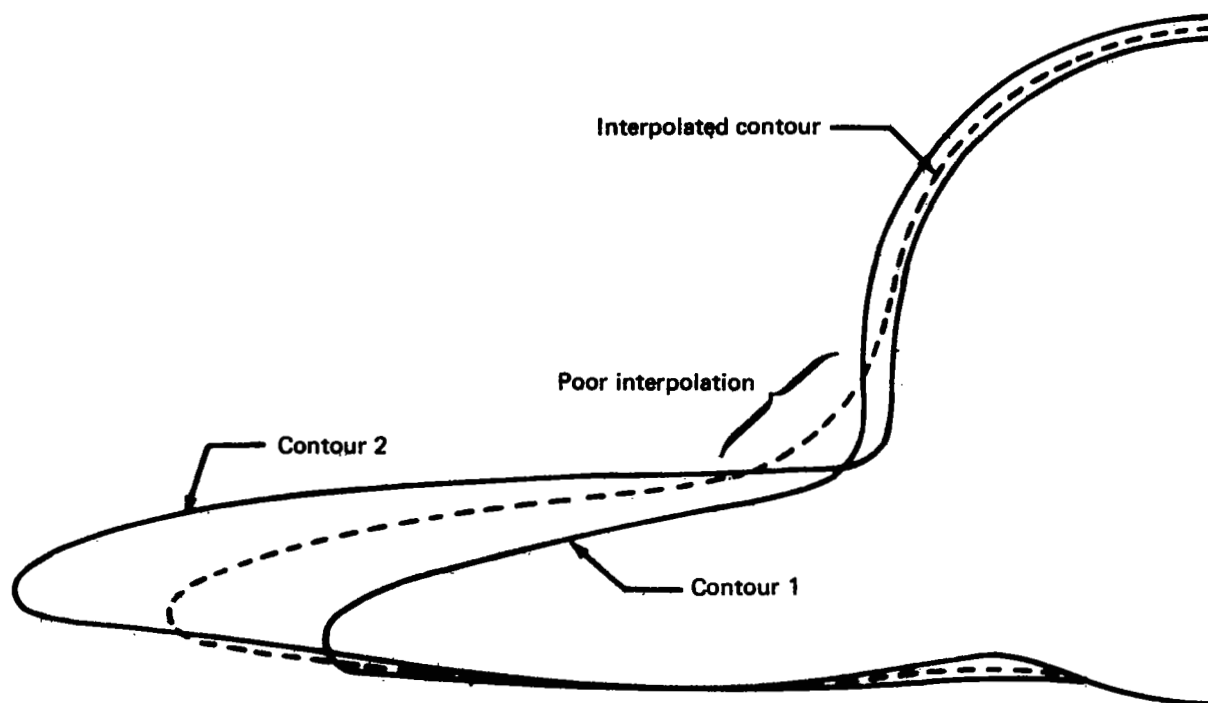


FIGURE 36.—INTERPOLATION WITHOUT CORRESPONDING POINTS

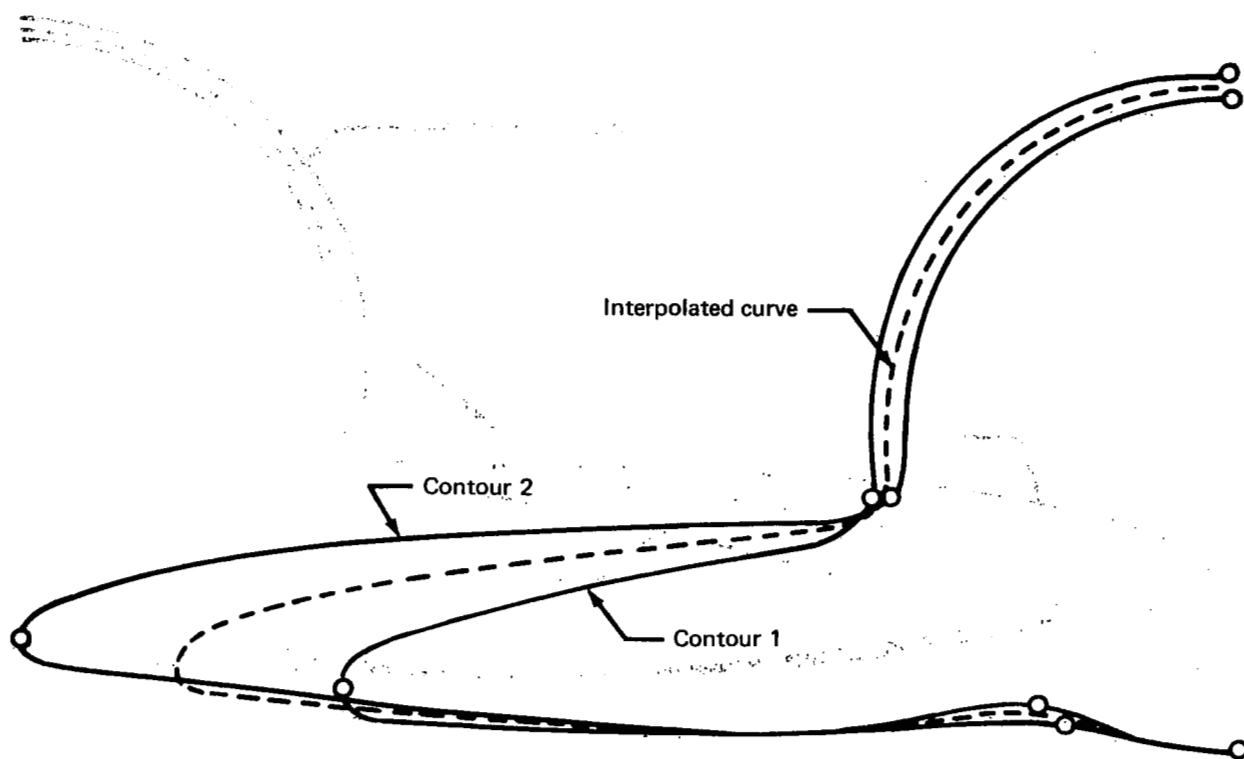


FIGURE 37.—INTERPOLATION WITH CORRESPONDING POINTS

There must be spline boundary conditions associated with each contour segment. On entry to the REDBOD package a spline is constructed through each original set of contour points. These definitions are interpolated to determine the tangent angle on each side of the computed segment end points. Note that the final spline boundary conditions are always in terms of the tangent angle no matter what the input conditions were for each contour.

Once we have two contours with an equal number of points and segments and the same types of spline boundary conditions, determining contours at intermediate times is straightforward. They are simply interpolated linearly (for REDBOD) along the straight line connecting corresponding points. Spline boundary conditions are also interpolated linearly in the event of interior discontinuity points.

The locus of curves thus generated for $t_1 \leq t \leq t_2$ form the surface of the aircraft as seen by the computer program.

APPENDIX D GEOMETRY PACKAGE USAGE

Conical Bodies (CONBOD)

CONBOD accepts a pointwise definition of a contour that is to be used as the directrix of a conical body. Prescribed discontinuities in slope and/or curvature are permissible. The definition of the directrix can be generated in a user-supplied subroutine (BGAUX1) or read in from punched cards. In constructing crosscut contours, the vertex of the conical body is always taken to be the origin of the body coordinates.

Additional subroutines in the package:

BGAUX1 (user supplied)

A description of the data cards is given below.

	<u>Code</u>	<u>Column</u>	<u>Explanation</u>
Card 1	GOMTTL	1-80	Geometry title card
Card 2	NDATA	1-4	Generation control option— READ; read in data cards
		1-8	GENERATE; call BGAUX1
Card Set 3	—		Data in this card set depend on the generation control option on card 2; see discussion below.
Card Set 4	AIFP	1-10	Interpolation section number
	T1	11-20	Axial distance to first of two crosscut contours
	T2	21-30	Axial distance to second contour
Card 5	—		Blank card to indicate end of geometric data set

READ option.—If the READ option is selected on card 2, then the following information should be given on each card in card set 3:

<u>Code</u>	<u>Column</u>	<u>Explanation</u>
X	1-10	The x-coordinate of a contour point
Y	11-20	The y-coordinate of a contour point
NTYP		Point-type option—
	21-30	Blank; normal contour point
	21	D; discontinuous curvature and/or slope
	21-23	END; last point in data set
XNB	31-40	Left-side derivative specification option needed when NTYP=D
		= 1.0; left-side tangent angle given
		= 2.0; left-side curvature given

DB	41-50	If NTYP=D either left-side tangent angle in degrees or left-side curvature, depending on value of XNB, given
XNA	51-60	Right-side derivative specification option needed when NTYP=D = 1.0; right-side tangent angle given = 2.0; right-side curvature given
DA	61-70	If NTYP=D either right-side tangent angle in degrees or right-side curvature, depending on value of XNA, given

GENERATE option.—If the user selects the GENERATE option on card 2, a subroutine BGAUX1 must be supplied with the following calling sequence: CALL BGAUX1 (DELT, N, M, X, Y, NDSC, NDL, DL, NDR, DR)

where

DELT	(=	Distance between the cone vertex and the defined directrix location
N		=	Number of points on the directrix
M		=	Number of segments on the directrix, each having continuous slope and curvature
X(I),Y(I)		=	Arrays defining Cartesian coordinates of the contour points
NDSC(J)		=	Array of indices defining interior points at which slope or curvature is discontinuous
NDL(J)		=	Array defining whether left-side tangent angle (=1) or left-side curvature (=2) is given at the j th discontinuity point
DL(J)		=	Value of left-side tangent angle in radians or left-side curvature at the j th discontinuity point
NDR(J)		=	Array defining whether right-side tangent angle (=1) or right-side curvature (=2) is given at the j th discontinuity point
DR(J)		=	Value of right-side tangent angle in radians or right-side curvature at the j th discontinuity point

The arrays defined above should be dimensioned as X(N), Y(N), NDSC(M), NDL(M), DL(M), NDR(M), DR(M). Data cards read by BGAUX1, if any, will depend on user specifications for writing the routine.

Bodies With Elliptical Cross Sections (ELLBOD)

ELLBOD accepts a pointwise definition of the axial variation of the semimajor and semiminor axis of elliptical crosscut contours. These points are connected by a linear cubic spline with specified slope discontinuities. It is explicitly assumed that the two axes are coincident with the x and y axes, and the semispan (x-direction) can be greater than or less than the semithickness (y-direction). Special provision is made for the case of axisymmetric bodies.

Additional subroutines in the package:

BGAUX1 (POINT-CURVE)

BGAUX2 (LCSPL)

BGAUX3 (INTERP)

A description of the data cards is given below.

	<u>Code</u>	<u>Column</u>	<u>Explanation</u>
Card 1	GOMTTL	1-80	Geometry title card
Card 2	NBOD	1-6 1-6	Contour type option— ELLBOD; elliptical cross section AXISYM; axisymmetric bodies
Card Set 3	—		Read by subroutine BGAUX1 (see below) to define axial variation of semispan
Card Set 4	—		If NBOD=ELLBOD, card set 4 is read by subroutine BGAUX1 (see below) to define axial variation of semi-thickness; delete if NBOD=AXISYM
Card Set 5	AIFP T1 T2 NC	1-10 11-20 21-30 31-40	Interpolation section number Axial distance to first of two crosscut contours Axial distance to second contour Number of contour points
Card 6			Blank card to indicate end of geometric data set

The data cards read by BGAUX1 (card sets 3 and 4 discussed above) follow:

	<u>Code</u>	<u>Column</u>	<u>Explanation</u>
Card 1	TITLE	1-80	Subtitle (or spacing) card
Card 2	T1 Z1 S1	1-10 11-20 21-30	Axial distance to first point Corresponding ordinate Slope at first data point
Card Set 3	T1 —	1-10 11-40	Axial distance to I th point Three dummy fields whose use is determined by the word in columns 41 to 50

NSEG	41-50	Contour segment end code If blank, normal contour point If NSEG is one of control words below, contour point is the end of a contour segment
NEND		Contour end code—
	51-60	Blank; normal contour point
	51-53	END; last point in data set

The data cards are read until an END is encountered in columns 51 to 53. The permissible control words defining contour segment ends are discussed below.

1) **LINE** (columns 41-44)—A straight line is fitted through the previous data point with the previous slope (must have been specified) that ends at the given axial distance; data in columns 11 to 40 are disregarded.

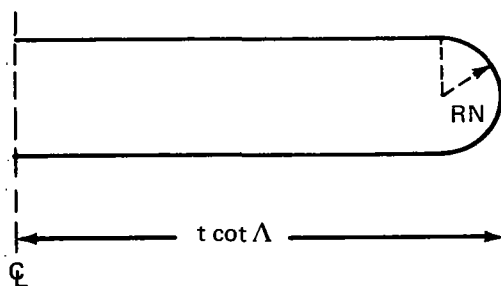
2) **PARABOLA** (columns 41 to 48)—A parabola is fitted through the previous data point with the previous slope (must have been specified) which terminates at the given axial distance with the slope specified in columns 11 to 20.

3) **SLOPE DSC** (columns 41 to 49)—A slope discontinuity occurs at the given axial distance; the ordinate is given in columns 11 to 20, the preceding slope is given in columns 21 to 30, and the succeeding slope is given in columns 31 to 40.

4) **SEG END** (columns 41 to 47)—This would be used to terminate a cubic spline contour segment before the **LINE** or **PARABOLA** option is used as well as at the contour's end point; the ordinate is given in columns 11 to 20 and a slope is given in columns 21 to 30.

Slab-Delta Wings

Slab-delta wing with a circular leading edge (SLBDEL).—SLBDEL accepts parameters defining the wing sweepback angle and nose radius. The generated crosscut contours consist of three curve segments:



the lower straight-line segment, a semicircular arc segment, and the upper straight-line segment. A curvature discontinuity occurs at the nose shoulder points.

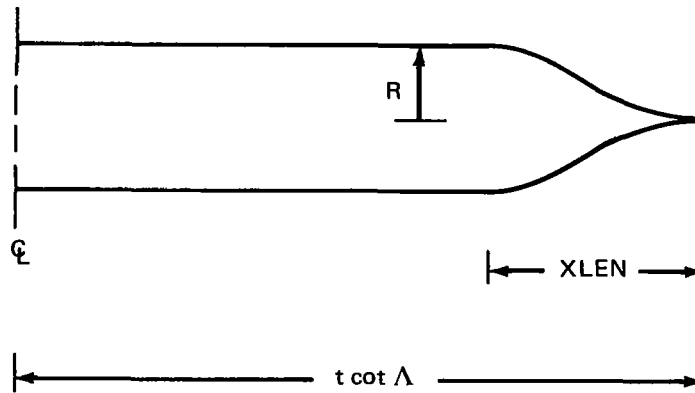
Additional subroutines in the package:

None

A description of the data cards is given below.

	<u>Code</u>	<u>Column</u>	<u>Explanation</u>
Card 1	GOMTTL	1-80	Geometry title card
Card 2	ALAMD	1-10	Sweepback angle in degrees
	RN	11-20	Nose radius
Card Set 3	AIFP	1-10	Interpolation section number
	T1	11-20	Axial distance to first of two crosscut contours
	T2	21-30	Axial distance to second contour
	NN	31-40	Number of equidistant points on the circular nose segment
	NF	41-50	Number of equidistant points on each straight-line segment excluding the shoulder point
Card 4	—		Blank card to indicate end of geometric data set

Slab-delta wing with a cusped leading edge (SLBDEL CUSP).—SLBDEL CUSP accepts parameters defining the wing sweepback angle, the wing semithickness, and the length of the cusped nose section. The generated crosscut contours have four contour segments:



the lower straight-line segment, a lower cubic, an upper cubic, and the upper straight-line segment. A curvature discontinuity occurs at the nose shoulder points and a slope discontinuity occurs at the leading edge.

Additional subroutines in the package:

None

A description of the data cards is given below.

	<u>Code</u>	<u>Column</u>	<u>Explanation</u>
Card 1	GOMTTL	1-80	Geometry title card
Card 2	ALAMD	1-10	Sweepback angle in degrees
	R	11-20	Wing semithickness
	XLEN	21-30	Cusped section length
Card Set 3	AIFP	1-10	Interpolation section number
	T1	11-20	Axial distance to first of two crosscut contours
	T2	21-30	Axial distance to second contour
	NC	31-40	Number of equispaced points on the cusped nose section
	NF	41-50	Number of equidistant points on each straight-line segment excluding the shoulder point
Card 4	—		Blank card to indicate end of geometric data set

Slab-Delta Wing Approximation (SLBDEL APPROX)

SLBDEL APPROX accepts parameters defining the wing sweepback angle (Λ) and the nose curvature (C_0). Crosscut contours are constructed from the parametric equations

$$\left. \begin{aligned} x &= t \cot \Lambda - C_0 (\sqrt{1 + \sigma^2} - 1) \\ y &= \frac{\sigma}{\sqrt{1 + \sigma^2}} - \frac{\sigma}{(1 + \sigma_{\max})^{3/2}} \end{aligned} \right\} -\sigma_{\max} \leq \sigma \leq \sigma_{\max}$$

with

$$\sigma_{\max} = \sqrt{\left(1 + \frac{t \cot \Lambda}{C_0}\right)^2 - 1}$$

For sufficiently large t , these contours are quite similar to the SLBDEL contours, but they have continuous curvature. Note that the user has no control over the thickness of the contour at $x = 0$; we have $y = \pm 1$ for large t . This means that normally, $0.7 \leq C_0 \leq 1.7$ would be chosen.

Additional subroutines in the package:

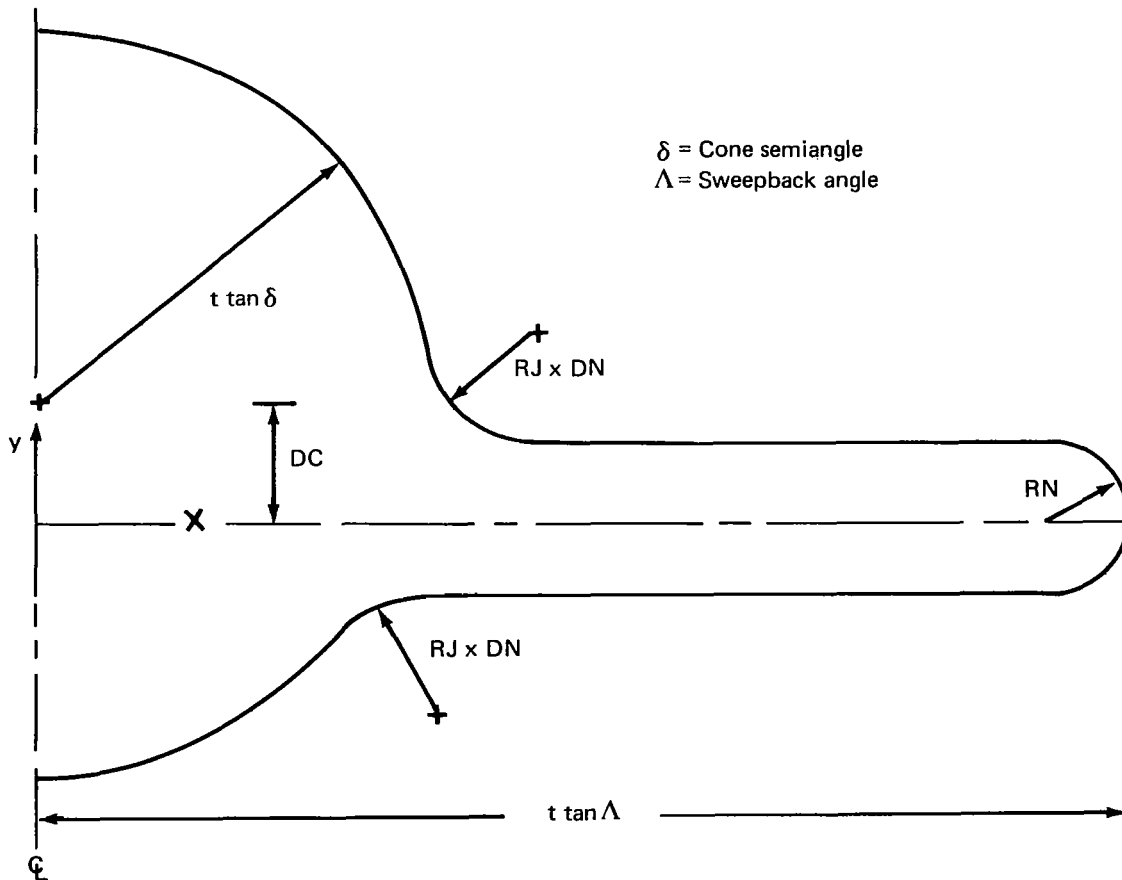
None

A description of the data cards is given below.

	<u>Code</u>	<u>Column</u>	<u>Explanation</u>
Card 1	GOMTTL	1-80	Geometry title card
Card 2	ALAMD	1-10	Sweepback angle in degrees
	C0	11-20	Nose curvature
Card Set 3	AIFP	1-10	Interpolation section number
	T1	11-20	Axial distance to first of two crosscut contours
	T2	21-30	Axial distance to second contour
	N	31-40	Number of points on the crosscut contours at equispaced σ values
Card 4	—		Blank card to indicate end of geometric data set

Wing/Body Combination

Cone/slab-delta wing combination with a circular leading edge (CONE-SLBDEL).—CONE-SLBDEL constructs a simple wing/body combination consisting of a circular cone and a slab-delta wing with a circular nose. The parameters defining a typical crosscut contour are illustrated below.



Circular arc fillets are added at the wing/body intersections to prevent trouble in the boundary update procedure; their radius cannot be less than three times the normal surface coordinate increment, DN. Note that the x-axis is always aligned with the wing centerline. The crosscut contours consist of seven segments, and there are curvature discontinuities between segments.

Additional subroutines in the package:

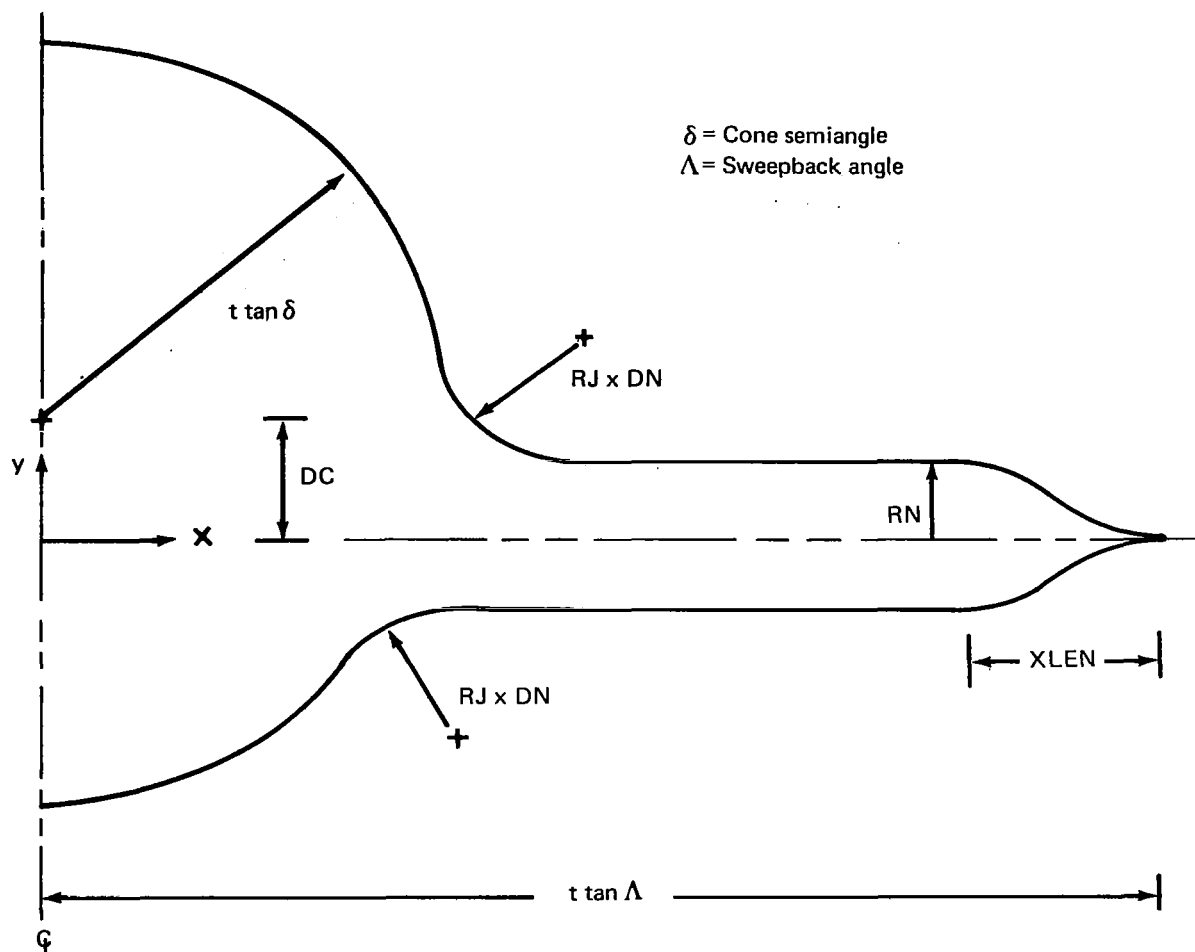
None

A description of data cards is given below.

	<u>Code</u>	<u>Column</u>	<u>Explanation</u>
Card 1	GOMTTL	1-80	Geometry title card
Card 2	ADEL	1-10	Cone semiangle in degrees
	ALAMD	11-20	Sweepback angle in degrees
	DC	21-30	Wing centerline/cone axis displacement; positive for low-wing configuration
	RJ	31-40	Normalized radius (≥ 3) of wing/body fillet
	RN	41-50	Radius of circular nose of the slab-delta wing
Card Set 3	AIFP	1-10	Interpolation section number
	T1	11-20	Axial distance to first of two crosscut contours
	T2	21-30	Axial distance to second contour
	ANB	31-40	$\pi/(ANB-1)$ is the nominal angle of arc between points on the cone crosscut contour; the cone radius times this angle is the nominal distance between points on the flat portions of the wing
	ANN	41-50	Number of points on the wing nose segment including shoulder points
Card 4	—		Blank card to indicate end of geometric data set

Note: A test is made in the routine to determine whether axial distances read in card set 3 are sufficiently large to ensure reasonable geometries. This test ensures that the cone and slab delta intersect properly and checks to be sure the wing shoulder points lie outside the wing/body fillet joining points. If the test is not satisfied, execution terminates.

Cone/slab-delta wing with a cusped leading edge (CONE SLBDEL CUSP).—CONE SLBDEL CUSP constructs a simple wing/body combination consisting of a circular cone and a slab-delta wing with a cusped leading edge. The parameters defining a typical crosscut contour are illustrated below.



Circular arc fillets are added at the wing/body intersections to prevent trouble in the boundary update procedure; their radius cannot be less than three times the normal surface coordinate increment, DN . Note that the x -axis is always aligned with the wing centerline. The crosscut contours consist of eight segments, and there are curvature discontinuities at the fillet end points and the nose shoulder and a slope discontinuity at the wing leading edge.

Additional subroutines in the package:

None

A description of data cards is given below.

	<u>Code</u>	<u>Column</u>	<u>Explanation</u>
Card 1	GOMTTL	1-80	Geometry title card
Card 2	ADELD	1-10	Cone semiangle in degrees
	ALAMD	11-20	Sweepback angle in degrees
	DC	21-30	Wing centerline/cone axis displacement; positive for low-wing configuration
	RJ	31-40	Normalized radius (≥ 3) of wing/body fillet
	RN	41-50	Wing semithickness
	XLEN	51-60	Length of cusped nose segment
Card Set 3	AIFP	1-10	Interpolation section number
	T1	11-20	Axial distance to first of two crosscut contours
	T2	21-30	Axial distance to second contour
	ANB	31-40	$\pi/(ANB-1)$ is the nominal angle of arc between points on the cone crosscut contour; the cone radius times this angle is the nominal distance between points on the flat portions of the wing
	ANN	41-50	Number of points on the wing nose segment including shoulder points
Card 4	—		Blank card to indicate end of geometric data set

Note: A test is made in the routine to determine whether axial distances read in card set 3 are sufficiently large to ensure reasonable geometries. This test ensures that the cone and slab delta intersect properly and checks to be sure the wing shoulder points lie outside the wing/body fillet joining points. If the test is not satisfied, execution terminates.

General Bodies Defined by Read-In Contours (REDBOD)

REDBOD accepts a pointwise definition of crosscut contours in pairs for a general body, wing, or wing-body combination. Each contour may be dissimilar in number of points, number of segments having continuous slope and curvature, and type of spline boundary condition given. The user assigns point numbers to establish a correspondence between contours; these are meant to define segments on the two contours that deform in a similar fashion, and all discontinuity points must be included. Using this information, REDBOD renders the contour pair similar. Reference to appendix C should be made for a discussion of how this is done.

Additional subroutines in the package:

BGAUX1 (CONDEF)
 BGAUX2 (SEG. RELATE)
 BGAUX3 (BOUND.COND.)
 BGAUX4 (CORR.POINT)

The cards read by the REDBOD package deviate in format from the other geometry generation packages. After the *geometry title card*, there is a set of cards for each interpolation section, and the geometry data are followed by a *blank card*. Each interpolation section set contains the cards described below.

	<u>Code</u>	<u>Column</u>	<u>Explanation</u>
Card 1	AIFP	1-10	Interpolation section number
	T1	11-20	Axial distance to first of the crosscut contour pair
	T2	21-30	Axial distance to second contour
	N1		Number of points on first input contour
	N2		Number of points on second input contour
Card 2	TITLE	1-80	Subtitle card for first input contour
Card Set 3	X	1-10	The x-coordinate of a contour point
	Y	11-20	The y-coordinate of a contour point
	ITYP		Point type option—
		21-30	Blank; normal contour point
		21	D; discontinuous slope and/or curvature
	AM	31-40	Left-side derivative specification option needed when ITYP = D = 1.0; left-side tangent angle given = 2.0; left-side curvature given
	BM	41-50	If ITYP=D either left-side tangent angle in degrees or left-side curvature, depending on value of AM given
	AP	51-60	Right-side derivative specification option needed when ITYP=D = 1.0; left-side tangent angle given = 2.0; left-side curvature given
	BP	61-70	If ITYP=D either right-side tangent angle in degrees or right-side curvature, depending on value of AP given
Card 4	TITLE	1-80	Subtitle card for the second input contour
Card Set 5	—		Same input variables as in card set 3 except for the second contour
Card 6	TITLE	1-80	Subtitle card for interior corresponding points
Card Set 7	ICP1	1-10	Interior corresponding point number for first contour
	ICP2	11-20	Interior corresponding point number for second contour
Card 8	NEND	21-23	Word END to indicate end of this section data; columns 24-80 are free for user comments

To illustrate the input procedure, crosscut contours are considered from an early Boeing SST configuration near the wing apex. The input cards are given in table 2. There are five interpolation sections corresponding to the following station intervals:

$T_1 = 1190, T_2 = 1360$ Section 1

$T_1 = 1360, T_2 = 1462$ Section 2

$T_1 = 1462, T_2 = 1658$ Section 3

$T_1 = 1658, T_2 = 1800$ Section 4

$T_1 = 1800, T_2 = 2047$ Section 5

The first section defines the fuselage just before the wing apex, and each crosscut contour is continuous. The remaining interpolation sections include the forming wing. There are slope and curvature discontinuities at the wing/body intersection points that must be specified.

It should be noted that a contour must, in general, be defined as a second contour and then as the first contour in the succeeding interpolation section. These two definitions do not have to be the same, although they should describe essentially the same spline contour. This increases the amount of input data, but the added flexibility can be useful. To illustrate this, consider the contour points given at $z = 1360$ in interpolation sections 1 and 2. Additional points were added in the second definition where the wing will form for $z > 1360$. These points are unnecessary at $z = 1360$, but the definition of the wing crosscut for $1360 < z < 1462$ would not be adequate if they were not included.

Another observation concerns choosing corresponding points. In this example, the contour segment at the wing leading edge is treated as a similarly distorting segment. Contrast this with the use of the leading edge point chosen in appendix C. This is done to ensure that points at the leading edge are sufficiently dense for a cubic spline fit in the region of high curvature. Note also that in section one there are no interior corresponding points given.

At a discontinuity point, the curvature can be given on one side and the tangent angle on the other.

These data cards were input to the REDBOD package to produce the contour point pairs shown in figure 38. Note that the number of contour points on the interpolation pair output by REDBOD is currently taken to be $N1$ (see card 1 above). On the other hand, the number of contour segments is determined by the number of independent discontinuity points on both contours. This is because we allow continuity and discontinuity points to be related as corresponding points.

TABLE 2.—SST INPUT DATA

EARLY SST CONFIGURATION IN THE VICINITY OF THE WING APEX

1.	1190.	1360.	19.	20.
----	-------	-------	-----	-----

FIRST CONTOUR

0.	-30.
15.	-28.
30.	-24.
44.	-18.
58.5	-8.3
70.	2.5
79.5	15.
85.5	28.
89.7	43.
90.	58.
87.5	73.
82.	88.
75.	102.
66.5	114.
54.	125.
41.	132.7
27.5	138.
13.	141.7
0.	142.5

SECOND CONTOUR

0.	-35.
15.	-34.
30.	-30.
44.5	-25.5
57.5	-17.5
69.	-9.
79.	2.
87.5	16.
93.	30.
96.	45.
96.5	60.
94.	75.
90.	88.5
82.7	102.5
73.	116.5
62.	127.5
47.5	137.5
32.5	144.
17.	148.
0.	150.

NO INTERIOR CORRESPONDING POINTS
END OF SECTION 1.

2.	1360.	1462.	25.	29.
----	-------	-------	-----	-----

FIRST CONTOUR

0.	-35.
15.	-34.

TABLE 2.—Continued

30.	-30.					
44.5	-25.5					
57.5	-17.5					
67.5	-10.					
74.	-4.					
76.75	-.8					
79.3	2.5					
81.75	5.9					
84.	9.6					
86.	13.1					
87.9	17.					
93.	30.					
96.	45.					
96.5	60.					
94.	75.					
90.	88.5					
82.7	102.5					
73.	116.5					
62.	127.5					
47.5	137.5					
32.5	144.					
17.	148.					
0.	150.					
SECOND CONTOUR						
0.	-35.5					
15.	-34.5					
30.	-31.					
44.	-26.					
58.	-18.					
68.5	-11.					
75.	-4.5	0	1.	50.	2.	0.
84.	-8.					
90.	-10.					
93.	-10.3					
95.5	-9.					
96.6	-6.7					
96.	-3.					
92.5	4.5					
88.	12.5	0	2.	0.	1.	62.
91.7	18.					
95.	27.					
98.5	39.					
100.	53.					
99.	68.					
96.	82.					
90.	97.					
82.5	110.					
72.5	122.5					
61.	132.5					
47.5	140.7					
32.5	147.5					

TABLE 2.—Continued

16.	151.3
0.	152.5
CORR. POINTS	
7.	7.
9.	10.
11.	12.
13.	15.

END OF SECTION 2.

3.	1462.	1658.	31.	30.		
FIRST CONTOUR						
0.	-35.5					
15.	-34.5					
30.	-31.					
44.	-26.					
58.	-18.					
68.5	-11.					
75.	-4.5	D	1.	50.	2.	0.
79.	-6.					
84.	-8.					
90.	-10.					
93.	-10.3					
95.5	-9.					
96.6	-6.7					
96.	-3.					
93.5	2.5					
91.	7.3					
88.	12.5	D	2.	0.	1.	62.
91.7	18.					
95.	27.					
98.5	39.					
100.	53.					
99.	68.					
96.	82.					
90.	97.					
82.5	110.					
72.5	122.5					
61.	132.5					
47.5	140.7					
32.5	147.5					
16.	151.3					
0.	152.5					
SECOND CURVE						
0.	-35.					
15.	-34.					
30.	-31.					
44.	-25.5					
56.	-18.5					
66.	-10.	D	1.	43.	2.	0.
76.	-15.					
84.5	-18.5					

TABLE 2.—Continued

92.	-20.5					
95.	-20.3					
97.	-19.					
97.6	-17.					
97.	-14.5					
92.	+7.7					
86.	-1.					
80.5	5.	D	2.	0.	1.	55.
88.	17.5					
93.7	30.					
97.5	45.					
98.	60.					
96.	75.					
92.	89.					
85.	103.					
76.	117.3					
65.	128.					
52.5	137.5					
40.	144.					
27.	149.					
14.	151.5					
0.	152.5					
CORR. PCINTS						
7.	6.					
11.	10.					
13.	12.					
17.	16.					

END OF SECTION 3.

4.	1658.	1800.	30.	32.		
FIRST CONTOUR						
0.	-35.					
15.	-34.					
30.	-31.					
44.	-25.5					
56.	-18.5					
66.	-10.	D	1.	43.	2.	0.
76.	-15.					
84.5	-18.5					
92.	-20.5					
95.	-20.3					
97.	-19.					
97.6	-17.					
97.	-14.5					
92.	-7.7					
86.	-1.					
80.5	5.	D	2.	0.	1.	55.
88.	17.5					
93.7	30.					
97.5	45.					
98.	60.					

TABLE 2.—Continued

96.	75.					
92.	89.					
85.	103.					
76.	117.3					
65.	128.					
52.5	137.5					
40.	144.					
27.	149.					
14.	151.5					
0.	152.5					
SECOND CONTOUR						
0.	-35.					
15.	-33.7					
30.	-30.					
44.	-25.					
53.	-20.					
62.	-13.	0	1.	35.	1.	-26.
75.	-19.3					
87.	-22.7					
106.3	-26.3					
125.	-28.					
137.	-29.					
140.8	-27.7					
143.	-25.					
142.9	-21.5					
140.	-17.					
130.	-8.7					
112.	1.5					
98.	9.					
85.	15.5	0	2.	0.	1.	67.
90.	22.					
91.7	31.					
94.5	45.					
95.	60.					
93.	74.					
89.	88.					
82.5	102.					
74.	113.					
64.	124.					
50.	134.					
34.	142.5					
17.5	147.					
0.	149.					
CORR. POINTS						
6.	6.					
10.	12.					
12.	14.					
16.	19.					
END OF SECTION 4.						
5.	1800.	2047.	32.	35.		

TABLE 2.—Continued

FIRST CONTOUR

0.	-35.					
15.	-33.7					
30.	-30.					
44.	-25.					
53.	-20.					
62.	-13.	0	1.	35.	1.	-26.
75.	-19.3					
87.	-22.7					
106.3	-26.3					
125.	-28.					
137.	-29.					
140.8	-27.7					
143.	-25.					
142.9	-21.5					
140.	-17.					
130.	-8.7					
112.	1.5					
98.	9.					
85.	15.5	0	2.	0.	1.	67.
90.	22.					
91.7	31.					
94.5	45.					
95.	60.					
93.	74.					
89.	88.					
82.5	102.					
74.	113.					
64.	124.					
50.	134.					
34.	142.5					
17.5	147.					
0.	149.					

SECOND CONTOUR

0.	-35.					
15.	-33.5					
30.	-29.					
41.	-25.					
50.	-20.	0	1.	30.5	1.	-15.
60.	-22.5					
77.	-25.					
102.	-29.					
125.	-31.					
150.	-30.					
175.	-29.					
200.	-26.					
217.	-24.					
222.	-22.5					
224.25	-18.25					
223.2	-14.2					
219.	-10.					

TABLE 2.—Concluded

209.	-4.5					
191.7	2.					
167.	7.7					
140.	14.					
117.5	18.					
100.	22.					
84.	25.	0	1.	-16.5	1.	75.
87.5	38.					
88.	52.5					
87.	67.5					
84.	82.5					
77.5	97.					
68.	110.					
57.	122.					
44.	130.					
30.	137.					
15.	140.5					
0.	141.					
CORR. POINTS						
6.	5.					
12.	14.					
14.	16.					
19.	24.					

END OF SECTION 5.

0.

EARLY SST CONFIGURATION IN THE VICINITY OF THE WING APEX

SECTION NUMBER = 1

0 T1 = 1190.0

T2 = 1360.0

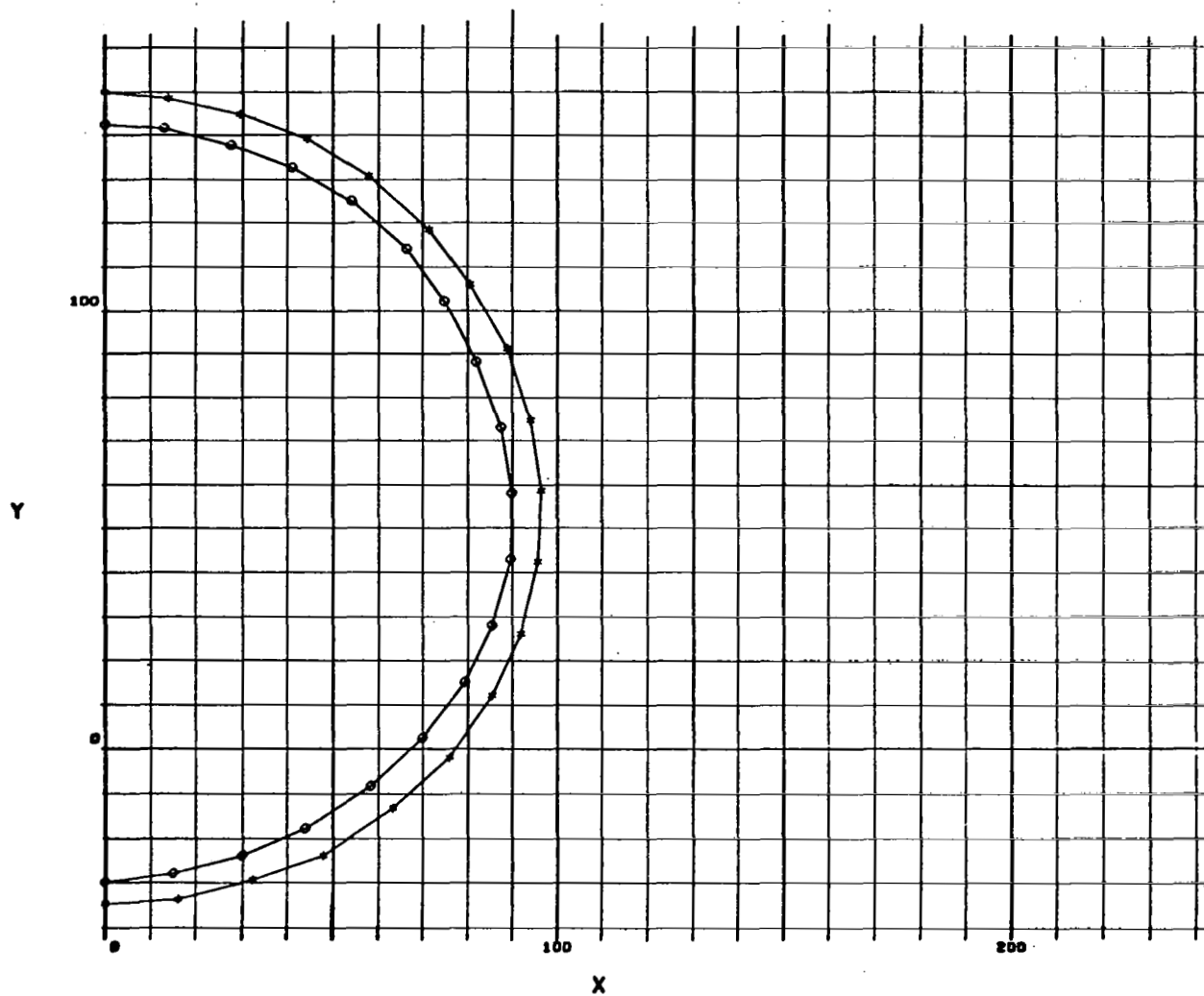


FIGURE 38.—SST GEOMETRY

EARLY SST CONFIGURATION IN THE VICINITY OF THE WING APEX

SECTION NUMBER = 2

O T1 = 1360.0

* T2 = 1462.0

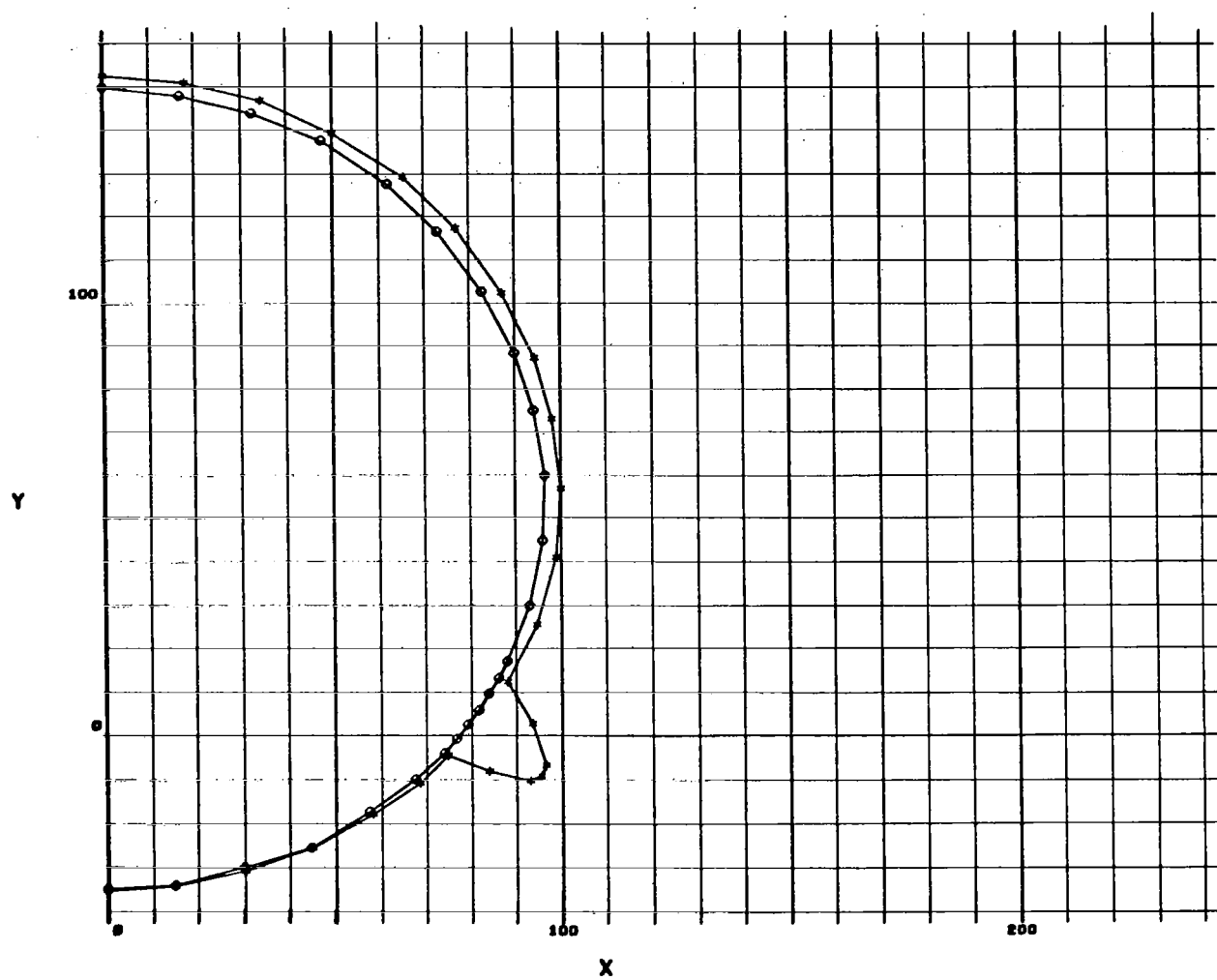


FIGURE 38.—Continued

EARLY SST CONFIGURATION IN THE VICINITY OF THE WING APEX

SECTION NUMBER = 3

○ T1 = 1462.0

● T2 = 1658.0

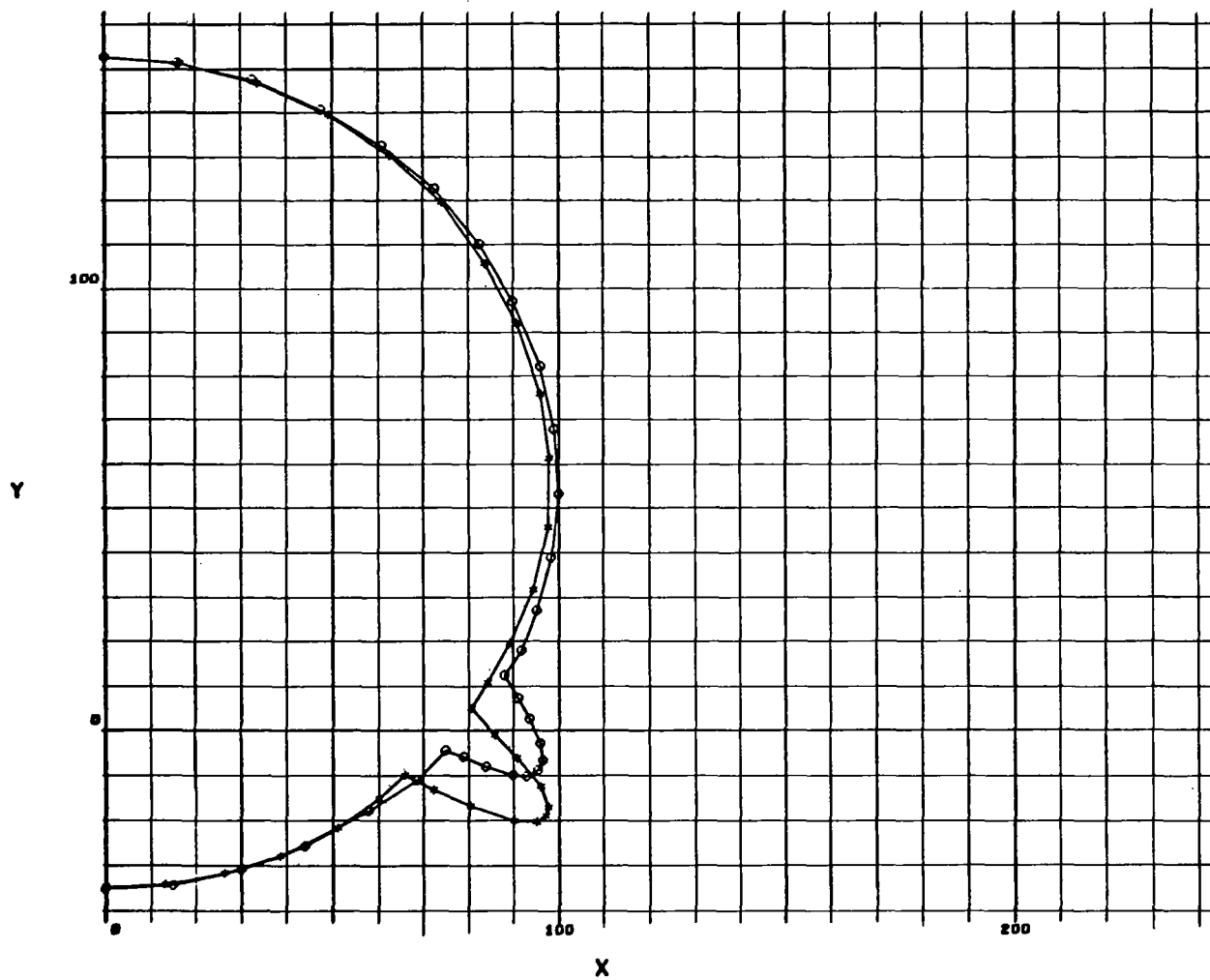


FIGURE 38.—Continued

EARLY SST CONFIGURATION IN THE VICINITY OF THE WING APEX

SECTION NUMBER = 4

0 T1 = 1658.0

* T2 = 1800.0

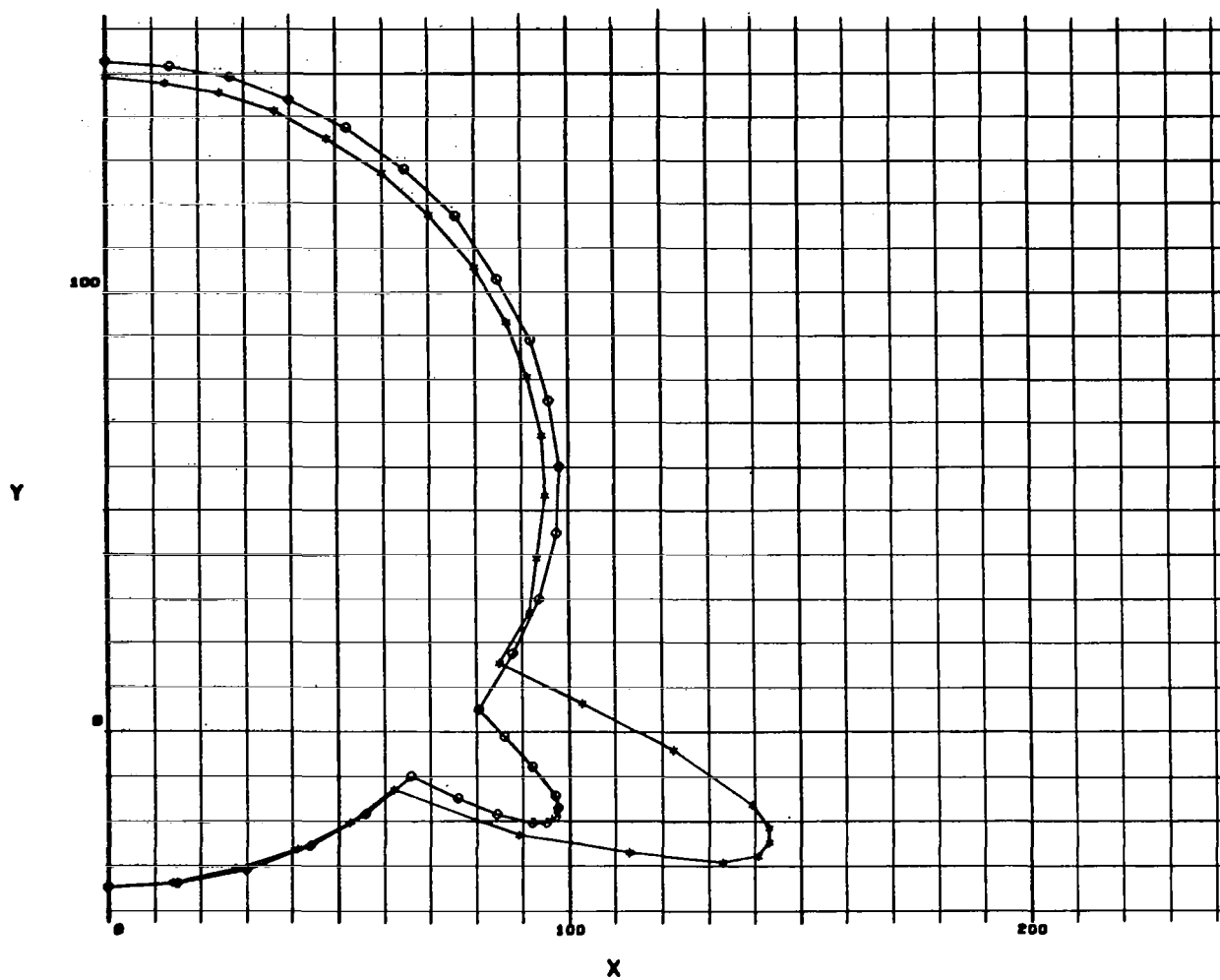


FIGURE 38.—Continued

EARLY SST CONFIGURATION IN THE VICINITY OF THE WING APEX

SECTION NUMBER = 5

0 T1 = 1800.0

* T2 = 2047.0

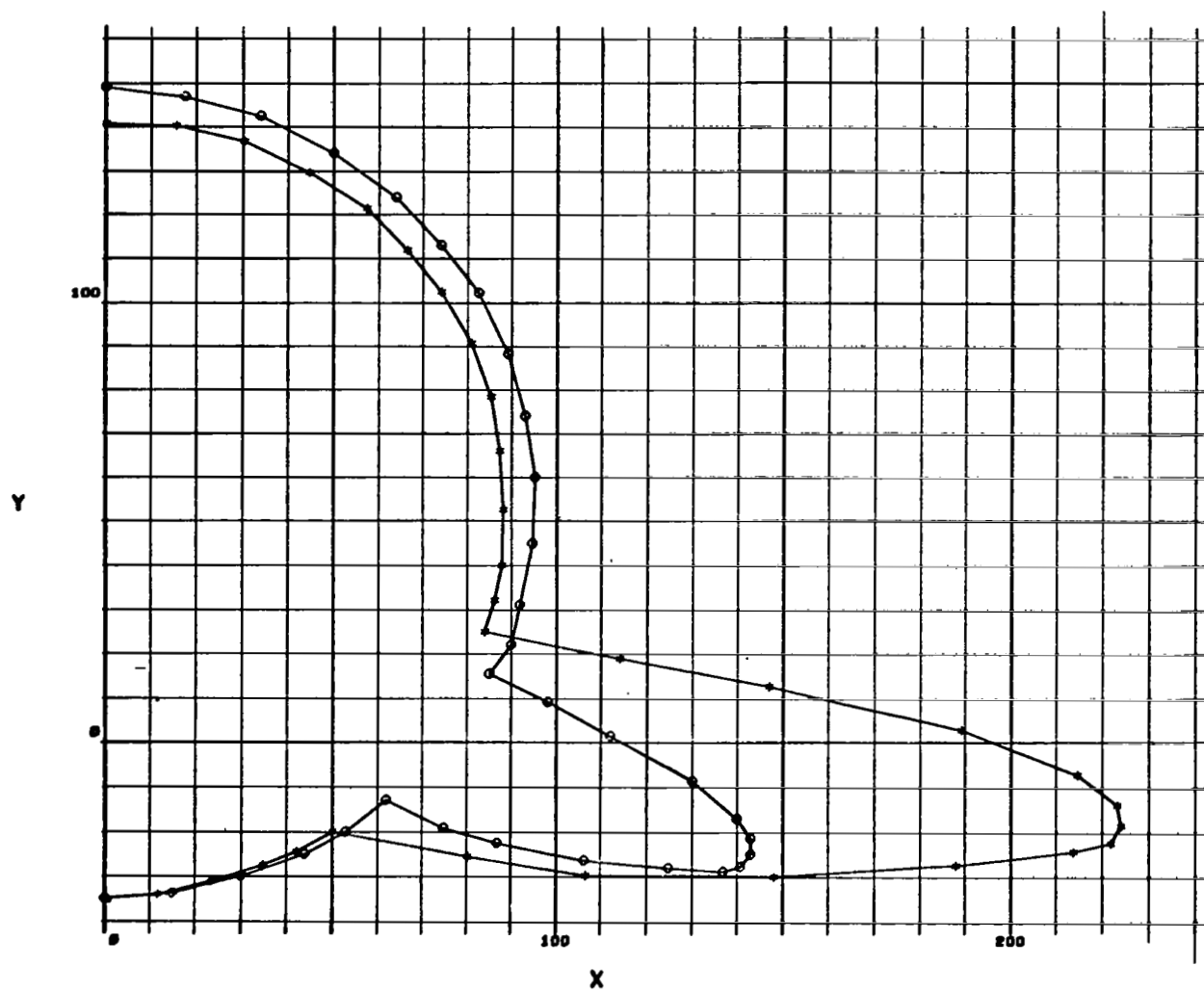


FIGURE 38.—Concluded

REFERENCES

1. Rakich, J. V.: Application of the Method of Characteristics of Noncircular Bodies at Angle of Attack. Symposium on Analytic Methods in Aircraft Aerodynamics, NASA-Ames, October 28-30, 1969.
2. Beeman, E. R., and Powers, S. A.: A Method of Determining the Complete Flow Field Around Conical Wings at Supersonic/Hypersonic Speeds. Preprint 69-646, AIAA, June 1969.
3. Lax, P. D.: Weak Solutions of Nonlinear Hyperbolic Equations and Their Numerical Computation. *Comm. Pure Appl. Math.*, 7, 1954.
4. Lax, P. D., and Wendroff, B.: Systems of Conservation Laws. *Comm. Pure Appl. Math.*, vol. XIII, 1960, p. 217.
5. DeJarnette, F. R.: Numerical Solution of Inviscid Hypersonic Flows for Nonequilibrium Vibration and Dissociation, Using an "Artificial Viscosity" Method. Ph.D., Thesis, V.P.I., 1965.
6. Thommen, H. W. and D'Attorre, L.: Calculation of Steady, Three-Dimensional Supersonic Flow Fields by a Finite Difference Method. Paper 65-26, AIAA, 1965.
7. Kutler, P.: Application of Selected Finite Difference Techniques to the Solution of Conical Flow Problems. Ph.D. Thesis, Iowa State University, 1969.
8. Van Dyke, M. D.: A Study of Hypersonic Small-Disturbance Theory. NACA Report 1194, 1954.
9. Hayes, W. D. and Probstein, R. F.: Hypersonic Flow Theory. Vol. I—Inviscid Flows. Second ed., 1966.
10. Chu, C. K., ed.: Computational Fluid Dynamics. Selected reprints, vol. IV, AIAA, 1968.
11. Lapidus, A.: A Detached Shock Calculation by Second-Order Finite Differences. *Journal of Computational Physics* 2, 1967, pp. 154-177.
12. Morretti, G.: The Importance of Boundary Conditions in the Numerical Treatment of Hyperbolic Equations. PIBAL Report 68-34, 1968.
13. Babenko, K. I., Voskrenenskiy, G. P., Lyubimov, A. N., and Rusanov, V. V.: Three-Dimensional Flow of Ideal Gas Past Smooth Bodies. NASA TT F-380, 1966.
14. Van Dyke, M.D.: First- and Second-Order Theory of Supersonic Flow Past Bodies of Revolution. *Journal of the Aeronautical Sciences*, March 1951.
15. Holt, M., and Blackie, J.: Experiments on Circular Cones at Yaw in Supersonic Flow. *Journal of the Aeronautical Sciences*, October 1956, p. 931.

16. Eggers, A. J., Savin, R. C., and Syvertson, C. A.: The Generalized Shock Expansion Method and Its Application to Bodies Traveling at High Supersonic Air Speeds. *Journal of the Aeronautical Sciences*, April 1955, p. 231.
17. Gregory, T. J., Wilcox, D. E., and Williams, L. J.: The Effects of Propulsion System-Airframe Interactions on the Performance of Hypersonic Aircraft. Paper 67-493, AIAA, 1967.
18. Chapkis, R. L.: Hypersonic Flow Over an Elliptic Cone: Theory and Experiment. Memo 49, Calif. Inst. Tech., Guggenheim Aeron. Lab., May 1959.
19. South, J. C., and Klunker, E. B.: Methods of Calculating Nonlinear Conical Flows. NASA Symposium on Analytical Methods in Aircraft Aerodynamics, October 28-30, 1969.
20. Rogers, E. W. E., and Berry, C. J.: Experiments at $M = 1.41$ on Elliptic Cones With Subsonic Leading Edges. R&M 3042, ARC, October 1955.
21. Kennet, H.: The Inviscid Hypersonic Flow on the Windward Side of a Delta Wing. Paper 63-55, IAS, 1963.
22. Babaev, D. A.: Numerical Solution of the Problem of Supersonic Flow Past the Lower Surface of a Delta Wing. *AIAA J.*, vol. 1, no. 9, September 1963, p. 2224.
23. Voskrenskii, G. P.: Chislennoe Reshenie Zadachi Obtekaniia Proizvol'noi Poverkhnosti Treugul'nogo Kryla v Oblasti Szhatiia Sverkhzvukovym Potokom Gaza (Numerical Solution of the Problem of a Supersonic Gas Flow Past an Arbitrary Surface of a Delta Wing in the Compression Region). *Izv. Akad. Nauk SSSR, Mekh. Zhidk. Gaza*, no. 4, 1968, pp. 134-142.
24. Randall, R. E., Bell, D. R., and Burk, J. L.: Pressure Distributions Tests of Several Sharp Leading Edge Wings, Bodies, and Body/Wing Combinations at Mach 5 and 8. AEDC TN-173, September 1960.
25. MacCormack, R. W.: Numerical Solution of the Interaction of a Shock Wave With a Laminar Boundary Layer. Second International Conference on Numerical Methods in Fluid Dynamics, University of California, Berkeley, California, September 15-19, 1970.

★ U. S. GOVERNMENT PRINTING OFFICE : 1972 720-403/325